Charles University
Faculty of Science

Study program: Modelling of Chemical Properties of Nano- and Biostructures

M.Sc. Pengbo Lyu

Theoretical Investigation of Novel Two-dimensional Materials with Application Potential

Teoretické studium aplikačního potenciálu nových dvourozměrných materiálů

Type of thesis

Doctoral thesis

Supervisor: prof. RNDr. Petr Nachtigall, Ph.D.

Prague, 2019

Declaration of Authorship

I declare that I have presented this work independently and I have properly cited all literature. Neither this work nor a substantial part of it has ever been submitted to obtain any other academic degree.

This work was based on following publications:

(1) Jing Jing Liu, **Pengbo Lyu**, Yu Zhang, Petr Nachtigall, Yuxi Xu, *New Layered Triazine Framework/Exfoliated 2D Polymer with Superior Sodium-Storage Properties*. *Adv. Mater.*, **2018**, 30, 1705401.

(2) Dana Schwarz, Amitava Acharja, Arun Ichangi, **Pengbo Lyu**, Maksym V. Opanasenko, Fabian R. Goßler, Tobias A. F. König, Jiří Čejka, Petr Nachtigall, Arne Thomas, Michael J. Bojdys, *Fluorescent sulphur and nitrogen containing porous polymers with tuneable donor-acceptor domains for light-driven hydrogen evolution*. *Chem. Eur. J.*, **2018**, 24, 11916.

(3) Dana Schwarz, Amitava Acharjya, Arun Ichangi, Yaroslav S. Kochergin, **Pengbo Lyu**, Maksym V. Opanasenko, Ján Tarábek, Jana Vacek Chocholoušová, Jaroslav Vacek, Johannes Schmidt, Jiří Čejka, Petr Nachtigall, Arne Thomas, Michael J. Bojdys, *Tuning the Porosity and Photocatalytic Performance of Triazine-Based Graphdiyne Polymers through Polymorphism*. *ChemSusChem*, **2019**, 12, 194.

(4) Haiyan Duan, **Pengbo Lyu**, Jingjing Liu, Yanli Zhao, and Yuxi Xu, *Semiconducting Crystalline Two-Dimensional Polyimide Nanosheets with Superior Sodium Storage Properties*, *ACS Nano*. **2019**, 13, 2, 2473-2480.

(5) Jingjing Liu, Yang Yang, **Pengbo Lyu**, Petr Nachtigall, Yuxi Xu, *Few-Layer Silicene Nanosheets with Superior Lithium-Storage Properties. Adv. Mater.*, **2018**, 30, 1800838.

(6) Shan Gong, Guangyu Zhao, **Pengbo Lyu**, Kening Sun, *A Pseudolayered MoS_2 as Li-Ion Intercalation Host with Enhanced Rate Capability and Durability*. *Small*, **2018**, 14, 1803344.

(7) Shan Gong, Guangyu Zhao, **Pengbo Lyu**, Kening Sun, *Insights into the intrinsic capacity of interlayer-expanded MoS_2 as a Li-ion intercalation host*. *J. Mater. Chem. A,* **2019**,7, 1187.

(8) **Pengbo Lyu**, Junjie He and Petr Nachtigall, *Theoretical investigation of CO catalytic oxidation by a Fe–PtSe2 monolayer*. *RSC Adv.*, **2017**, 7, 19630.

(9) Junjie He, **Pengbo Lyu**, Lizhong Sun, Angel MoralesGarcia, Petr Nachtigall, *Two-dimensional Janus MXenes: High-temperature Spin-polarized Semiconductor with Zero Magnetization*. *J. Mater. Chem. C*, **2016**, 4, 6500.

(10) Junjie He, **Pengbo Lyu**, Petr Nachtigall, *New TwoDimensional Mn-based MXenes with Room-Temperature Ferromagnetism and Half-Metallicity*. *J. Mater. Chem. C*, **2016**, 4, 11143.

(11) Junjie He, ShuangYing Ma, **Pengbo Lyu**, Petr Nachtigall, *Unusual Dirac Half-Metallicity with Intrinsic Ferromagnetism in Vanadium Trihalides Monolayers*. *J. Mater. Chem. C*, **2016**, 4, 2518.

(12) Junjie He, Xiao Li, **Pengbo Lyu**, Petr Nachtigall, *NearRoom-Temperature Chern Insulator and Dirac Spin-Gapless Semiconductor: Nickle Chloride Monolayer*. *Nanoscale*, **2016**, 4, 2518.

My contributions to these publications were as follows:

In the 1st paper, I investigated the stability of CTF-1 with different stacking considering solution effect using DFT calculations and participated in paper writing, my overall contribution in this paper is 40%.

In the 2nd and 3rd papers, I investigated various COFs for their structures and electronic structures using DFT calculations and the overall contributions are both 15%.

In the 4th paper, I investigated the polyimide COF for its structure and evaluated its performance as a sodium ion battery electrode using DFT calculations and the overall contribution is 30%.

In the 5th paper, I investigated the few-layer-thick silicene using DFT calculations for its structure and application as a lithium ion battery electrode, the overall contribution is 20%.

In the 6th and 7th papers, I did DFT calculations to investigate the interlayer-expanded MoS_2 for its structure and performance as lithium ion battery electrode, respectively. My overall contribution is 25%.

In the 8th paper, I did DFT calculations for the theoretical investigation to seek and evaluate CO oxidation catalysts. My overall contribution is 90%.

In the 9th –12th papers, I evaluated the magnetic properties and Curie/Néel temperatures using Monte-Carlo simulations based on DFT calculations for various 2D materials and my overall contribution is 15%.

Signed:

_____

Date:

_____

Acknowledgements

Foremost, I would like to express my sincere gratitude to my supervisor, Prof. Petr Nachtigall. I really appreciate his keen interest and dedication to help his students during my whole PhD study. The completion of this thesis is impossible without his patient guidance in scientific research. Then I would like to thank my advisor, Lukáš Grajciar. He is always eager to help me with kind suggestions. I also want to thank all my current and former colleagues in our group for all their help which were always timely: Junjie He, Miroslav Položij, Ángel Morales-García, Viet Thang Ho, Christopher James Heard, Federico Brivio, Shuo Li, Dianwei Hou, Mengtin Jin, Chen Lei, Mingxiu Liu and Song Lu. I want to thank Carlos Henrique Vieira Melo, who have helped me a lot with scientific writing. I would like to express my deep appreciations to other people in our department, with whom I have discussed and from whom I have learned.

I would like to thank our experimental collaborators that this thesis is also impossible without their excellent efforts: Michael J. Bojdys from Charles University (then) and Humboldt-Universität zu Berlin (now); Michael Ertl and Josef Breu from University of Bayreuth; Jingjing Liu, Haiyan Duan, Yuxi Xu from Fudan University, China; Shan Gong and Kening Sun from Harbin Institute of Technology, China.

Finally I want to thank my parents and other family members for all their understanding, support and encouragement. Thank you very much.

Pengbo Lyu

March 2019

Abstract

Electron confinement due to the two-dimensional (2D) nature of layered materials accounts for their fascinating electronic properties and for their applications in new-generation electronic devices. Moreover, the large specific surface area of 2D materials also enables their use in surface-related applications, such as catalysis and adsorption. In addition, these 2D materials are promising photocatalysts thanks to the shorter migration distance of photogenerated electrons and of electron holes. The research reported in this thesis aimed to provide atomistic insight into 2D layered materials, particularly into their structures, electronic properties and potential applications in the field of catalysis, photocatalysis and alkali metal ion batteries. Our findings are not only theoretically relevant but also open new research avenues for our experimental collaborators to improve specific properties and activities of their materials. The main results from this thesis, for five different classes of 2D materials, are summarized below.

2D covalent organic frameworks (COFs). CTF-type COFs with similar topology but different nitrogen-to-carbon ratios were investigated for their potential in photocatalytic water splitting. More specifically, torsion and bending effects on structure stability were investigated in detail. In addition, structural effects on band gap and band edge positions were discussed herein considering the conditions required for photocatalytic water splitting. Our results showed that these COFs are potential photocatalysts for water splitting, whose performance can be tuned by adjusting the nitrogen-to-carbon ratio and by layer arrangements, depending on the synthesis strategy. Importantly, both factors can be experimentally tuned; therefore, our results help to guide the preparation of CTF-type COFs with optimal photocatalytic performance. Accordingly, in collaboration with experimental groups, we explored several applications of COFs. For sulphur- and nitrogen-containing COFs, we calculated their structures and band structures, which were in good agreement with the corresponding experimental data. For triazine-based graphdiyne polymers, we calculated their structures and compared simulated and experimental SAED patterns. For polyimide COF, we obtained structures in good agreement with experimental data and calculated its specific capacity as a sodium-ion battery electrode, which were also in satisfactory agreement with experiments.

Silicene. High-quality silicene, which was synthesized by our experimental collaborators via $CaSi_2$ oxidation and exfoliation in the liquid phase, forms a monolayer or few-layer-thick

sheets with high crystallinity. Silicene has been experimentally explored as a new anode for lithium ion batteries (LIBs) with impressive cycling stability. To evaluate its performance as an LIB electrode, from an atomistic point of view, silicene was modelled as both monolayer and bilayer. Considering different adsorption sites, the formation energy profile was assessed based on the most stable configurations. Subsequently, the specific capacity for each model was calculated with respect to their fully lithiated structures. The results from the bilayer model were in excellent agreement with the experimental data on the specific capacity of the silicene anode.

Transition metal dichalcogenides (TMDs). An interlayer-expanded MoS_2 material previously prepared by oxygen incorporation has been shown to have superior performance as an LIB electrode material by our experimental collaborators. Thus, first-principle calculations were performed to gain atomistic insight into its interlayer structures and performance as an LIB electrode. Our results show that the interlayer-expanded MoS_2 has higher specific capacity than pristine MoS_2, in qualitative agreement with experimental findings. A quantitative agreement with the experimental data was also assessed when considering the presence of molybdenum oxide species (resulting from oxygen incorporation) in the interlayer space. $PtSe_2$ monolayers, another type of TMDs, embedded with 3*d* transition metal atoms in Se vacancies, were investigated for their potential as CO oxidation catalysts under mild conditions. The results showed that the Fe-$PtSe_2$ system was the best candidate, and reaction mechanisms for this catalyst were investigated in detail. Our kinetic analysis showed that both Langmuir-Hinshelwood and Eley-Rideal mechanisms have comparable reaction rate constants under mild conditions.

Transition metal carbides (MXenes) and transition metal trihalides (TMTs). Two-dimensional materials often show interesting magnetic properties. For practical applications in spintronics, these two-dimensional materials must maintain their magnetic properties near room temperature. However, only a limited number of 2D materials intrinsically meet such requirement. Therefore, we investigated suitable candidates for spintronics, in particular 2D Cr- and Mn-based MXenes as well as V- and Ni-based TMTs. These two-dimensional materials showed various intrinsic magnetic properties, such as antiferromagnetism with spin-polarized semiconductivity (Cr-based MXene), ferromagnetism with half-metallicity (Mn-based MXene), ferromagnetism with Dirac half-metallicity (VI_3 and VCl_3) and ferromagnetism with Dirac spin-gapless semiconductivity ($NiCl_3$). In addition, Monte-Carlo simulations indicated high Curie/Néel temperatures for these materials, thus suggesting their high potential for practical applications in spintronics.

Layered double hydroxides (LDHs). LDHs have already been extensively studied for various applications. Hence, understanding their structures will enable us to advance research on these materials. However, the structure of mössbauerite, belonging to the special fougèrite group (having the same divalent and trivalent ions – Fe), remains poorly understood. Thus, mössbauerite was computationally investigated, in addition to fougèrite. Both theoretical and experimental results showed that the mössbauerite structure consists of both carbonate-grafted and non-grafted layers, whereas no carbonate grafting was found for fougèrite. The mechanism of grafting and fougèrite oxidation to mössbauerite was also computationally explored, showing that the driving force of the formation of carbonate-grafted structures in mössbauerite is a strongly exothermic reaction between fougèrite and hydrogen peroxide.

Keywords: Two-dimensional Material; Covalent Organic Framework; Silicene; Transition metal Dichalcogenide; MXene; Transition Metal Trihalide; Layered Double Hydroxide; Density Functional Theory; Modeling; Monte Carlos Simulations; Photocatalysis; Catalysis; Reaction Mechanisms; Alkali-ion Battery

Abstrakt v českém jazyce

Elektronová struktura tenkých dvourozměrných (2D) materiálů je velmi odlišná od elektronové struktury korespondujících trojrozměrných materiálů. V důsledku prostorového omezení vykazuje elektronová struktura 2D materiálů neobyčejné vlastnosti, které jsou vhodné k řadě aplikací v elektronice. Velký povrch 2D materiálů je rovněž vhodný pro aplikace v katalýze a adsorpci. Další potenciální uplatnění 2D materiálů je možné očekávat ve fotokatalýze, pro kterou je výhodná krátká vzdálenost k povrchu pro fotokatalyticky generované elektrony a elektronové díry. Výsledky prezentované v této dizertační práci jsou motivovány snahou pochopit vlastnosti 2D na atomární úrovni a lépe porozumět jejich struktuře, elektronové struktuře a potenciálním aplikacím v oblasti katalýzy, fotokatalýzy a alkalických baterií. Věříme, že výsledky zde prezentované jsou relevantní nejen z hlediska teoretického studia 2D materiálů, ale pomohou i experimentálním kolegům na cestě k novým 2D materiálům hledaným pro konkrétní aplikace. Hlavní výsledky této práce jsou stručně popsány níže pro pět tříd 2D materiálů.

2D kovalentní organické sítě. Tyto materiály se označují zkratkou COF z anglického "covalent organic framework". Jedním z typů materiálů COF jsou tzv. CTF sítě, které mají podobnou topologii, ale různý poměr mezi dusíkem a uhlíkem. Tyto materiály byly studovány vzhledem k jejich potenciálu pro fotokatalytické štěpení vody. V první řadě byla studována struktura těchto materiálů, zejména efekty plynoucí z rozdílného C/N poměru. Následně byl studován vliv struktury na pásovou strukturu materiálů a jejich fotokatalytické vlastnosti. Výsledky ukazují, že CFT materiály jsou vhodné fotokatalyzátory pro rozklad vody. Jejich fotokatalytické vlastnosti závisí na N/C poměru a uspořádání jednotlivých vrstev. Oba tyto faktory mohou být experimentálně kontrolovány. Dosažené výsledky tak ukazují cestu k optimálním fotokatalyzátorům v dané třídě materiálů. Byly studovány rovněž další typy COF obsahující dusík a síru a to zejména z hlediska jejich struktury a elektronických vlastností. Byly počítány SAED difrakce a srovnávány s dostupnými experimentálními údaji. Pro některé ze studovaných COF byly počítány jejich vlastnosti relevantní pro využití v alkalických bateriích.

2D křemíkové vrstvy. Nové experimentální postupy založené na oxidaci $CaSi_2$ vedly k přípravě vysoce kvalitních 2D křemíkových vrstev (silicene). Motivováni tímto novým experimentem jsme společně s experimentálními kolegy studovali strukturu 2D křemíkových vrstev a jejich potenciál jako anodový materiál pro lithiové baterie. Specifické kapacity byly počítány pro různé modely a výsledky byly diskutovány na základě porovnání s experimentálními daty.

Chalkogenidy tranzitních kovů. Struktura a uspořádání 3D a exfoliovaných 2D vrstev MoS_2 byla modelována ve spolupráci s experimentálními kolegy vzhledem k jejich potenciálu jako anody pro lithiové baterie. Podstatně vyšší specifické kapacity byly nalezeny pro MoS_2, ve kterém byly sousední vrstvy expandovány přítomností oxidů a hydroxidů molybdenu. 2D $PtSe_2$ byl studován z hlediska oxidace CO za mírných podmínek. Nahrazení jednoho atomu Se atomem tranzitního kovu vede k materiálu, který má vhodné katalytické vlastnosti pro studovaný proces. Na základě systematického studia vlastností takto vytvořených katalyzátorů s různými 3d tranzitními kovy byl identifikován katalyzátor $Fe@PtSe_2$ jako nejvhodnější pro oxidaci CO. Pro tento systém byl podrobně studován mechanismus oxidace a bylo zjištěna, že za mírných podmínek se mohou uplatnit oba typy mechanismů, tedy mechanismus Langmuirův-Hinshelwoodův i mechanismus Eleyův-Ridealův.

2D carbidy transitních kovů (MXene) a 2D halidy tranzitních kovů (TMT). Dvourozměrné halidy a karbidy tranzitních kovů vykazují magnetické vlastnosti, které je předurčují k aplikacím v elektronice a spintronice. Experimentální příprava těchto materiálů vede většinou k 2D matriálům, ve kterých je povrch funkcionalizován elektronegativním atomem nebo funkční skupinou. Z toho důvodu jsme studovali strukturu, stabilitu a magnetické vlastnosti 2D carbidů a halidů a to včetně zahrnutí vlivu povrchových funkčních skupin. Z výsledků studia vyplývá, že (i) nesymetricky funkcionalizované 2D carbidu chromu jsou spinově polarizované polovodiče, (ii) 2D carbidy managanu jsou feromagnetické polokovy, (iii) 2D VI_3 a VCl_3 jsou feromagnetické a vykazují Diracovu polokovovost a (iv) 2D $NiCl_3$ je feromagnetický a vykazuje Diracovu polovidivost. Monte Carlo simulace ukázali, že všechny tyto 2D materiály mají vysokou teplotu magnetického přechodu.

Podvojné vrstevnaté hydroxidy (LDH). Byla studována struktura a vlastnosti speciální třídy podvojných vrstevnatých hydroxidů, ve které je přítomno železo ve formě dvoj- i trojnásobně nabitého kationtu (fougèrite a mössbauerite). Zejména struktura mezi sousedními vrstvami (obsahující vodu a CO_3^{2-} anionty), jakož i mechanismus oxidace fougèrite na mössbauerite byla studována na DFT úrovni. Výsledky ukazují, že CO_3^{2-} zůstává v prostoru mezi vrstvami a nereaguje s povrchovými atomu ve fougèrite. V mössbauerite dochází naopak k reakci s povrchovými atomy. Tento proces nemůže nastávat samovolně, ale je způsoben reakcí s peroxidem vodíku, který se používá k oxidaci fougèrite na mössbauerite.

Klíčová slova: dvourozměrné materiály, kovalentní organické sítě, 2D vrstevnatý křemík, dichalkogenidy tranzitních kovů, MXene, trihalidy tranzitních kovů, podvojné vrstevnaté hydroxidy, teorie funkcionálu hustoty, modelování, Monte Carlo simulace, fotokatalýza, katalýza, reakční mechanismy, alkalické baterie

List of the Abbreviations

AIMD	*ab initio* Molecular Dynamics
CBM	Conduction Band Minimum
CI-NEB	Climbing Image Nudged Elastic Band
COF	Covalent Organic Framework
CTF	Covalent Triazine Framework
DFT	Density Functional Theory
DFT+U	Density Function Theory Plus Hubbard U
DOS	Density of States
ER	Eley-Rideal
GGA	Generalized Gradient Approximation
GW	Green's function and screened coulomb interaction
HSE	Heyd-Scuseria-Ernzerhof
LDA	Local Density Approximation
LDH	Layered Double Hydroxide
LDOS	Localized Density of States
LH	Langmuir-Hinshelwood
LIB	Lithium Ion Battery
MXene	Two-dimensional Transition Metal Carbide/Nitride/Carbonitride
OCV	Open Circuit Voltage
PBE	Perdew-Burke-Ernzerhof
PAW	Projector Augmented Wave
PXRD	Powder X-ray Diffraction
QAHE	Quantum Anomalous Hall Effect
QSHE	Quantum Spin Hall Effect
SAED	Selected Area Electron Diffraction
TEM	Transmission Electron Microscope
TM	Transition Metal
TMD	Transition Metal Dichalcogenide
TMT	Transition Metal Trihalide
UC	Unit Cell
VBM	Valence Band Maximum
XRD	X-ray Diffraction

Table of Contents

CHAPTER 1. Introduction

Two-dimensional (2D) layered materials have unusual optical and electronic properties resulting from the absence of a third dimension.[1-3] Compared with their conventional bulk counterparts, 2D layered materials have many advantages for practical applications, such as intrinsic uniform thickness, high specific surface area, and shorter migration distance of photogenerated electrons and holes, to name a few.[4, 5] However, the existence of 2D layered materials was still debated in the early 20th century because 2D materials were not considered thermodynamically stable at finite temperature due to thermal lattice fluctuations.[6] The breakthrough in research on 2D layered materials occurred in 2004, when the monolayer analog of graphite - graphene - was physically exfoliated and found stable under ambient conditions;[7] since then, graphene has been intensively studied for various applications.[8, 9]

Graphene is a sp^2-hybridized carbon sheet with a honeycomb lattice and with a very special electronic structure, which shows zero density of states at the Fermi level and no band gap. Thus, graphene is a semimetal, which limits its applications in some areas, such as optoelectronics and photocatalysis, where the semiconducting properties are required.[10, 11] In the last decade, numerous studies on graphene have paved the way towards other 2D materials.

Inspired by the rapid advances in graphene research, many new 2D layered materials with a rich spectrum of properties have been explored, thus promoting the new research field of 2D crystals. In this context, a number of 2D materials, including transition metal dichalcogenides (TMDs), layered double hydroxides (LDHs), silicene, transition metal carbides (MXenes), layered transition metal trihalides (TMTs) and covalent organic frameworks (COFs) have been theoretically investigated in this thesis, often hand-in-hand with experimental studies performed in collaboration with research groups worldwide.

The main goal of the thesis was to increase our understanding of the application potential of 2D materials. For such purpose, the systematic computational investigation presented herein helps to increase the atomistic understanding of these materials, particularly regarding key structure-property relationships. The systems computationally investigated in these studies are described below in Figure 1, showing typical structures of these materials.

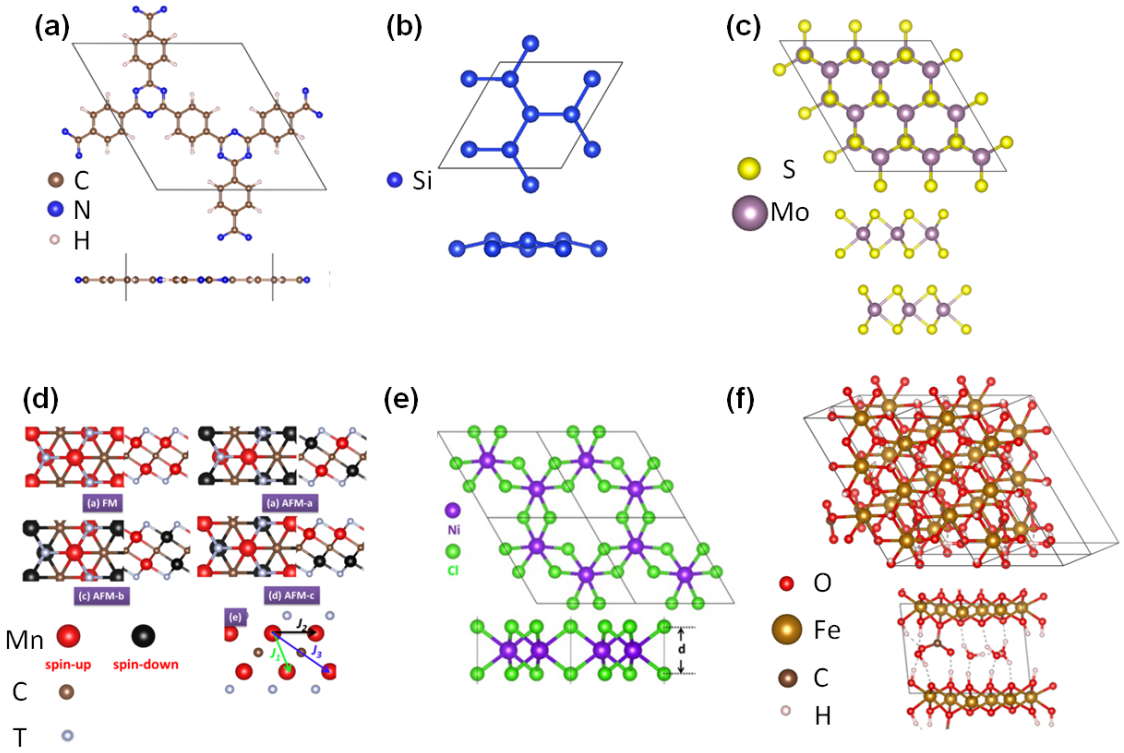

Figure 1: Top and side views of typical structures of (a) COF (CTF-1); (b) silicene; (c) TMD (2H-MoS_2); (d) MXene (Mn_2CT_2,T=F, Cl and OH); (e) TMT ($NiCl_3$) and (f) LDH (mössbauerite with grafted carbonate).

Two-dimensional organic layered materials, such as covalent organic frameworks (COFs), have many advantages over inorganic layered materials, including lower cost, easier preparation, higher mechanical flexibility[12] and concentration of reactive sites [13] and smaller environmental impact.[14] Layered COFs are crystals in which 2D polymers are held together via van der Waals (vdW) interactions. The low density of COFs and their layer arrangement, which is govern by vdW interactions, results in structures with 1D channels through 2D layers.[15-17] COFs can be prepared with tailored topology and pore sizes.[18-21] The flexibility of COF structures enables us to search for COFs for specific applications, such as alkali metal ion batteries and photocatalytic water splitting.[22] Although structures, interlayer arrangements and band gaps of numerous boron-based COFs have already been computationally investigated,[23, 24] no such systematic theoretical study has been performed for CTF-type COFs to determine the key factors of band gaps. In addition to photocatalytic applications, the 2D nature and incorporation of heteroatoms into the frameworks account for the efficient diffusion and storage properties of alkali atoms, which are essential for alkali-ion batteries.

Silicene, a silicon analog of graphene, has a non-planar honeycomb structure due to buckling resulting from a partial sp^3 hybridization of silicon atoms.[25] Moreover, exciting properties have been predicted for silicene, including a Dirac fermion state close to the Fermi Level;[26] stronger spin-orbit coupling and quantum spin Hall (QSHE) effects than those assessed in graphene;[27] and quantum anomalous Hall effect (QAHE).[28] Although 2D silicene materials are difficult to obtain, epitaxy on hosting substrates, such as Ag(1 1 1),[29] ZrB_2(0 0 0 1),[30] and Ir(1 1 1),[31] among others, or $CaSi_2$ exfoliation have enabled their preparation.[32] In contrast to the highly oxygen-active surface of silicon, resistance to oxygen was reported for silicene nanoribbons.[33] Furthermre, owing to its excellent properties, silicene is widely studied for various applications. For example, silicene is expected to improve the performance of solar cells[33] and LIBs[34] in terms of energy storage

Transition metal dichalcogenides with different properties from graphene are among the most intensively studied semiconducting layered materials. TMDs have the formula MX_2 (M=transition metal elements and X=chalcogen, *i.e.* S, Se and Te). Accordingly, they are layered materials with the X-M-X form in which two chalcogen layers are separated by a metal layer. In addition, octahedral or trigonal prismatic coordination of metal atoms in these materials results in the formation of hexagonal or rhombohedral crystals, and their strong intralayer bonding and weak interlayer interactions enable exfoliation into 2D layers.[35] Although TMDs have been studied for decades,[36] their 2D forms have only been recently investigated thanks to advances in material engineering that have made it possible to prepare, measure and manipulate atomically thin films. [35] Moreover, TMDs usually have direct band gaps above 1 eV. Therefore they have a high potential for applications in photocatalysis, optoelectronic devices and field effect transistors (FETs), among others.[4, 37-40], and their unique physical properties enable their application in novel valleytronics devices.[41] In addition to these applications as semiconductors, TMD-based materials have also been reported as promising materials for catalysis.[42-44]

MXenes and TMTs possess intrinsic magnetism suitable for practical applications in spintronics. MXenes ($M_{n+1}X_n$, M=transition metal, X=C or N, respectively), in which the transition metal layers are separated by carbon or nitrogen layers, are prepared by exfoliation of the MAX phase (A is an A-group element) via hydrofluoric acid (HF) etching.[45] The surfaces of MXenes are stabilized by saturation with functional groups such as OH, H, F and Cl. Although the intrinsic magnetism has been predicted for some MXenes,[46, 47] it generally disappears once the surfaces of MXenes are functionalized (due to completely compensated antiferromagnetic ground states). Thus, investigations of MXenes with asymmetric surface

functionalizations are theoretically and practically important for maintaining their intrinsic magnetism after functionalization. TMTs have the formula TMX_3, where X is a halide element in which transition metal atoms are octahedrally coordinated with halide atoms forming a honeycomb arrangement. The magnetism of 2D TMTs, such as CrI_3, has been experimentally confirmed.[48] The practical applications of 2D materials in spintronics rely on their intrinsic magnetism at high temperatures. Although magnetic properties can be introduced in various 2D layered materials using approaches such as doping, defects and/or functionalization, the experimental preparation of such materials with an highly ordered spin structure, as well as spin-polarization at room temperature, remains a challenge.[49] [50] Thus, MXenes and TMTs with intrinsic magnetism at high temperatures are desirable for applications in spintronics.

Layered double hydroxides (LDHs) are ionic layered materials holding together positively charged brucite-like layers $[(M^{2+}_{(1-x)}M^{3+}_{x})(OH)_2]^{x+}$ with water molecules and charge-compensating anions A^{n-} in the interlayer space. They have the general formula $[(M^{2+}_{(1-x)}M^{3+}_{x})(OH)_2]^{x+}[A^{n-}]_{x/n}\bullet mH_2O$ where m is the number of water molecules in the interlayer space.[51] A remarkable feature of LDHs is the absence of crosslinking between adjacent cationic layers, which allows the expansion and compression of the interlayer space to accommodate various exchangeable A^{n-}. Although LDHs are unstable under acidic conditions, they can be found in minerals[52] and synthetic LDHs are prepared using reconstruction [53] or co-precipitation [54] methods. They have already been widely studied for applications as CO_2 adsorbents,[55] ion exchange hosts,[56] flame retardants,[57, 58] elastomer composites,[59] LDH/carbon composites[60, 61] and pharmaceuticals[62] and in photochemistry[63, 64] and electrochemistry.[65, 66] Among all LDHs, fougèrite group minerals are a unique subgroup of hydrotalcites in which divalent and trivalent cations are the same element (Fe) [67], and they naturally occur in green rust phases. There are three distinct fixed-composition phases of fougèrite group LDHs, including fougèrite ($Fe^{II}_4Fe^{III}_2(OH)_{12}[CO_3]\cdot 3H_2O$), trébeurdenite ($Fe^{II}_2Fe^{III}_4O_2(OH)_{10}[CO_3]\cdot 3H_2O$) and mössbauerite ($Fe^{III}_6O_4(OH)_8[CO_3]\cdot 3H_2O$). Despite some efforts,[67] the interlayer structure of mössbauerite has not yet been fully described. The interlayer structure, including an interlayer distance which is smaller than that of fougèrite, remains unclear, and even though an in-depth and thorough analysis of fougèrite group structures is essential to advance research on these LDHs, no theoretical investigation has been performed to improve our atomistic understanding of these materials.

Based on the above, this thesis is organized into the following sections: after this introduction (Section 1), the individual computational methods used throughout this investigation are briefly described in Section 2, together with technical details of the calculations. The results and their discussion are presented in Section 3, starting with findings relevant for organic 2D materials, followed by results from investigations of various inorganic 2D materials. Conclusions are drawn in Section 4. The order in which individual materials are analyzed in this thesis is motivated by the relevance of their potential applications.

Section 3 is divided into five sub-sections. Initially, COFs are reported in Section 3.1. The systematic study of the stacking stability of CTF-type COFs and its effect on photocatalytic water splitting performance is reported first, followed by results from our collaborations with experimental groups. Then, we report the investigation of several different COFs for their structure, electronic structure and applications, for example, as sodium-ion battery electrodes. Our experimental collaborators include Xu's Group from Fudan University, China, and Bojdys's group from Charles University then, now from Humboldt-Universität zu Berlin, Germany. Subsequently, the investigation of silicene is reported in Section 3.2; in collaboration with Xu's group from Fudan University, China, we investigated its structure and application as lithium ion battery electrode. Then, the investigation of TMDs is reported in Section 3.3. In collaboration with Sun's group from the Harbin Institute of Technology, China, we determined the structure and assessed is potential as a lithium-ion battery electrode for oxygen-expanded MoS_2. In addition, the theoretical investigation of $PtSe_2$ monolayers with embedded transition metal atoms (Sc–Zn) in Se vacancies as CO oxidation catalyst is also reported in this sub-section. The following sub-section (3.4) includes the results from the theoretical investigation of Cr- and Mn-based MXenes and TMTs (VCl_3, VI_3 and $NiCl_3$) and their intrinsic magnetic properties associated with high Curie/Néel temperatures. Lastly, the investigation of LDHs is reported in Section 3.5. In collaboration with Breu's group from University of Bayreuth, Germany, we report the theoretical results from a systematic investigation of the structure of fougèrite group LDHs, in particular, fougèrite and mössbauerite.

The main goal of the thesis is to provide an atomistic understanding of structures and properties of 2D materials. The motivation for this research is two-fold: (i) theoretical investigation of existing materials in close collaboration with experimental groups to provide an atomistic interpretation of available experimental data and to increase our understanding of structure/property relationships; (ii) *in silico* investigation of experimentally unknown

materials to screen for potential applications of such materials and, thus, to help our experimental colleagues synthesize challenging 2D materials. For the latter purpose, we investigated materials designed by an introduction of relatively small modifications in existing materials. All calculations reported in the thesis were obtained at the density functional theory level, employing either GGA or hybrid type exchange-correlation functionals to maintain a relatively high reliability of calculated properties, as shown by a good (in some cases excellent) agreement with available experimental data. Our calculations also provide useful suggestions for experimentalists to design and to develop advanced materials with improved performance for practical applications. Novel 2D materials are highly desired in many fields for their superior properties. However, advanced 2D materials for specific purposes are generally obtained on a trial-and-error basis. Herein, we have developed a theoretical approache to predict and design 2D materials with tailored properties, which should greatly facilitate experimental studies. Ultimately, we aim to promote the research of 2D materials with a high potential for applications in several areas. We believe that the results reported herein are highly relevant from the theoretical and practical standpoints.

CHAPTER 2. Methods

Various two-dimensional materials, including COFs, silicene, TMDs, MXenes, TMTs and LDHs were investigated computationally using periodic first-principle calculations. All electronic-structure calculations were performed at the DFT level. The majority of calculations were done for the structure optimization, transition state search and for various properties resulting from the electronic structure of the materials (band gaps, magnetic properties, etc.) In addition to the theoretical investigations, we were also devoted to gain atomistic insight into the real materials in collaboration with experimental groups. This section briefly describes the methods used in this thesis.

2.1 DFT methods

Most quantum chemical approaches are targeting the approximate solution of the time-independent, non-relativistic Schrödinger equation:[68]

$$\widehat{H}\Psi(\mathbf{x_1}, \cdots \mathbf{x_N}, \mathbf{R_1}, \cdots \mathbf{R_M}) = \mathrm{E}\Psi(\mathbf{x_1}, \cdots \mathbf{x_N}, \mathbf{R_1}, \cdots \mathbf{R_M}) \tag{2.1}$$

where $\widehat{H}$ is the Hamiltonian for a molecular system containing M nuclei and N electrons without external magnetic or electric fields and Ψ is a wave function for such system. $\widehat{H}$ could be expressed as (in atomic units): [68]

$$\widehat{H} = -\frac{1}{2}\sum_{i=1}^{N}\nabla_i^2 - \frac{1}{2}\sum_{A=1}^{M}\frac{1}{M_A}\nabla_A^2 - \sum_{i=1}^{N}\sum_{A=1}^{M}\frac{Z_A}{r_{iA}} + \sum_{i=1}^{N}\sum_{j>i}^{N}\frac{1}{r_{ij}} + \sum_{A=1}^{M}\sum_{B>A}^{M}\frac{Z_A Z_B}{R_{AB}} \tag{2.2}$$

where A and B run over M nuclei, while i and j run over N electrons in the system. The first two terms represent the kinetic energy of electrons and nuclei, respectively. The third term represents the attractive electrostatic interaction between nuclei and electrons. The fourth and fifth terms represent the electron-electron and nucleus-nucleus repulsion, respectively.

Since electrons are moving much faster than nuclei, the motion of electrons can be considered in the field of fixed nuclei, which is called Born-Oppenheimer approximation, and thus the complete Hamiltonian (2.2) is reduced to electronic Hamiltonian: [68]

$$\widehat{H}_{\mathrm{elec}} = -\frac{1}{2}\sum_{i=1}^{N}\nabla_i^2 - \sum_{i=1}^{N}\sum_{A=1}^{M}\frac{Z_A}{r_{iA}} + \sum_{i=1}^{N}\sum_{j>i}^{N}\frac{1}{r_{ij}} \tag{2.3}$$

The solution of the $\widehat{H}_{\mathrm{elec}}$ is the electronic wave function Ψ_{elec} and the electronic energy E_{elec}:

$$\widehat{H}_{\mathrm{elec}}\Psi_{\mathrm{elec}} = E_{\mathrm{elec}}\Psi_{\mathrm{elec}} \tag{2.4}$$

The total energy E_{tot} is the sum of E_{elec} and the constant nuclear repulsion term $\sum_{A=1}^{M}\sum_{B>A}^{M}\frac{Z_A Z_B}{R_{AB}}$.

However, the traditional wave function theory (WFT) based approaches for solving Schrödinger equation depends on the wave functions with 4*N* coordinates (3 spatial and 1spin coordinates for each electron). Thus, it is extremely expensive for large systems. In contrast, the target of density function theory (DFT) is to find the total electron spin-densities which depend only on 8 coordinates. It is therefore conviniet to model large systems such as those investigated in this thesis. In addition, within DFT scheme it is conceptually easier to take electron correlation into account, although practically many approximations are needed.

In modern density functional formalism, the of exact density functional formalism given by Hohenberg and Kohn (HK) [69] is based on the variational principle. The relationship between electron density $n(\mathrm{r})$ and ground state wave function Ψ is: [68]

$$\rho(\mathbf{r}) = \int ds_1 d\mathbf{x}_2 \cdots d\mathbf{x}_N \Psi^*(\mathbf{x_1}, \mathbf{x_2}, \cdots, \mathbf{x_N})\Psi(\mathbf{x_1}, \mathbf{x_2}, \cdots, \mathbf{x_N}) \tag{2.5}$$

The first HK theorem demonstrates that the external potential V_{ext} (within a constant) and hence the total energy is uniquely determined by electron density $n(\mathrm{r})$ of an *N*-electron system. Excited states are also determined by $\rho(\mathbf{r})$ because the Hamiltonian which determines all states are determined by external potential, hence by $\rho(\mathbf{r})$.[70] To obtain the total energy using variational principle, a universal functional $F_{\text{HK}}[\rho(\mathbf{r})]$ is defined which is valid for any external potential V_{ext}:[70]

$$F_{\text{HK}}[\rho] = T[\rho] + E_{\text{ee}}[\rho] = \langle \Psi_\rho | T + V_{\text{ee}} | \Psi_\rho \rangle \tag{2.6}$$

The total energy functional $E[\rho, V_{ext}]$ satisfies the variational principle:

$$E_{GS} = \min_{\rho[\mathbf{r}]} E[\rho, V_{\text{ext}}] \tag{2.7}$$

where

$$E[\rho, V_{\text{ext}}] = \int d\mathbf{r}\, V_{\text{ext}}(\mathbf{r})\rho[\mathbf{r}] + F_{\text{HK}}[\rho] \tag{2.8}$$

The variation is performed in HK functional over all nondegenerate electron densities derived from the ground state of some external potential and can be generalized to minimization over the densities.[71]

With Kohn-Sham approach,[72] a much simplified approximation to the energy functional $E[\rho, V_{\text{ext}}]$ can be obtained: [70]

$$F_{\text{HK}}[\rho] = T_{\text{s}} + \frac{1}{2}\int d\boldsymbol{r}\, \Phi(\boldsymbol{r})\rho[\mathbf{r}] + E_{\text{xc}}[\rho] \tag{2.9}$$

for a system with electron density ρ, T_s is the kinetic energy for reference system of non-interacting electrons, Φ is the classical Coulomb potential for electrons, and E_{xc} is the exchange-correlation energy. Application of variational principle for Eq. (2.9) results in

$$\frac{\delta E[\rho, V_{ext}]}{\delta \rho(\boldsymbol{r})} = \frac{\delta T_s}{\delta \rho(\boldsymbol{r})} + V_{\text{ext}}(\boldsymbol{r}) + \Phi(\boldsymbol{r}) + \frac{\delta E_{\text{xc}}(\rho)}{\delta \rho(\boldsymbol{r})} = \mu \tag{2.10}$$

where μ is the Lagrange multiplier with the constraint of constant electron number. Considering a system with the same electron density ρ in an effective potential $V_{\text{eff}}(\mathbf{r})$ of non-interacting electons model,

$$\frac{\delta E[\rho]}{\delta \rho(\mathbf{r})} = \frac{\delta T_s}{\delta \rho(\mathbf{r})} + V_{\text{eff}}(\mathbf{r}) = \mu \tag{2.11}$$

Mathematically, the problems of Eq. (2.10) and (2.11) are identical, thus

$$V_{\text{eff}}(\mathbf{r}) = V_{\text{ext}}(\mathbf{r}) + \Phi(\mathbf{r}) + \frac{\delta E_{\text{xc}}(\rho)}{\delta \rho(\mathbf{r})} \tag{2.12}$$

While the solution of Eq. (2.10) is complicated, the solution of Eq. (2.11) can be obtained by solving the Schrödinger equation within a model of non-interacting particles,

$$\left[-\frac{1}{2}\nabla^2 + V_{\text{eff}}(\mathbf{r})\right]\phi_i(\mathbf{r}) = \epsilon_i \phi_i(\mathbf{r}) \tag{2.12}$$

and

$$\rho(\mathbf{r}) = \sum_{i=1}^{N} f_i |\phi_i(\mathbf{r})|^2 \tag{2.13}$$

where ϕ_i are the Kohn-Sham (KS) orbitals and f_i are occupation numbers. In contrast to non-local Hartree-Fock, local $V_{\text{eff}}(\mathbf{r})$ makes it numerically easier to solve the Kohn-Sham equations, because with such potential, there are efficient methods to solve self-consistent, single particle Schrödinger-like equations. However, the approximations of E_{xc} are unavoidable because their exact forms are unknown except for few very simple systems.

Kohn and Sham proposed the local density approximation (LDA): [72]

$$E_{\text{xc}}^{\text{LDA}} = \int d\mathbf{r}\rho(\mathbf{r})\varepsilon_{\text{xc}}[\rho(\mathbf{r})] \tag{2.14}$$

where $\varepsilon_{\text{xc}}[\rho(\mathbf{r})]$ is the exchange-correlation energy per particle of a homogeneous electron gas with density $\rho(\mathbf{r})$. Its generalized form for spin-polarized systems can be given as: [73, 74]

$$E_{\text{xc}}^{\text{LSDA}} = \int d\mathbf{r}\rho(\mathbf{r})\varepsilon_{\text{xc}}[\rho_{\uparrow}(\mathbf{r}), \rho_{\downarrow}(\mathbf{r})] \tag{2.15}$$

LDA is a good approximation for the cases where the density is almost constant, or at high densities where the kinetic energy dominates the exchange-correlation terms. However, LDA

does not appropriately describe chemical bonding. To overcome such deficiency of LDA, generalized gradient approximations (GGA) were proposed: [75-77]

$$E_{\mathrm{xc}}^{\mathrm{GGA}} = \int d\mathbf{r}\rho(\mathbf{r})\varepsilon_{\mathrm{xc}}\left[\rho(\mathbf{r}), \nabla\rho(\mathbf{r})\right] \tag{2.15}$$

In practice, $E_{\mathrm{xc}}^{\mathrm{GGA}}$ is usually split into its exchange and correlation contributions:

$$E_{\mathrm{xc}}^{\mathrm{GGA}} = E_{\mathrm{x}}^{\mathrm{GGA}} + E_{\mathrm{c}}^{\mathrm{GGA}} \tag{2.16}$$

One of the most commonly used GGA is PBE, which was developed by Perdew, Burke and Ernzerhof[78] without empirical fitting. PBE follows the so called "Jacob's ladder" where higher levels of functional builds on the experience of lower levels and satisfies particular physical constraints, thus it incorporates the LSD forms below it.

However, PBE is known to underestimate reaction barriers as well as band gaps. Both of them can be improved by hybrid functionals. Hybrid functionals include a contribution from Hatree-Fock exchange term. For example, PBE0, can be expressed as: [79]

$$E_{\mathrm{xc}}^{\mathrm{PBE0}} = E_{\mathrm{xc}}^{\mathrm{PBE}} + 0.25(E_{\mathrm{x}}^{\mathrm{HF}} - E_{\mathrm{x}}^{\mathrm{PBE}}) \tag{2.17}$$

And Heyd-Scuseria- Ernzerhof (HSE) functional can be expressed as: [80]

$$E_{\mathrm{xc}}^{\mathrm{HSE}} = 0.25E_{\mathrm{x}}^{\mathrm{HF,SR}}(\omega) + 0.75E_{\mathrm{x}}^{\mathrm{PBE,SR}}(\omega) + E_{\mathrm{x}}^{\mathrm{PBE,LR}}(\omega) + E_{\mathrm{c}}^{\mathrm{PBE}} \tag{2.18}$$

where SR and LR represent short range and long range components, and ω is an adjustable parameter governing the extent of short range interactions. HSE is equivalent to PBE0 for ω=0 and a pure PBE for $\omega\rightarrow\infty$.

2.2 Dispersion correction

One of the areas which are particularly challenging for DFT is the description of van der Waals interactions with "standard" approximations for exchange-correlation energy. A recent empirical correction to standard DFT (DFT-D3), which was proposed by Grimme *et al.*,[81] provides a consistent description of dispersion interaction for 94 elements H-Pu. Thus, it was applied in layered materials involved in this thesis where the van der Waals interactions are important.

The vdW-energy in the D3 scheme can be expressed as:

$$E_{\mathrm{disp}} = -\frac{1}{2}\sum_{i=1}^{N_{at}}\sum_{j=1}^{N_{at}}\sum_{\boldsymbol{L}}{}'\left[f_{d,6}(r_{ij,\boldsymbol{L}})\frac{C_{6ij}}{r_{ij,\boldsymbol{L}}^{6}} + f_{d,8}(r_{ij,\boldsymbol{L}})\frac{C_{8ij}}{r_{ij,\boldsymbol{L}}^{8}}\right] \tag{2.19}$$

where the summations are over N_{at} (atom number) and all translations of the unit cell $\boldsymbol{L}=(l_1,l_2,l_3)$; the prime indicates that $i\neq j$ for $\mathbf{L}=\mathbf{0}$; C_{nij} denotes the dispersion coefficient for the atom pair of ij, which are geometry-dependent and adjusted on the local geometry around the atom pair; $f(r_{ij})$ is a damping function to dump the contributions from interactions within typical bonding distance.

As for the damping function, the zero damping can be expressed as:

$$f_{d,n}(r_{ij}) = \frac{s_n}{1 + 6(r_{ij}/(s_{R,n}R_{0ij}))^{-\alpha_n}} \tag{2.20}$$

where $R_{0ij}=\sqrt{\frac{f_{d,8}(r_{ij,\boldsymbol{L}})}{f_{d,6}(r_{ij,\boldsymbol{L}})}}$; the parameters α_6, α_8, $s_{R,8}$ and s_6 are fixed at 14.0, 16.0, 1.0 and 1.0, respectively; s_8 and $s_{R,6}$ are adjustable parameters and functional dependent.

Another choice of damping function is Becke-Jonson (BJ) damping:[82]

$$f_{d,n}(r_{ij}) = \frac{s_n r_{ij}^n}{r_{ij}^n + (a_1 R_{0ij} + a_2))^n} \tag{2.21}$$

where a_1, a_2, s_6 and s_8 are adjustable parameters.

2.3 DFT+*U* method

The GGA fails to describe systems with strong electron-electron correlations. One solution is to use so called DFT+*U* method[83]. In such method, a non-local screened Coulomb potential, which is frequency-independent, is used to describe the non-local and energy-dependent self-energy. The DFT+U method can give, *e.g.*, the correct magnetic state for Cu-based superconductors such as La_2CuO_4. [83] It can also provide more reasonable band gaps than GGA with respect to experimental values.

In this thesis, the rotationally invariant DFT+*U* approach[84] is used for layered double hydroxides (LDHs). In this approach, the values of effective Coulomb interaction $U_{\text{eff}}=U-J$ instead of individual U and J values are used. The DFT+*U* energy can be expressed as:

$$E_{\text{DFT}+U} = E_{\text{DFT}} + E_U \tag{2.22}$$

where E_U is the effective on-site Coulomb interaction: [84]

$$E_U = \frac{U_{\text{eff}}}{2}\sum_{\sigma}\left[\sum_{j}\rho_{jj}^{\sigma} - \sum_{j,l}\rho_{jl}^{\sigma}\rho_{lj}^{\sigma}\right] = \frac{U_{\text{eff}}}{2}\sum_{\sigma}[\text{Tr}\rho^{\sigma} - \text{Tr}(\rho^{\sigma}\rho^{\sigma})] \tag{2.23}$$

where ρ_{jl}^{σ} is the density matrix of *d* electrons.

Practically, the values of U_{eff} for transition metals is system-dependent and usually obtained by fitting experimental data, and the U_{eff} in this thesis is taken from literature.[85]

2.4 Transition state searching

Many different methods have been proposed to find minimum energy path (MEP) and saddle points (transition state, TS).[86] The nudged elastic band (NEB) method [87, 88] is one of the efficient ways to find the MEP between a given initial state (IS) and final state (FS). NEB finds the MEP in a variational way. An elastic band with N+1 images is denoted as [$\mathbf{R}_0$, $\mathbf{R}_1$, …, $\mathbf{R}_N$]. The energy minima IS ($\mathbf{R}_0$) and FS ($\mathbf{R}_N$) are kept fixed while the rest N-1 intermediate images are adjusted during structural optimization. The total force which acts on an image is the sum of the spring force along the local tangent and the true force perpendicular to it (following the notation of ref [89]):

$$\boldsymbol{F}_i = \boldsymbol{F}_i^s|_{\parallel} - \nabla E(\mathbf{R}_i)|_{\perp} \tag{2.24}$$

where $\nabla E(\mathbf{R}_i)|_{\perp}$ is the true force which can be expressed as:

$$\nabla E(\mathbf{R}_i)|_{\perp} = \nabla E(\mathbf{R}_i) - \nabla E(\mathbf{R}_i) \cdot \hat{\boldsymbol{\tau}}_i \tag{2.25}$$

where E is the total energy of the system, as a function of coordinates of all atoms, and $\hat{\boldsymbol{\tau}}_i$ is the normalized local tangent at ith image. $\boldsymbol{F}_i^s|_{\parallel}$ is the spring force and given by:

$$\boldsymbol{F}_i^s|_{\parallel} = k(|\mathrm{R}_{i+1} - \mathrm{R}_i| - |\mathrm{R}_i - \mathrm{R}_{i-1}|)\hat{\boldsymbol{\tau}}_i \tag{2.26}$$

where k is the spring constant. Then an optimization algorithm can be used to move the images based on the force in Eq. (2.24). Usually there will be no images located at or even close to the saddle point and thus interpolation is necessary to evaluate the energy of the saddle point.

Thus, the climbing image nudged elastic band (CI-NEB) method was proposed to modify the NEB method.[89] In contrast to NEB, the shape of minimum energy path in CI-NEB remains, but an exact convergence to a saddle point is assured, without significantly consuming additional computational resource. The image with highest energy ($i_{\max}$) is obtained with the force given following instead of Eq. (2.24): [89]

$$\begin{aligned} \boldsymbol{F}_{i_{\max}} &= -\nabla E\left(\mathbf{R}_{i_{\max}}\right) + 2\nabla E\left(\mathbf{R}_{i_{\max}}\right)|_{\parallel} \\ &= -\nabla E\left(\mathbf{R}_{i_{\max}}\right) + 2\nabla E\left(\mathbf{R}_{i_{\max}}\right) \cdot \hat{\boldsymbol{\tau}}_{i_{\max}} \hat{\boldsymbol{\tau}}_{i_{\max}} \end{aligned} \tag{2.27}$$

The other method used for transition state searching in this thesis is dimer.[90] The dimer is a pair of images (at $\mathbf{R}_1$ and $\mathbf{R}_2$) separated by their common midpoint $\mathbf{R}$ and the distance of each image to $\mathbf{R}$ is ΔR. A unit vector ($\widehat{\mathbf{N}}$) pointing form $\mathbf{R}_2$ to $\mathbf{R}_1$ defines the dimer

orientation. If a transition state for a given initial configuration is started without prior knowledge of $\widehat{\mathbf{N}}$, then $\widehat{\mathbf{N}}$ will be assigned with a random unit vector and thus form the corresponding dimer images:

$$\mathbf{R_1} = \mathbf{R} + \Delta R\widehat{\mathbf{N}}; \qquad \mathbf{R_2} = \mathbf{R} - \Delta R\widehat{\mathbf{N}} \tag{2.28}$$

Whenever the dimer is relocated, the forces acting on the dimer as well as the energy of dimer are calculated from the energy and forces acting on the two images (denoted as $\mathbf{F}_1$, $\mathbf{F}_2$ and E_1, E_2, respectively). The energy of the dimer (E) is the sum of E_1 and E_2. The energy and the force acting on $\mathbf{R}$ (E_0 and $\mathbf{F}_R$) are calculated by interpolating between the images. $\mathbf{F}_R$ is simply the average of $\mathbf{F}_1$ and $\mathbf{F}_2$, while E_0 need to be estimated with $\mathbf{F}_1$, $\mathbf{F}_2$ and E_1, E_2. To derive E_0, the finite difference formula of curvature of the potential along the dimer (C) is needed:

$$C = \frac{(\mathbf{F_2} - \mathbf{F_1}) \cdot \widehat{\mathbf{N}}}{\mathbf{2}\Delta R} = \frac{E - 2E_0}{(\Delta R)^{\mathbf{2}}} \tag{2.29}$$

Thus E_0 can be derived from the equation above:

$$E_0 = \frac{E}{\mathbf{2}} + \frac{\Delta R}{4}(\mathbf{F_2} - \mathbf{F_1}) \cdot \widehat{\mathbf{N}} \tag{2.30}$$

It follows that all the properties of the dimer can be derived from $\mathbf{F}_1$, $\mathbf{F}_2$ and E_1, E_2, which minimize the total number of force evaluations necessary for saddle points.

2.5 Free energy calculation

A thermodynamic analysis of chemical processes requires the free energy calculations. In this thesis, the reaction free energy is approximated with harmonic vibrational frequencies, which are computed as the second derivatives of energy of atomic positions.

The free energy change of the reaction is:

$$\Delta G_{\mathrm{r}}(\mathrm{T}) = \sum (E_0 + H_{\mathrm{corr}}(T) - S_{\mathrm{vib}}T)_{\mathrm{products}} - \sum (E_0 + H_{\mathrm{corr}}(T) - S_{\mathrm{vib}}T)_{\mathrm{reactants}} \tag{2.31}$$

where ΔG_{r} is the reaction free energy, E_0 is the DFT energy at 0K, H_{corr} is the enthalpy corrections, S_{vib} is the vibrational entropy, T is the temperature. For adsorption complex, the difference of pressure-volume work between products and reactants is rather small which can be safely ignored.[91] Thus the H_{corr} can be replaced with the internal energy correction U_{corr}:

$$\Delta G_{\mathrm{r}}(\mathrm{T}) = \sum (E_0 + U_{\mathrm{corr}}(T) - S_{\mathrm{vib}}T)_{\mathrm{products}} - \sum (E_0 + U_{\mathrm{corr}}(T) - S_{\mathrm{vib}}T)_{\mathrm{reactants}} \tag{2.32}$$

where U_{corr} and S_{vib} are given based on vibrational frequencies: [91]

$$U_{\mathrm{corr}}(v_i, T) = \frac{1}{2}\sum_i h\nu_i + \sum_i h\nu_i \left[\exp\left(\frac{h\nu_i}{k_{\mathrm{b}}T}\right) - 1\right]^{-1} \tag{2.33}$$

$$S(v_i, T) = k_{\mathrm{b}} \sum_i \left\{\left(\frac{h\nu_i}{k_b T}\right)\left[\exp\left(\frac{h\nu_i}{k_b T}\right) - 1\right]^{-1} - \ln\left[1 - \exp\left(-\frac{h\nu_i}{k_b T}\right)\right]\right\} \tag{2.34}$$

where h is Planck's constant, k_{b} is Boltzmann's constant, and ν_i is the harmonic vibrational frequency.

Thus, $G_{A_{\mathrm{ads}}}$ is given as:

$$\Delta G_{\mathrm{r}}(\mathrm{T}) = \Delta E_0 + \Delta F_{\mathrm{vib}}(T) \tag{2.35}$$

where F_{vib}, the Helmoholtz vibrational energy, is given as the difference of U_{corr} and $S_{\mathrm{vib}}T$:

$$F_{\mathrm{vib}}(v_i, T) = \frac{1}{2}\sum_i \left\{h\nu_i + 2k_b T \ln\left[1 - \exp\left(-\frac{h\nu_i}{k_b T}\right)\right]\right\} \tag{2.36}$$

2.6 Photocatalytic water splitting

For photocatalysis, such as photocatalytic water splitting, critical parameters to evaluate the performance of a material as photocatalyst are the band gap, conduction band minimum (CBM) and valence band maximum (VBM) of such material. The band gap energy should range from 1.2 to 3.0 eV for enhanced absorbance of sunlight in this region; taken vacuum as reference and at pH=0, VBM should be lower than the oxidation potential of O_2/H_2O (-5.67 eV) while the CBM should be higher than the reduction potential of H^+/H_2 (-4.44 eV). The larger the difference between CBM (and VBM) and reduction (and oxidation) potential is, the stronger the reducing (oxidising) power will be.[12]

To evaluate the CBM and VBM, the work function is necessary and it can be calculated as:[92]

$$W = -\mathrm{e}\phi - E_{\mathrm{F}} \tag{2.37}$$

where e is the electron charge; ϕ is the electrostatic potential in the vacuum (practically larger than 15 Å in the vertical direction); E_{F} is the energy at the Fermi level of the material. With the calculated work function, the CBM and VBM are given as:

$$E_{\mathrm{CBM}} = -W + E'_{\mathrm{CBM}}; \qquad E_{\mathrm{VBM}} = -W - E'_{\mathrm{VBM}}; \tag{2.38}$$

where the E'_{CBM} and E'_{VBM} are the band edge positions with respect to the Fermi level.

2.7 Specific capacity and open circuit voltage calculations

Take lithium intercalation in MoS_2 as an example, the lithiation process can be described as:

$$Li^+ + e^- + MoS_2 \rightarrow LiMoS_2 \tag{2.39}$$

Thus the formation energy of lithiated MoS_2 is given as:

$$E_f = \frac{E_{tot}(Li_nMoS_2) - E(MoS_2) - n\mu_{Li}}{n} \tag{2.40}$$

where $E(MoS_2)$ is the energy of MoS_2, μLi is the chemical potential of Li taken as the cohesive energy per atom of bulk Li; $E_{tot}(Li_nMoS_2)$ is the total energies of lithiated MoS_2 structure; n is the number of Li atoms lithiated. According to Eq. (2.40), more negative formation energy indicates a more exothermic lithiation process.

Specific capacity and open circuit voltage (OCV) are two key parameters for modeling of alkali metal ion batteries. According to previous studies,[93] the maximal lithiation is obtained when OCV still remain positive. Thus OCV profiles are necessary to evaluate specific capacities: [93]

$$OCV = -\frac{\Delta G_r}{(x_2 - x_1)F} = -\frac{\left[G\left(Li_{x_2}MoS_2\right) - G\left(Li_{x_1}MoS_2\right) - (x_2 - x_1)G_{Li}\right]}{(x_2 - x_1)F} \tag{2.41}$$

where x_1 and x_2 are two different content, G is the Gibbs free energy of corresponding phase and F is the Faraday constant. However, currently most first principle modeling of batteries are simply using DFT energy instead of the free energy because the differences of entropy contribution and pressure-volume work are small at low temperature and thus frequently ignored: [94]

$$OCV = -\frac{\Delta E}{(x_2 - x_1)F} = -\frac{\left[E\left(Li_{x_2}MoS_2\right) - E\left(Li_{x_1}MoS_2\right) - (x_2 - x_1)E_{Li}\right]}{(x_2 - x_1)F} \tag{2.42}$$

where E is the DFT energy for corresponding phase.

Once the maximum number of ions with positive OCV is located, the specific capacity (J, in mAh g^{-1}) can be calculated as

$$J = \frac{Q \times F}{3.6 \times M} \tag{2.43}$$

where Q is the charge released, F is the Faraday constant, M is the molar mass of MoS_2 and 3.6 is the conversion ratio from mAh to coulomb. The computed specific capacities are often in reasonable agreement with experimental values.

2.8 *Ab initio* molecular dynamics

As implemented in VASP,[95] *ab initio* Born-Oppenheimer molecular dynamics (BOMD) based on DFT is given by the Lagrangian:[96]

$$L^{BO}(\mathbf{R},\dot{\mathbf{R}}) = \frac{1}{2}\sum_i M_i R_i^2 - U_{\mathrm{DFT}}[\mathbf{R};\boldsymbol{\Psi}^{\mathrm{sc}}] \tag{2.44}$$

where the nuclear coordinates are denoted as $\mathbf{R}=\{R_i\}$, and the dot denotes its time derivative; $U_{\mathrm{DFT}}[\mathbf{R};\boldsymbol{\Psi}^{\mathrm{sc}}]$ is the ground state energy (including ion-ion interaction) for the self-consistent (sc) electronic wave functions ($\boldsymbol{\Psi}^{\mathrm{sc}}$); $\boldsymbol{\Psi}^{\mathrm{sc}}$ is defined as $\boldsymbol{\Psi}^{\mathrm{sc}}=\{\psi_{nk}^{sc}\}$, where n and k are the band and reciprocal lattice vectors, respectively. The dynamical variables $\mathbf{R}(\boldsymbol{t})$ and $\dot{\mathbf{R}}(\boldsymbol{t})$ are given by the Euler-Lagrange equations:

$$\frac{d}{dt}\left(\frac{\partial L}{\partial \dot{R}}\right) - \frac{\partial L}{\partial \dot{R}} = 0 \tag{2.45}$$

The computational costly process to find the $\boldsymbol{\Psi}^{\mathrm{sc}}(t)$ is significantly simplified with an initial guess which is extrapolated from previous steps:[97]

$$\boldsymbol{\Psi}^{\mathrm{sc}}(t) = \mathrm{SCF}\left[\sum_{m=1}^{M} c_m\, \boldsymbol{\Psi}^{\mathrm{sc}}(t - m\delta t);\mathbf{R}\right] \tag{2.46}$$

2.9 Monte Carlo simulation

The Monte Carlo simulations[98] were used in this thesis to calculate the Curie and Néel temperatures. The core of Monte Carlo simulation is to investigate a system with random sampling. In brief, as for the simple Monte Carlo, the target quantity is the expectation value (μ) of a random variable (Y):

$$\mu = \mathrm{E}(Y) \tag{2.47}$$

Then values of Y_1, Y_2, …, Y_n are generated independently and randomly based on the distribution of Y, and their average are taken as the estimation of μ:

$$\hat{\mu}_n = \frac{1}{n}\sum_{i=1}^{n} Y_i \tag{2.48}$$

In practice, Y is commonly defined as $Y=f(\mathbf{X})$, where f is a real-valued function over $D\in\mathbb{R}^d$ and $\mathbf{X}$ is the random variable belonging to D with a probability density function $p(\boldsymbol{x})$, then:

$$\mu = \int_D f(\boldsymbol{x})p(\boldsymbol{x})d\boldsymbol{x} \tag{2.49}$$

It is easier to work with expectations for some cases while directly tackling integrals is simpler for other cases.

Some problems are remaining for the simple Monte Carlo even with all the variance reduction methods, one major problem is, the practical way to make independent samples of random inputs sometimes cannot be found. Markov Chain Monte Carlo (MCMC) methods[99] were developed to tackle such problem. In MCMC, a Markov chain with limiting distribution instead of independent points is used for sampling. Assuming a finite state space $\{x_1,\ldots, x_n\}$, the initial distribution is associated with $\boldsymbol{\lambda}=\{\lambda_1,\ldots,\lambda_n\}$:[99]

$$\Pr(\mathrm{X}_1 = x_i) = \lambda_i, i = 1, \ldots, n \tag{2.50}$$

and the transition probabilities are associated with a matrix P with elements p_{ij}:

$$\Pr(\mathrm{X}_{n+1} = x_j | \mathrm{X}_n = x_i) = p_{ij}, \qquad i = 1, \ldots, n \; and \; j = 1, \ldots, n \tag{2.51}$$

MCMC thus largely extend the area that Monte Carlo simulation can handle.

2.10 Computational details

Calculations with periodic models were performed at the density functional theory (DFT) level with the projected augmented wave (PAW) approximation, [78] as implemented in the Vienna ab initio simulation package (VASP).[95, 100, 101] PBE,[78] PBE0[79] and HSE[80] exchange–correlation functional were used in this work. The geometry optimizations were carried out at the PBE level which is considered sufficient for most solids.[102] The structural parameters optimized with PBE for systems investigated in this thesis are also in reasonable agreements with available experimental data. For the bulk forms of layered materials (in the cases of COFs and LDHs), the lattice parameters were fully relaxed. However, PBE is known to underestimate reaction barriers, as well as band gaps. Thus, PBE0 was used for barrier calculations and HSE06 was used for evaluation of band gaps of COF monolayers. For LDHs which are strongly correlated systems, DFT+U method was used for both structure optimizations and band gap calculations (in these cases, HSE was also found to overestimate the band gaps compared with experimental results). The kinetic energy cut-offs were chosen based on test; for all cases except COFs, a plan-wave cutoff of 500 eV were found sufficient; in the cases of COFs, an energy cutoff of 800 eV was necessary. D3 correction[82] was consistently used for dispersion correction. The choices of k-point sampling were based on tests and system-dependent. In this thesis, 2D models of monolayer are associated with a large vacuum (larger than 12 Å) to avoid the artificial interactions between periodic images.

Transition states on the reaction path were located with the climbing image nudged elastic band method (CI-NEB)[89] and the dimer algorithm[103] as implemented in Transition State Tools for VASP (VTST).[104] Vibrational frequencies were calculated for stationary points along the reaction path to identify the character of individual stationary points.

Molecular models were calculated with the Gaussian 09 program suite[105] with the PBE exchange-correlation functional with the TZVP[106] basis set. D3 correction was also used in all molecular calculations.

For the analysis of linker-linker interaction in COFs, SAPT-DFT [107, 108] calculations were performed with Molpro[109] using AVTZ basis set.

The Monte-Carlo simulations of Curie and Néel temperatures were performed with a Python script based on 2D Ising model (https://github.com/prtkm/ising-monte-carlo).

CHAPTER 3. Results and Discussion

3.1 Covalent organic frameworks

Covalent organic frameworks (COFs) are crystalline polymers with ordered pores.[15] Layered COFs formed by two-dimensional (2D) sheets and stabilised by interlayer stacking interactions have one-dimensional channels through 2D layers.[16, 17] COFs can be synthesized with designed skeletons and pores.[18-21] Numerous π-conjugated organic molecules allow the synthesis of COFs with tunable properties. The flexible tunability of their structures enables the optimisation of the band gap width, which renders COFs potentially applicable in photocatalytic water splitting.[22] Compared to their inorganic counterparts,[110] organic semiconductors such as COFs are superior because of their lower cost, ease of synthesis, mechanical flexibility,[12] higher concentration of reactive sites[13] and avoidance of heavy metal toxicity.[14]

3.1.1 CTF-type COFs

The covalent organic frameworks CFT-1, HPP and TzF have similar topology, their bulk structure consists of differently arranged two-dimensional layers, and they only differ in C:N ratio (4:1, 1:0 and 9:1, respectively). However, the three-dimensional stacking of these COFs, as well as their band gaps and band edge positions, remains poorly understood. Thus, we have systematically investigated these COFs using the density functional theory augmented with the dispersion correction term. We have analysed factors which affect the geometry of individual layers and their bulk arrangements, as well as the relationship between structure and photocatalytic properties.

3.1.1.1 COF monolayers

We first report the results for the isolated monolayers of each COF. Two important factors, the torsional and bending angles (for definition see Figure 2f) of the Bz linker, are essential to determine the structural stability of monolayers. The results shown in Fig. 2 indicate that the most stable structures of the isolated CTF-1 monolayers are planar (no visible buckling), while the torsional angle increases from TzF to HPP; buckling occurs only in some bulk structures but not in monolayers (see below).

To understand the effect of torsional and bending angles on layer stability, 2D potential surface scans were performed using Tz-3Bz and 4Bz models. The variations of energy as a function of torsional and bending angles are shown in Figure 3. All three torsional and bending angles were changed simultaneously from their equilibrium values. The minimum energy structures of Tz-3Bz and 4Bz have torsional angles 0° and 42°, respectively (Figure 3). The energy reflects changes in conjugation compensated for by changes in repulsion between close H atoms on neighbouring Bz rings.

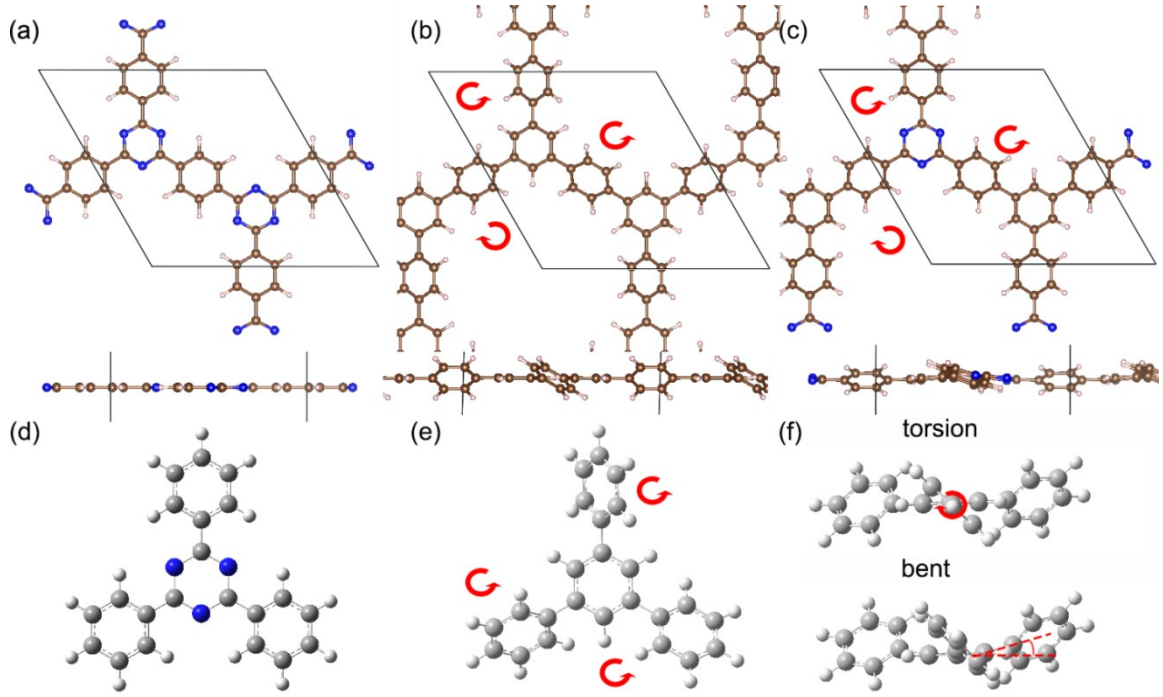

Figure 2: Top and side view of the most stable configurations of (a) CTF-1, (b) HPP and (c) TzF monolayers. Red arrows indicate the torsion of linkers. The most stable structures of 1, 3, 5-Triphenylbenzene and 2, 4, 6-Triphenyltriazine (molecular models corresponding to CTF-1 and HPP, respectively) are shown in (d) and (e), respectively. Note that both models are relevant for TzF. Torsional and bending angles are defined in (f). Nitrogen atoms are depicted as blue balls.

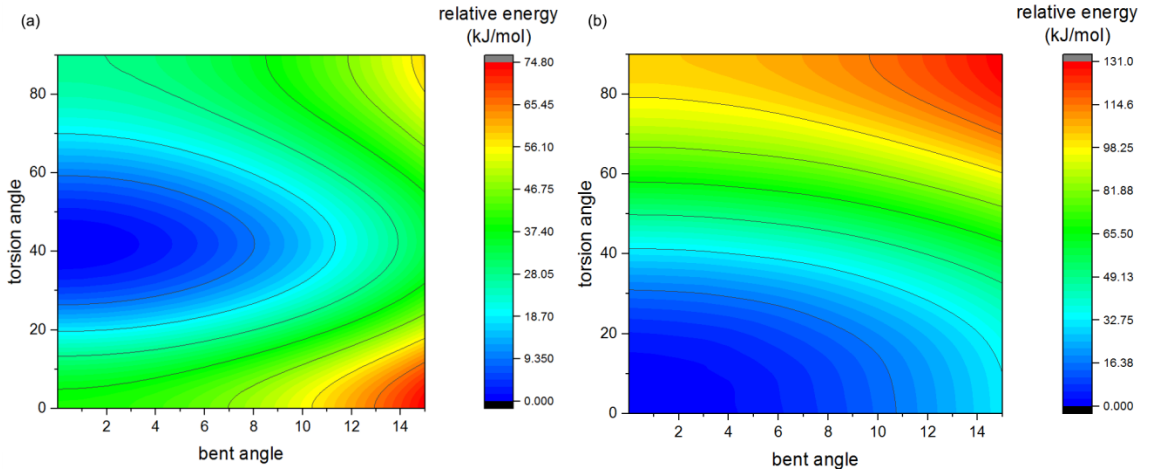

Figure 3: 2D potential energy profiles of torsion and bending angels of 4Bz (left) and Tz-3Bz (right) molecules.

3.1.1.2 Bulk structures

The following interlayer arrangements have been considered: AA eclipsed, AA serrated, AA inclined, AB staggered and AB helical (Figure 4).[111, 112-114] Using a unit cell consisting of 2 layers, the AA eclipsed configurations are stacked without any offset, while inclined and serrated configurations can be obtained with interlayer offset vectors oriented in the same or in the opposite directions, respectively. AB staggered and helical configurations can be obtained with interlayer offset vectors rotated by 180° and 60° along the surface normal, respectively. Three distinct directions (**x**, **y** and −**y**) were considered for the interlayer slip, as shown in Figure 4f. The most stable structures are slipped along either **x** or **y**, while slipping along the –**y** direction always leads to higher energy structures.

The torsional angles of bulk structures are similar to those observed in monolayer structures. While monolayers are not buckled, both unbuckled and buckled structures are found in each COF investigated. Interlayer interactions are driven by competition between geometry penalty (due to torsion and bending angles) and dispersion forces, and individual structures can be classified with respect to the dominant stabilisation motive between linkers. In analogy with the benzene dimer, we can distinguish parallel displaced and T-shaped (denoted PD and T respectively) arrangements.[115, 116] However, AB structures show interlayer interactions between connectors, while linkers are far apart. The interaction energies are summarised in Table 1, and slip directions and lattice parameters are summarised in Table 2. The results of individual COFs are discussed below, starting with the structurally simplest CFT-1, followed by HPP and TzF. The interaction energy is defined for per unit cell:

$$E_{\text{int}} = E_{\text{DL}} - 2 \times E_{\text{ML}} \tag{3.1}$$

where E_{DL} indicates the total energy of unit cells contains double layers, and E_{ML} indicates the energy of corresponding monolayer with a large vacuum.

Table 1: Interaction energies (E_{int}) of the most stable structures of HPP, TzF and CTF-1 for different interlayer arrangements.[a] The prevailing interlayer arrangement is shown in parenthesis—PD, T and PD/T (a mixed PD and T arrangement).

E_{int}	CTF-1	HPP	TzF	
			Tz-Tz	Tz-Bz
AA-eclipsed	—[b]	—[b]	−192(PD)	−205(PD)
AA-serrated	−222 (PD)	−214 (PD/T)	−221(PD/T)	−227(PD)
AA-inclined	−225 (PD)	−211(PD)	−219(PD/T)	−219(PD)
AB-staggered	−187 (PD)	−198 (T)	−183(T)	−190(T)
AB-helical	−205 (PD)	−266 (T)	−236(PD)	−240(PD)

[a] in kJ mol^{-1}. [b]Corresponding structure not found, not a minimum on the potential energy surface. Geometry optimisation ends in AA serrated structure.

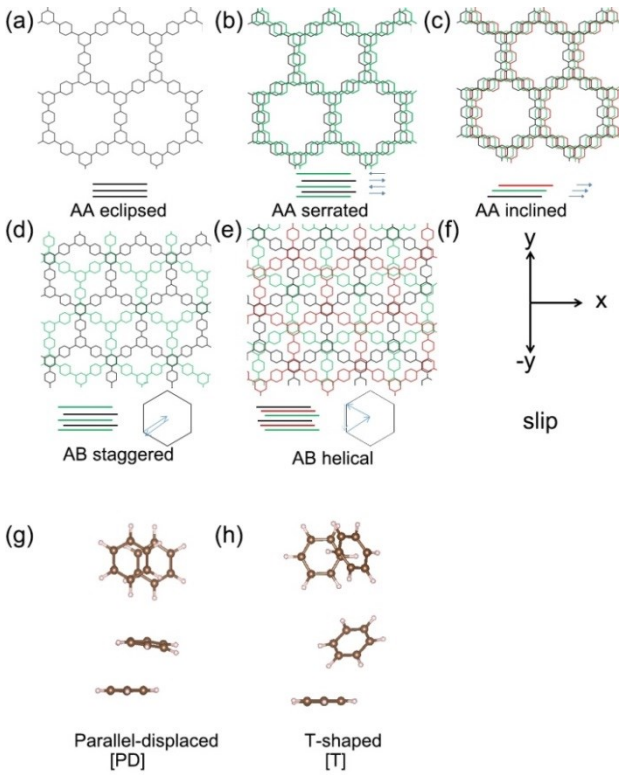

Figure 4: Schematic description of (a) AA eclipsed, (b) AA serrated, (c) AA inclined, (d) AB staggered and (e) AB helical interlayer structures. Arrows indicate the direction of layer shift. Different layers are shown in different colours. (f) Possible slips depending on symmetry; (g) PD and (h) T shaped arrangements of linkers.

Table 2: Lattice parameters (in Å) of most stable structures

	CTF-1	HPP	TzF	
			Tz-Tz	Tz-Bz
Monolayer	a=14.53	a=14.93	a=14.74	
AA-eclipsed	—[a]	—[a]	*a*=14.73, *c*	*a*=14.73, *c*
AA-serrated	*a*=14.53,	*a*=14.93, *c*	*a*=14.73, *c*	*a*=14.72, *c*
AA-inclined	*a*=14.53, *c*	*a*=14.94, *c*	*a*=14.70, *c*	*a*=14.70, *c*
AB-	*a*=14.52, *c*	*a*=14.93, *c*	*a*=14.73, *c*	*a*=14.72, *c*
AB-helical	*a*=14.43, *c*	*a*=14.73, *c*	*a*=14.61, *c*	*a*=14.59, *c*
Experimental	a=14.57[117]	—	a=14.75[118]	

[a]Corresponding structure not found; not a minimum on the potential energy surface; geometry optimisation ends in AA serrated structure; [b]x slip; [c]y slip; [d]no slip

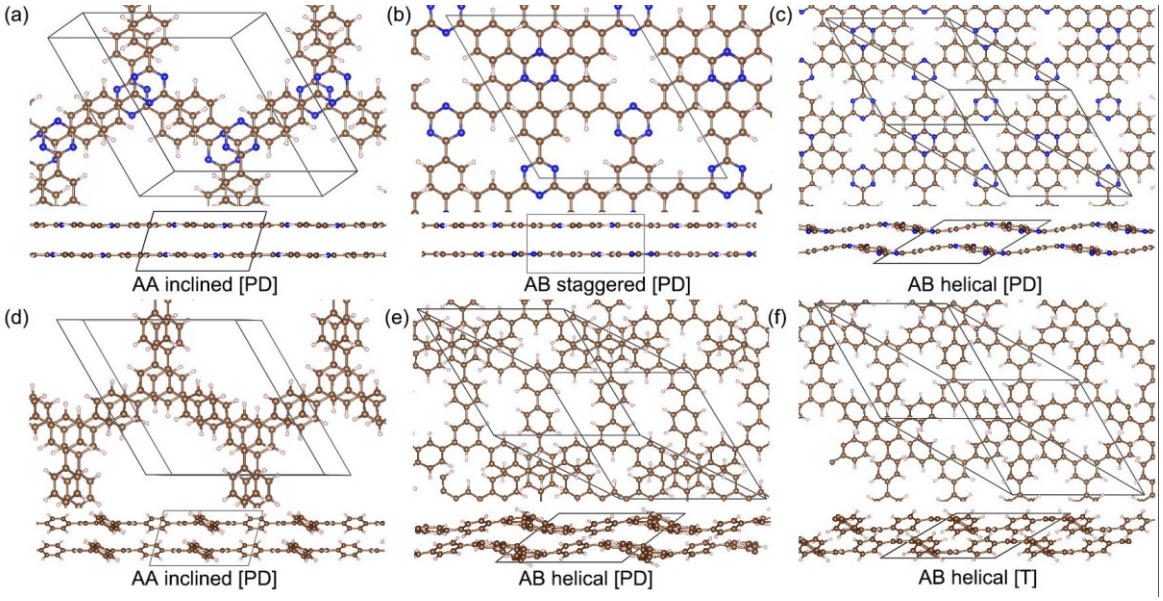

Figure 5: Top and side views of the selected structures of CTF-1 (a) (b) (c) and HPP (d) (e) (f). (a-f) shows the characteristic interlayer arrangements. PD and T stand for parallel-displaced and T-shaped arrangements, respectively.

CTF-1: Benzene linkers in CTF-1 are exclusively connected with Tz connectors; thus, there is no repulsion between hydrogen atoms on adjacent aromatic rings and, consequently, the CTF-1 structures have zero torsional angles and maximal in-plane π-conjugation. Four different structures were found for CTF-1. All CTF-1 structures have Tz units in adjacent layers in close proximity, except the staggered structures in which only half of the Tz rings are stacked on top of each other. The energetically most stable structures, AA-inclined (Figure 5a) and AA-serrated, have a PD arrangement between Tz and Bz units in subsequent layers. The other two structures of CTF-1, AB-staggered and AB-helical (Figure 5b and 5c, respectively), show a stacking arrangement of Tz units, and they are 38 and 20 kJ mol^{-1}

higher than the most stable AA-inclined structure. All planar structures have quite similar *a* vectors, while the *a* value of the buckled AB helical is lower. The comparison between the most stable AA- and AB-type structures (AA-inclined and AB-helical, Table 1) shows that the AA-inclined structure is 20 kJ mol^{-1} more stable, while its dispersion stabilisation (relative D3 correction values) is 26 kJ mol^{-1} smaller. The AB-helical structure shows significant buckling of individual layers (6º bending angle, Figure 5c), which increases interlayer dispersion interaction, but its geometry penalty is higher.

HPP: The structures of HPP are significantly more complicated than the structures of CTF-1 discussed above due to repulsive interactions between hydrogens on adjacent connectors and linkers and, therefore, all torsional angles are non-zero. Each linker is twisted either clockwise or anti-clockwise with respect to adjacent connecters. For each connector in the unit cell, only two combinations of torsional angle signs are possible: either all of them are the same, or one of the three has an opposite sign. Similarly, only two relative arrangements/twists between nearby linkers at adjacent layers are possible, thus leading to either PD- or T-type arrangements. Considering the above possibilities and the number of possible interlayer arrangements already discussed for CFT-1, a larger number of HPP structures was thus investigated, a subset of which is shown in Figure 6. The resulting structures are either of PD, T or mixed PD/T character (e.g., AA-inclined, AB-helical, and AA-serrated, respectively, Table 1). The most stable HPP structure is the AB helical [T] configuration without any slip (the structure shown in Fig. 4f, and the torsional angle arrangement is shown in Figure 6k). The AB helical configuration is 52 kJ mol^{-1} more stable than the AA serrated structure (Figure 6h). The large difference between the relative stabilities of AB helical [T] and other HPP structures results from the considerable difference in dispersion interactions (around 100 kJ mol^{-1}, see below).

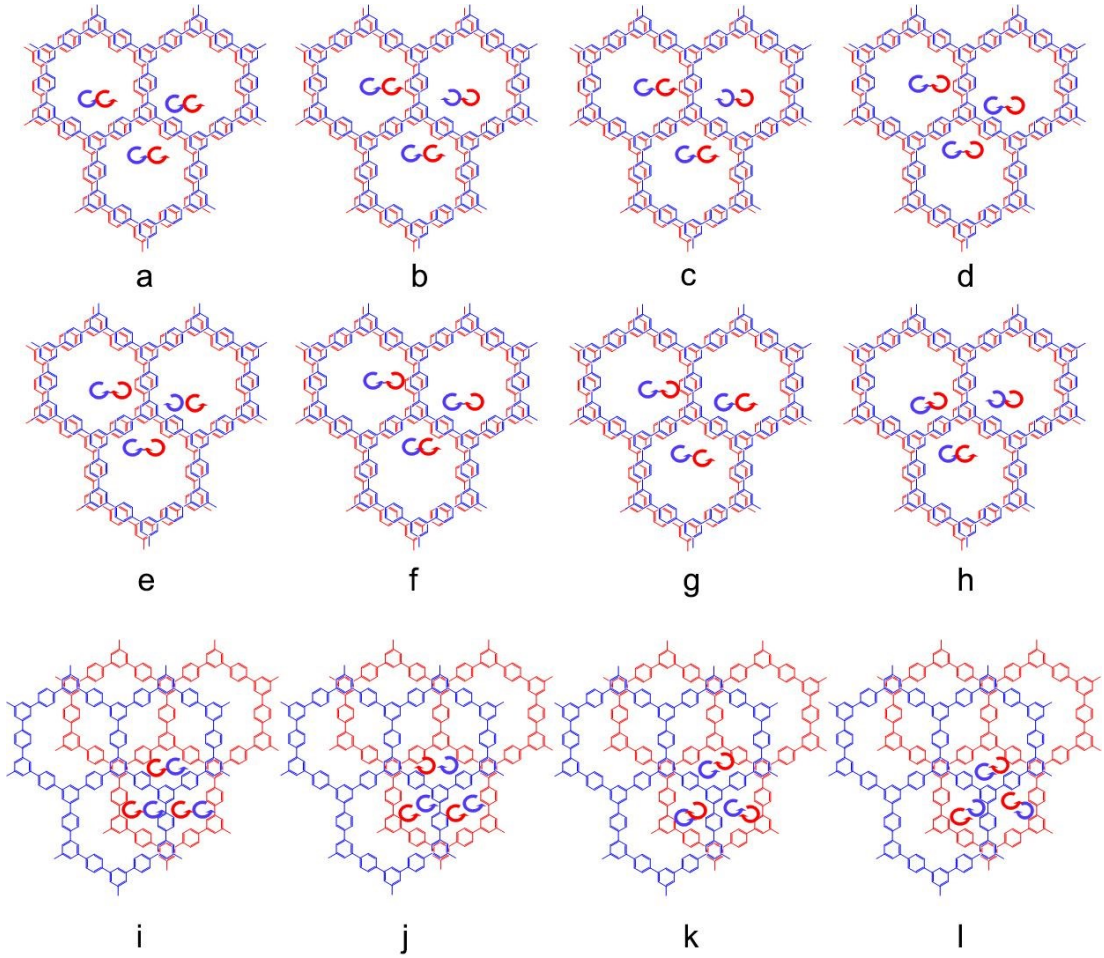

Figure 6: Structures of the HPP investigated: red and blue indicate different layers; the arrows indicate the torsion between the connector and the adjacent linkers. Red and blue arrows correspond to upper and lower layers, respectively; The PD arrangement occurs when they have the same direction, and the T arrangement otherwise. Note that **b** and **c** are similar arrangements, albeit with different offset distances.

TzF: Because TzF has two types of connectors (Tz and Bz), we have to distinguish two different interaction modes; structures are denoted Tz-Tz when the same connects are on top of each other, while the other structures are denoted Tz-Bz when Tz is interacting with Bz connectors in adjacent layers. The Tz-Tz and Tz-Bz arrangements of AA and AB structures of TzF are schematically depicted in Fig. 3.6. All possible slips were investigated, and similarly to CTF-1 and HPP, the structures are always either **x**- or **y**-slipped.

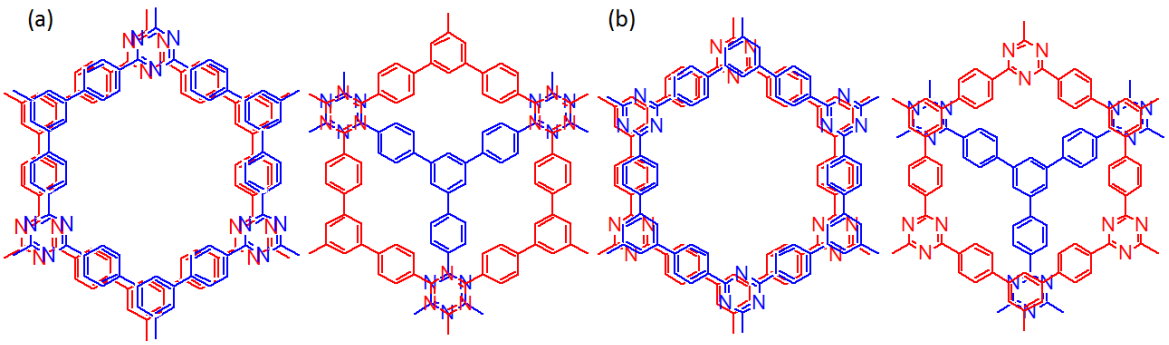

Figure 7: Schematic description of AA and AB structures for (a) Tz-Tz and (b) Tz-Bz arrangements of TzF.

The relative stability of individual structures increases in the following order for both Tz-Tz and Tz-BZ structures: AB-staggered < AA-eclipsed < AA-inclined < AA-serrated < AB-helical. The most stable structure (AB helical [PD], Figure 6i) is only slightly more stable than the AB helical [T] structures (8 and 7 kJ mol^{-1} for Tz-Tz and Tz-Bz, respectively). The structures of AA inclined [PD], AB helical [PD] and AB helical [T] are quite similar to those of HPP (Figure 5). The AB helical structures are more stable because of dispersion interactions, which are 107 and 94 kJ mol^{-1} (for Tz-Tz and Tz-Bz, respectively) larger than those of any other TzF arrangement. Without the D3 dispersion term, the AA serrated structure would be more stable than the AB helical structure.

3.1.1.3 Band gaps of bulk structures

PBE is known to underestimate band gaps, however, when the calculated band gaps are to be compared with experimental data, HSE and GW not necessarily perform better than PBE, which is summarized for a number of 2D materials in Table 3. In our case, the HSE band gaps of all 3 COFs are calculated as shown in Figure 8. HSE consistently shifts the CBM and VBM by about 0.3 and −0.6 eV, respectively. The band structures remain the same while the band gaps are shifted by about 0.9 eV. The HSE band gap of CTF-1 is 3.58 eV, and GW_0 value of CTF-1 is reported to be 5.44 eV,[119] which indicates CTF-1 monolayer is an insulator other than a semiconductor. However, we found it seems not the case considering experimental data became recently available: band gap of CTF-1 2D sheet (with a thickness up to 3 nm) is reported to be 2.48 eV.[120] From previous report,[12] the band gap of CTF remains almost constant from 2 layer to infinite (bulk), thus 2.48 eV should already represent the band gap of CTF bulk. Thus, CTF-1 bulk is semiconducting. To understand the difference

between the band gaps in monolayer and bulk COFs, we chose AA inclined structure of CTF-1 which has a period of 1 layer to do HSE calculations and found the PBE and HSE values are 2.33 and 3.12 eV, respectively, as shown in Figure 9. Indeed, the PBE value of 2.33 eV is still underestimating the band gap respect to the experimental 2.48 eV, however, HSE value of 3.12 eV is overestimating the band gap with a larger error for some reason. In conclusion, HSE and GW approach overestimate band gaps, while PBE underestimates that but it yields more reasonable results compared to experiment. For this reason, we stay with the PBE numbers for following discussion.

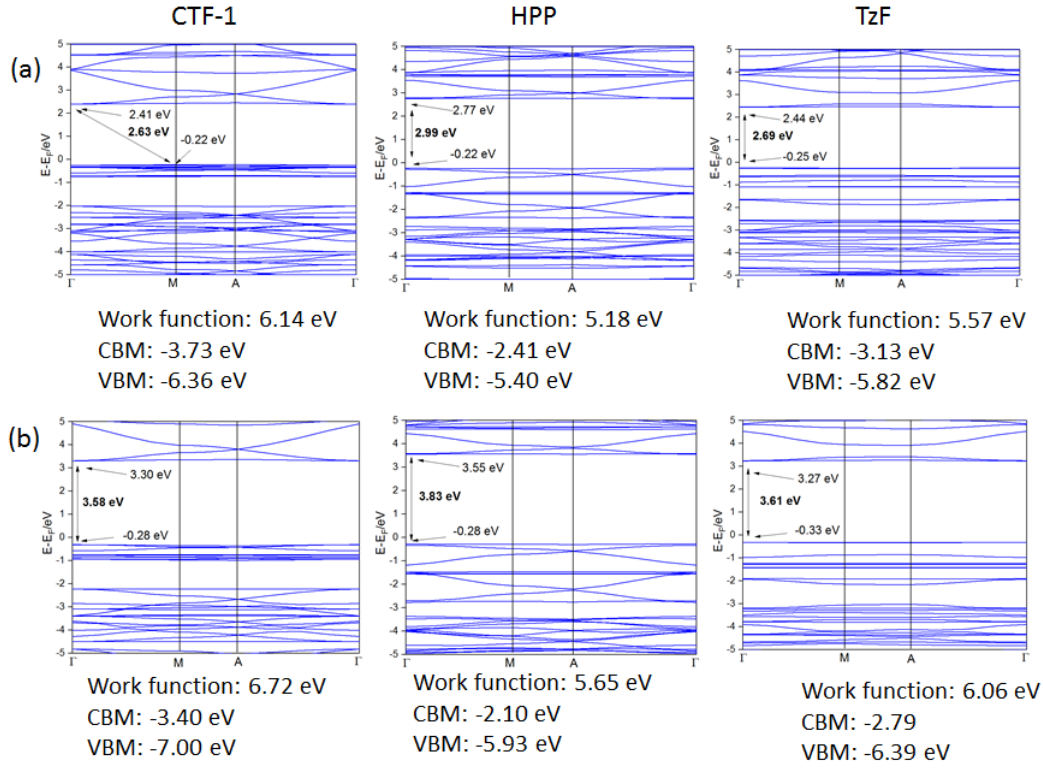

Figure 8: The work-functions and band gaps of CTF-1, HPP and TzF monolayers calculated with (a) PBE and (b) HSE.

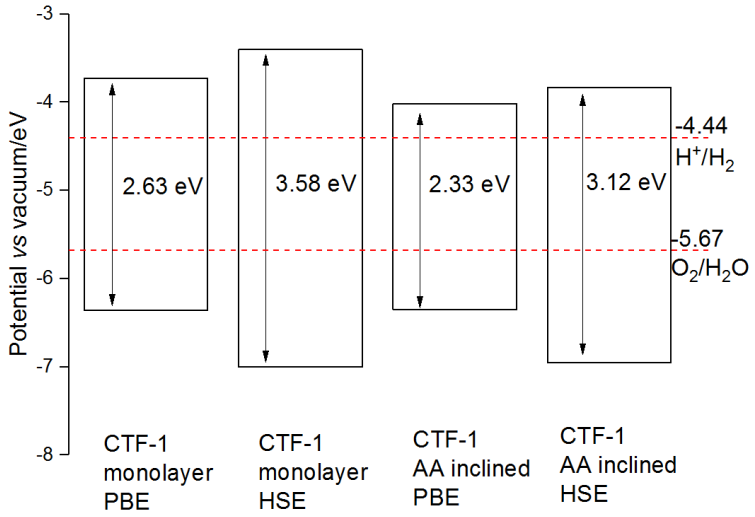

Figure 9: The PBE and HSE band gaps and band edge alignments for CTF-1 monolayer and AA inclined structure.

Table 3: Available theoretical and experimental band gaps (in eV) for monolayers of selected 2D materials

Materials	PBE	HSE	GW	Experimental
WS_2	1.81[a]	2.32[a]	2.91[a]	1.94[b]
MoS_2	1.67[a]	2.25[a]	2.66[a]	1.85[c]
$MoSe_2$	1.44[a]	1.99[a]	2.31[a]	1.54[c]
CTF-1	2.63[d], 2.67[e], 2.42[f]	3.58[d]	5.44[g]	—
HPP	2.99[d]	3.83[d]	—	—
TzF	2.69[d]	3.61[d]	—	—
CTF-0	2.49[f], 2.55[d]	3.32[f], 3.69[d]	—	—

[a]taken from ref[121]; [b]taken from ref[122]; [c]taken from ref[123]; [d]in this work;[e]taken from ref[124]; [f]taken from ref[12]; [g]taken from ref[119].

The calculated PBE band gaps (E_g) of the selected structures (including all structures from Table 1) are reported in Table 4. Our results clearly show that the band gaps calculated for monolayers are always larger than those calculated for bulk structures, and the difference is as large as 0.7 eV. The band gaps of CFT-1 bulk structures are approximately 2.3 eV (except AB helical, which is 0.2 eV smaller). The E_g calculated for HPP ranges from 2.30 to 2.69 eV, and T arrangements always have larger band gaps than PD arrangements. As discussed below in more detail (Section 3.1.1.5), T arrangements show larger geometrical deviation from planarity than PD arrangements. Thus, the decrease of conjugation in T arrangements is also more significant, which explains the larger band gaps in T arrangements.

Rather similar results were found for TzF in which T arrangements also have larger band gaps than PD arrangements; however, the differences in TzF are smaller than in HPP.

Table 4: Summary of band gap energies (E_g) of HPP, TzF and CTF-1 structures.[a] The prevailing interlayer arrangement is shown in parenthesis — PD, T and PD/T (a mixed PD and T arrangement).

Arrangement	CTF-1	HPP	TzF	
			Tz-Tz	Tz-Bz
Monolayer	2.63	2.99	2.69	2.69
Bulk				
AA-eclipsed	—	—	1.85 (PD)	1.99 (PD)
AA-serrated	2.34(PD) 2.37	2.47(PD/T)	2.24 (PD/T)	2.30 (PD)
AA-inclined	**2.33** (PD)	2.30(PD)	2.19 (PD/T)	2.23 (PD) 2.20
AB-staggered	2.30 (PD)	2.51(T)	2.42 (T)	2.35 (T)
AB-helical	2.10(PD)	2.31(PD), **2.69**	**2.27** (PD) 2.52	**2.27**(PD) 2.48(T)

[a] in eV.

3.1.1.4 Band edge alignments

Band gap, conduction band minimum (CBM) and valence band maximum (VBM) are critical parameters for photocatalytic water splitting, as described in Section 2.6.[12]

All calculated band gaps and band edge positions are shown in Fig. 7. The reducing and oxidising powers depend on the band edge positions (CBM and VBM). The valence band minima do not change when transitioning from monolayer to bulk structures. Therefore, band gap changes result from changes in CBM between monolayer and bulk structures. Monolayers always have higher CBMs than bulk structures. The oxidation/reduction behaviours of photocatalysts are also related to pH, as shown in Figure 10.[125] At pH=0, the alignment of VBM and CBM with respect to water oxidation is perfectly suitable for all CTF-1 structures, while the potential of TzF is smaller than that of CTF-1, and HPP can be ruled out as a suitable catalyst due to the VBM position. In contrast, at pH =7, HPP and TzF bulk structures have appropriately aligned CBM and VBM, while almost all CTF-1 bulk structures can be ruled out due to the CBM position. HPP structures have a stronger reducing power (larger CBM/reduction potential difference), and TzF structures have stronger oxidising power (larger VBM/oxidation potential difference).

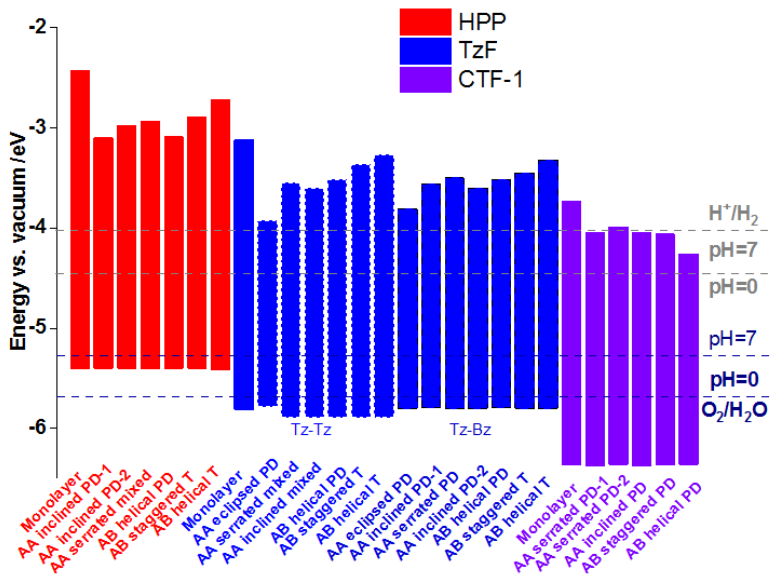

Figure 10: Band edge alignments of HPP, TzF and CTF-1. Grey dash lines indicate the standard H^+/H_2 reduction potentials, while blue dash lines indicate O_2/H_2O oxidation potentials at pH=0 and 7 (with respect to the vacuum level)

3.1.1.5 Discussion

The results from our systematic investigation of the Tz/Bz family of COFs (CTF-1, HPP and TzF) presented above show that : (i) decreasing nitrogen content increases the deviation from planarity of individual layers; (ii) increasing nitrogen content favours AA over AB layer structures; (iii) increasing nitrogen content favours the PD arrangement of linkers in adjacent layers over the T arrangement; (iv) dispersion interactions (evaluated from D3 corrections calculated for bulk structures) are always stronger in AB helical structures than in any type of AA structures; (v) COF layer arrangements have no direct effect on band gaps; (vi) band gaps increase with the interlayer distance. To explain these observations and the effect on photocatalytic water splitting, we have analysed the geometrical parameters and components of vdW interactions between layers.

Torsional and bending angles were identified as geometrical determinants of planarity and interlayer arrangements in the class of COFs investigated, as outlined in Table 5 for the most stable AA and AB structures. The torsional and bending angles of CFT-1 are close to zero for AA structures, while the bending angles of AB structures are always larger than 6°. In the case of HPP and TzF COFs, AA structures have smaller torsional and bending angles than AB structures. Considering the geometry penalty for bending and torsional angles (Figure 3), the energy destabilisation for geometrical reasons is higher for AB than for AA structures.

Tz-3Bz and 4Bz clusters (Section 3.1.1.1) were used to quantify this geometry penalty per unit cell (E_{gp}), and the details of E_{gp} calculations are given in Table 5 below. The summary of these results is presented in Table 6, first row.

Table 5: The summary of torsion and bent angles and relative energies of 4Bz and Tz-3Bz clusters for structures of HPP and TzF with PD and T shaped torsion. E_{rel} is the calculated relative energy of clusters. The angles are in degree and energies are in kJ mol^{-1}. The 3 values are denoting angles of 3 different linkers to the same connector. Geometry penalty calculation (HPP as example): T has energy penalty +23×4 (4 connectors per unit cell) = +92 kJ mol^{-1}, PD has +39×4=+156 kJ mol^{-1}.

	torsion angle[a]	bent angle	E_{rel}
CTF-1			
monolayer (Tz-3Bz)	0/0/0; 0/0/0	0/0/0	0
Tz-3Bz/AB helical [PD]	0/0/0; 0/0/0	6/6/6	+10
Tz-3Bz/AA	0/3/3;0/3/3	0/0/0	0
HPP			
monolayer(4Bz)	36/35/35;35/35/36	0/0/0	0
4Bz/AB helical [T]	32/32/31;33/33/33	8/8/8	+23
4Bz/AB helical [PD]	13/15/20;10/13/21	7/9/6	+39
4Bz/AA	42/28/24	1/1/3	+6
TzF			
monolayer(4Bz)	26/27/28;27/25/28	2/2/0	0
monolayer(Tz-3Bz)	14/18/18;14/19/18	4/4/0	0
Tz-Tz			
4Bz/AB helical [T]	27/27/27;25/25/25	8/8/8	+22
4Bz/AB helical [PD]	3/23/15; 2/22/16	0/8/6	+34
Tz-3Bz/AB helical [T]	24/24/24;26/26/26	7/7/7	+25
Tz-3Bz/AB helical [PD]	1/7/15; 2/10/15	4/6/3	+22
4Bz/AA	−20/19/34; −20/20/32	0/0/3	+4
Tz-3Bz/AA	16/20/−6;17/20/−6	4/4/2	+3
Tz-Bz			
4Bz/AB helical [T]	27/27/27;25/25/25	8/8/8	+21
4Bz/AB helical [PD]	8/23/23;3/23/23	0/8/6	+32
Tz-3Bz/AB helical [T]	24/24/24;25/26/26	7/7/7	+25
Tz-3Bz/AB helical [PD]	5/7/11;0/9/9	3/6/4	+23
4Bz/AA	23/25/−25;24/24/−26	4/4/0	+6
Tz-3Bz/AA	−2/10/13; −3/12/12	0/4/5	+3

Table 6: Geometry penalty, dispersion interaction energy, interaction energy calculated with PBE and total interaction energy (E_{gp}, E_d, E_{int}(PBE) and E_{int}, respectively) calculated for the most stable AA and AB structures (AB is always AB helical) are outlined in the top panel of the Table. The same set of characteristics calculated for T and PD arrangements are shown in the bottom panel of the Table.[a]

	CTF-1		HPP		TzF			
					Tz-Tz		Tz-Bz	
	AA	AB	AA	AB	AA	AB	AA	AB
E_{gp}	0	+40	+24	+92	+14	+112	+18	+110
E_{D3}	−284	−310	−269	−376	−272	−379	−285	−379
E_{int}(PBE)	+59	+105	+55	+110	+51	+143	+58	+139
$\boldsymbol{E_{int}}$**(**E_{int}(PBE)+ E_{D3}**)**	**−225**	**−205**	**−214**	**−266**	**−221**	**−236**	**−227**	**−240**
AB helical	PD	T	PD	T	PD	T	PD	T
E_{gp}	—	—	+156	+92	+112	+94	+110	+92
E_{D3}	—	—	−384	−376	−379	−361	−379	−362
E_{int}(PBE)	—	—	+167	+110	+143	+133	+139	+129
$\boldsymbol{E_{int}}$**(**E_{int}(PBE)+ E_{D3}**)**	—	—	**−217**	**−266**	**−236**	**−228**	**−240**	**−233**

[a] In kJ mol^{-1}.

The dispersion component of interlayer interaction energies (E_{D3}) was assessed as the difference between D3 empirical corrections calculated for bulk systems and the corresponding number of monolayers (Table 13, second row). For completeness, E_{int}(PBE), the interaction energies calculated at Perdew-Burke–Ernzerhof (PBE) level (without dispersion corrections) were also summarised in Table 6 (row 3). The results clearly show that the relative energies of AA and AB structures calculated at E_{int}(PBE) level are determined by the geometry penalty term E_{gp}. The overall stability of individual structures depends on the competition between dispersion stabilisation and geometry penalty. AB arrangements always have larger dispersion stabilisation energies than AA structures, and the difference in E_{D3} is small enough to be overruled by the geometry penalty only in CTF. Similarly, the large geometry penalty of PD arrangements in HPP structures results in the higher stability of the T arrangements, while dispersion contributions determine the higher stability of PD arrangements in TzF.

To understand better the preference for PD or T arrangements of linkers, a SAPT-DFT analysis of the pair of benzene linkers at geometries taken from the bulk structures of various interlayer arrangements of HPP was performed. The interaction energies of PD structures of benzene molecules are larger than −11 kJ mol^{-1}, while those of T arrangements are only about −8.5 kJ mol^{-1}, and this difference primarily derives from the dispersion term.

Band gap energy varies almost linearly as a function of the interlayer distance of CTF-1 in AB helical and AB staggered structures (Figure 11). At similar interlayer distances, the band gap is larger in buckled AB helical than in planer AB staggered arrangements due to a significant loss of conjugation. Thus, the band gap is modulated by conjugation but also by interlayer distance.

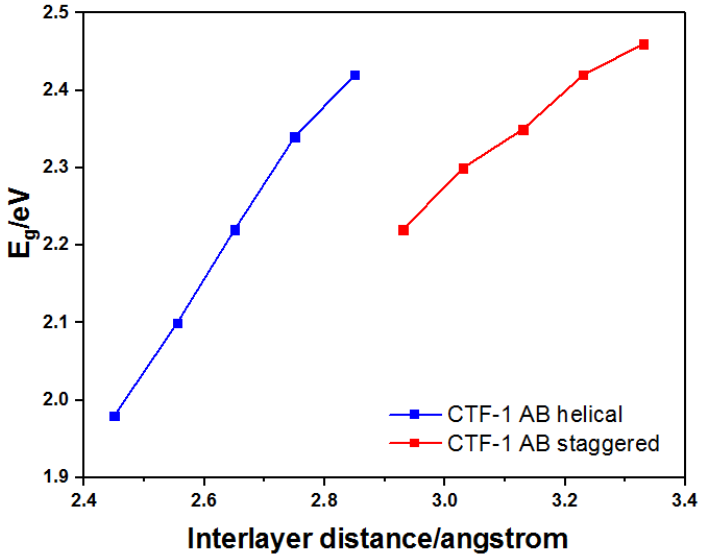

Figure 11: Band gap energy as a function of the interlayer distance of CTF-1 AB helical and AB staggered structures

The band gaps of ordered porous materials such as graphynes have been previously tuned by changing pore size.[126] Another way to tune the band gaps of COFs by changing interlayer arrangements is proposed herein. COFs with different layer arrangements can be prepared under different conditions, including solvent or catalyst, *e.g.*, CTF-1 can be prepared either as a AA structure via ionothermal synthesis in molten $ZnCl_2$,[117] or as a AB structure via solution synthesis at the interface of CF_3SO_3H/CH_2Cl_2. [120, 127] While a band gap of 2.48 eV was recently report for CTF-1 [120], band gaps of 1.91 and 2.24 were reported for a mixture of 2D TzF and 3D TzG,[118] in good agreement with our results. Our results also explain why highly crystalline COFs are so difficult to obtain experimentally: the relative energies of individual interlayer arrangements are often similar, particularly in CTF-1 and TzF. Indeed, experimentally observed XRD patterns show rather broad peaks.[118, 127] Our results also indicate that HPP, if properly synthesized, should show much higher crystallinity due to larger differences in the relative stabilities of individual structures.

We have shown that nitrogen ratio is relevant to the COF structures to influence the band gaps. It is necessary to check other relevant COFs without breaking of conjugation due to linkers. Thus, we have considered the monolayers of CTF-0a, CTF-0b and CTF-0c with C:N ratios 3:1, 1:1, and 1:0, respectively, as shown in Figure 12. They have similar topology as CTF-1 series but without linkers, which means the breaking of conjugation is eliminated. Even consider the longer conjugation distance (existence of linkers) which reduces the band gaps, we still found that the band gap decreasing trend upon increasing of nitrogen content holds in the series. This trend is qualitatively agree with previous report.[12] The only exception is CTF-0c, which has the C:N ratio 1:0 but band gap only 2.40 eV (previous reported PBE values are 2.42 eV[124] and 2.59 eV[12], respectively). However it might be caused by the planarity: in the case of HPP, if the planar structure is considered, the planar HPP has smaller band gap (2.54 eV)[124] than CTF-1. The larger band gap of HPP monolayer (2.99 eV) than CTF-1 in our case is due to the breaking of conjugation by the torsion of linkers. Thus it may not be surprising to find the band gap of CTF-0c smaller than CTF-0a because both of them are planar.

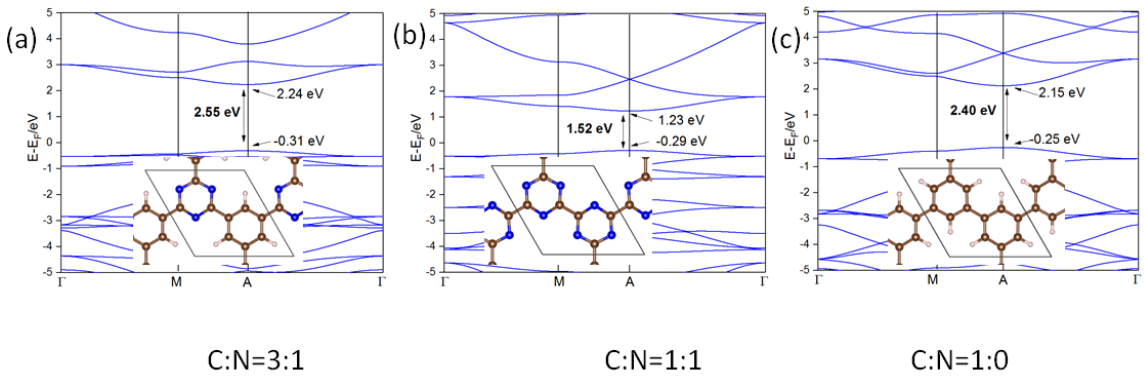

Figure 12: Band structures and band gaps of (a) CTF-0a, (b) CTF-0b and (c) CTF-0c.

Table 7: The band gaps (in eV) of monolayers of COFs with different C:N ratio

Materials	C:N ratio	band gaps
HPP	1:0	2.99
TzF	9:1	2.69
CTF-1	4:1	2.63
CTF-0a	3:1	2.55
CTF-0b	1:1	1.52

3.1.2 Solvation effects on stacking stability of CTF-1

The efficient methods to prepare 2D COF which have tunable structures and properties are still a challenge. A millimeter-size CTF-1 with layered structure was prepared recently via solution synthesis by our experimental collaborator.[120] Thus prepared CTF-1 crystal can be further exfoliated to thin crystal film. The obtained CTF-1 crystal shows a structure with AB stacking and pore size of $\approx$0.6 nm. Previously reported CTF-1 crystal synthesized via ionothermal method shows a structure with AA stacking.[117] Thus we investigated the structure stability of CTF-1 crystal with respect to different layer arrangements using DFT calculations. Results present in this section have been published in *Adv. Mater.* 2018, 30, 1705401 where more details about the topic can be found. This paper can be found as Attachment No. 1.

3.1.2.1 CTF-1 structures without solvent

In the absence of solvent, the AA and AB structures of CTF-1 is the same as those reported in Section 3.4 and summarized in Table 1. Thus, the AA stacking is more stable than AB one. This corresponds to the CTF-1 crystal synthesized via ionothermal method and showing the AA stacking. Relative stabilities of different stacking arrangement were also investigated computational with explicit solvent present in the pores using the same models as described in Section 3.1.1.

3.1.2.2 The influence of dichloromethane (CH_2Cl_2)

The solvent adsorption energies and the total interaction energies (interlayer interactions and solvent adsorption) were investigated for bilayer models with a vacuum.

The interaction energies for AA and AB bilayers are −104 and −83 kJ mol^{-1}, respectively. The adsorption energy is calculated as following:

$$E_{\text{ads}} = E_{\text{total}}(n\text{S} + \text{DL}) - nE(\text{S}) - E(\text{DL}) \quad (3.2)$$

where $E_{\text{total}}(n\text{S}+n\text{L})$ is the total energy of n solvent molecules (denoted as nS) adsorbed on layers, E(S) is the total energy for single solvent molecule, and E(DL) is the total energy of the bilayer structure.

The total interaction energy in the presence of solvent $E_{\text{int-S}}$ is calculated as following:

$$E_{\text{int-S}} = E_{\text{total}}(n\text{S} + \text{DL}) - nE(\text{S}) - 2E(\text{ML}) \quad (3.3)$$

where E_{total}(nS+DL*)* is the total energy of solvent/bilayer system, and E(ML) is the energy of monolayer.

The calculated adsorption energies and total interaction energies are shown in Table 8 for 1, 2 and 3 dichloromethane molecules. The adsorption energy of one dichloromethane molecule on monolayer is −22 kJ mol^{-1}. In the case of bilayer model (Table 8), it is −25 and −29 kJ mol^{-1} for AA and AB, respectively. The adsorption energy of dichloromethane in AB is slightly stronger than in AA, however, up to the adsorption of 3 molecules in the same pore (which is already quite crowded), this difference is not large enough to reverse the order of total interaction energies. Consequently, the presence of dichloromethane solvent does not change the relative stability of AA and AB arrangements.

Table 8: Adsorption energies and interlayer interaction energies[a] in the presence of solvent calculated for AA and AB stacking using bilayer (for dichloromethane) and bulk models (for triflic acid), respectively.

	AA		AB	
	E_{ads}	$E_{\text{int-S}}$	E_{ads}	$E_{\text{int-S}}$
CH_2Cl_2	−25	−129	−29	−112
2 CH_2Cl_2	−61	−165	−64	−147
3 CH_2Cl_2	−104	−208	−116	−200
CF_3SO_3H	−106[b]	−327[b]	−135[b]	−322[b]
2 CF_3SO_3H	−207[b]	−428[c]	−256[c]	−443[c]

[a] in kJ mol^{-1};[b]dissociative adsorption; [c] dimer adsorption.

3.1.2.3 The influence of triflic acid (CF_3SO_3H)

Triflic acid (CF_3SO_3H) is the other component of solvent used in the experimental protocol. As shown in Figure 13, the adsorption of triflic acid molecules is complicated: it can adsorb associatively, dissociatively, or as a dimmer. The corresponding adsorption energies (in the case of monolayer) are −46, −65 and −144 kJ mol^{-1}, respectively. In addition, the dissociative adsorption of two triflic acid molecules was also considered (−120 kJ mol^{-1}). For one molecule, the dissociative adsorption is already more favorable than the associative one (−65 *vs.* −46 kJ mol−^{1}). For two molecules, a dimer adsorption (one molecule dissociatively adsorbed) is more stable than the dissociative adsorption of both molecules (−144 *vs.* −120 kJ mol^{-1}). Thus only the dissociative and dimer adsorptions were considered in the bulk models of CTF-1.

Using Eq. (3.2) and (3.3), we have also calculated E_{ads} and $E_{int\text{-}S}$ for triflic acid molecules in bulk models as shown in Table 8. For one triflic acid molecule, its adsorption (dissociative) in AB structure is more favored than AA (−135 *vs.* −106 kJ mol−^{1}); nevertheless, the total interaction energy still slightly favors AA structure. Upon the adsorption of two triflic acid molecules as a dimer (Figure 14), the difference in adsorption energies of AA and AB structures is large enough (−207 *vs.* −256 kJ mol^{-1}) to stabilize the AB structure (−428 kJ mol^{-1} vs −443 kJ mol^{-1} for AA and AB, respectively).

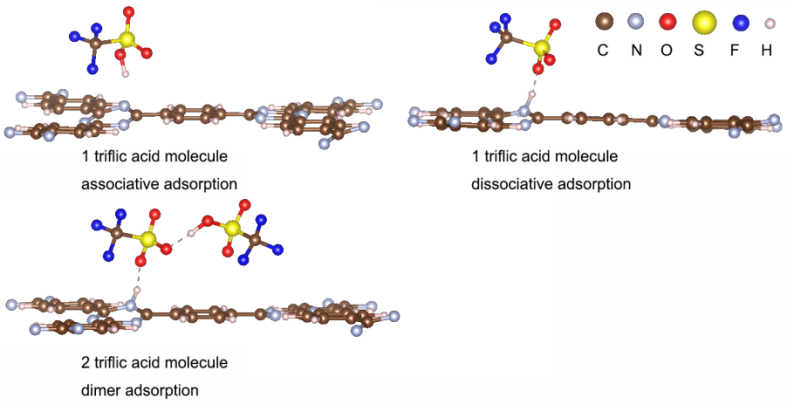

Figure 13: Three types of adsorption of triflic acid molecules (in the case of monolayer): associative, dissociative and dimer adsorption.

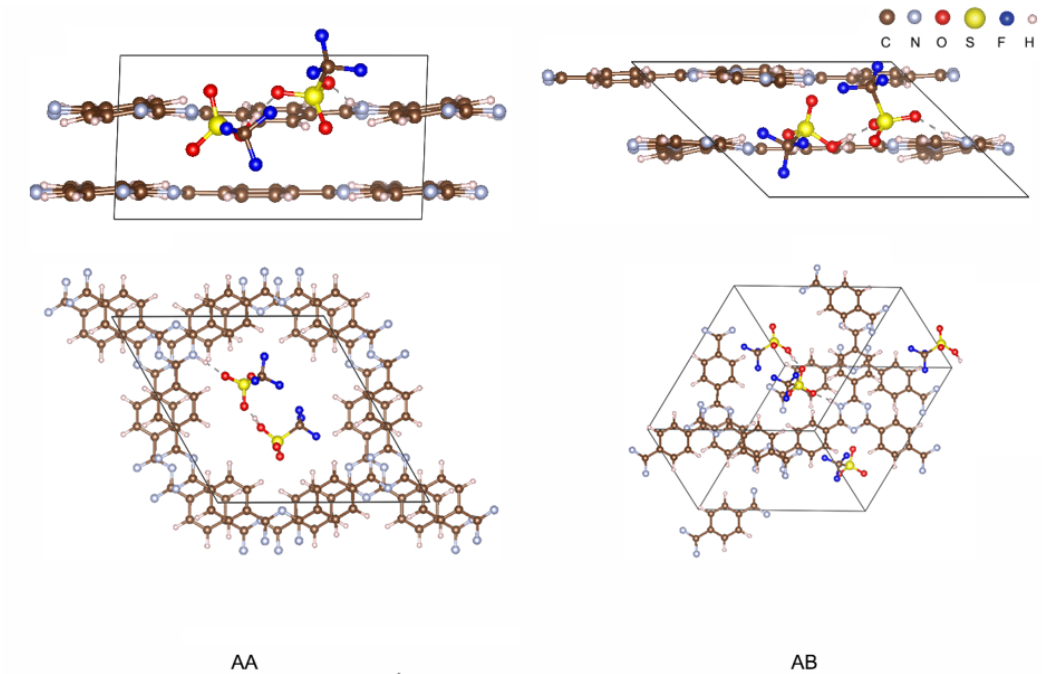

Figure 14: Adsorption of triflic acid molecules dimers on AA and AB structures.

3.1.3 Applications of COFs in collaboration with experiments

The flexibility of COF structures broadens the application scope of COFs, including alkali metal ion batteries and photocatalytic water splitting.[22] DFT calculations are able to provide atomistic insight into the performance of COFs in these areas. Thus we have done such investigations of COFs in collaboration with experiment. Results present in this section have been published in *Chem. Eur. J.* 2018, 24, 11916, *ChemSusChem* 2019, 12, 194 and *ACS Nano* 2019, 13, 2, 2473, where more details about the topic can be found. These papers can be found in Attachments No. 2-4.

3.1.3.1 Light-driven hydrogen evolution

Photocatalytic water splitting is a promising route towards clean energy. However, it remains a challenge to predict and design heterogeneous photocatalysts with sufficient efficiency for such process. Our collaborators synthesized a series of COFs with incorporated electron-donating sulphur-containing linkers and electron-withdrawing triazine units (C_3N_3). Therefore, we performed DFT calculations to optimize bulk structures and calculated their band structure.

The structure of sulphur- and nitrogen-containing COFs (denoted as SNP and NP, respectively) are schematically depicted in Figure 15. The corresponding atomistic structures of these COFs with an AA stacking are shown in Figure 16. The band structures of NPs and SNPs are calculated for the corresponding structures as shown in Figure 17. The calculated band gaps are in the range of 1.19~1.80 eV, which is in reasonable agreement with experimental values (1.9~2.52 eV).

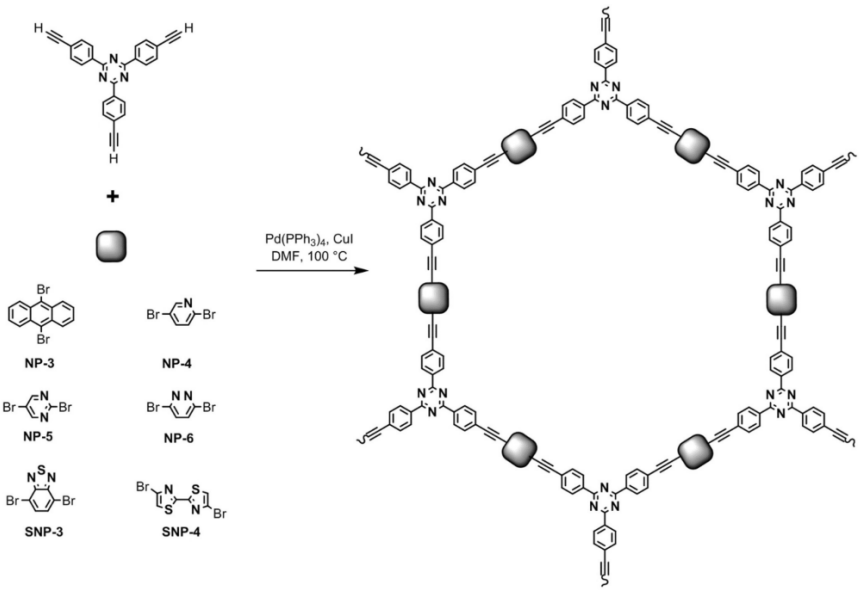

Figure 15: The scheme of NP and SNP synthesis

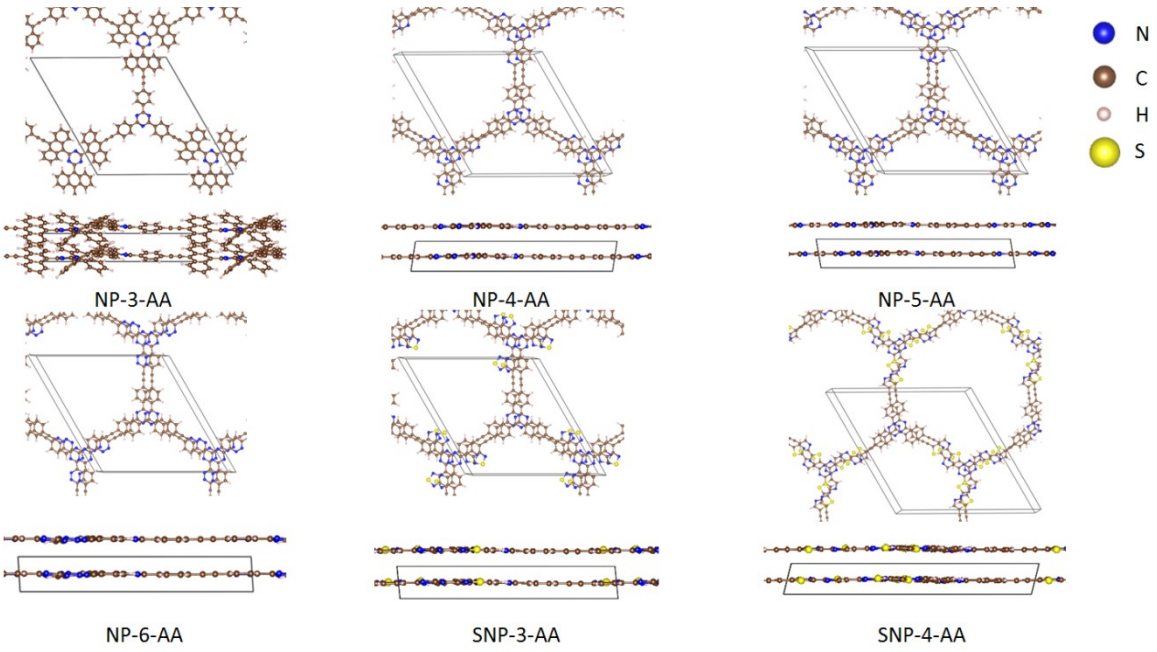

Figure 16: The top and side views of COFs with linkers corresponding to Figure 15

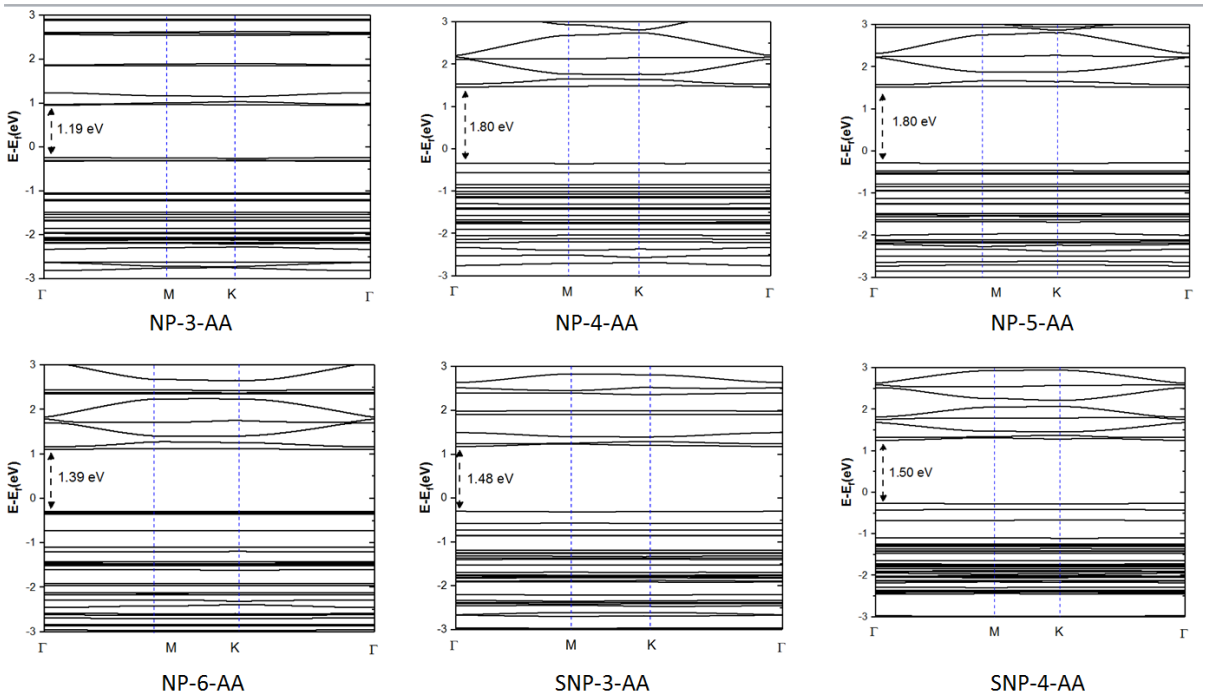

Figure 17: The band structures of NP and SNP COFs

3.1.3.2 Photocatalysis

Our experimental collaborators have synthesized a triazine-based graphdiyne (TzG) framework using different catalysts. To verify the structure of TzG, we have simulated the selected-area electron diffraction on optimized structures to compare with experimental results. The band structures were also calculated.

AA serrated, inclined and ABC (i.e. AB helical defined in Figure 18) structures of TzG were optimized and their lattice parameters as well as interaction energy (E_{int}) are shown in Table 9, as well as unit cell volume, accessible solvent surface area, pore volumes and densities. The structures and corresponding simulated SAED are shown in Figure 18.

Table 9: Interlayer interaction energies (E_{int}), lattice parameters, unit cell volume, accessible solvent surface area (S_{area}), pore volumes (V_{pore}) and densities for different TzG structures.[a]

structure	E_{int}	lattice parameter					UC volume	S_{area}	V_{pore}	density
		a	c	α	β	γ				
AA-1-serrated	−381	30.97	6.81	91	91	120	5617	2377	1.07	0.45
AA-1-inclined	−373	30.97	7.60	98	109	120	5548	2365	1.05	0.45
AA-2-serrated	−328	30.90	7.52	114	65	120	5431	2614	0.94	0.46
AA-2-inclined	−282	30.86	12.63	34	132	121	4944	3119	0.66	0.51
ABC	−336	30.81	35.75	31	149	120	3360	2102	0.13	0.75

[a]Energy in kJ mol^{-1}, distance in Å, angle in degree, volume in Å^3, S_{area} in m^2 g^{-1}, V_{pore} in cm^3 g^{-1}, density in g cm^{-3}

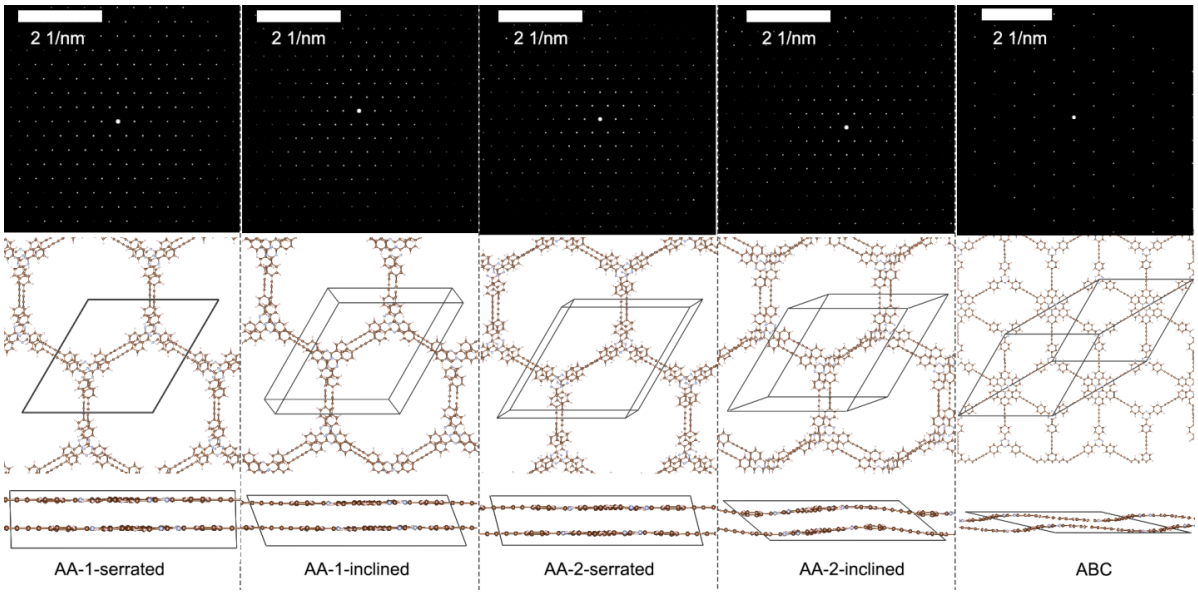

Figure 18: The simulated SAED, top and side views of sturctures of selected structures for TzG

Although AA is energetically most stable structure, the SAED of ABC matches best with experiment.

As we shown in Section 3.1.2, the structure stability may not only be determined by the interaction energy because other factors (such as solvent) may also have effect. Thus we calculated the band structures for both energetically most favored AA-serrated-1 and ABC which best matches with experimental SAED, as well as for the monolayer, as shown in Figure 19.

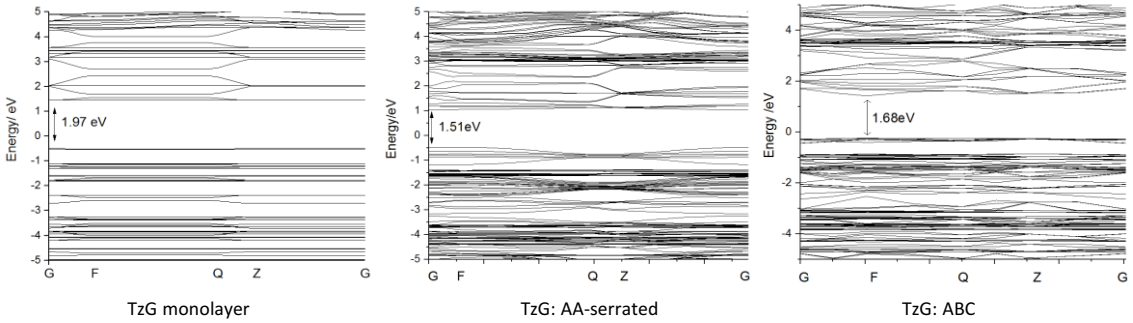

Figure 19: Band structures for TzG monolayers, AA-serrated and ABC structure.

3.1.3.3 Sodium ion battery

Our experimental collaborator synthesized the two-dimensional polyimide COFs via hydrogen-bond-induced preorganization and subsequent imidization reaction. It shows high capacity (312 mAh g^{-1} at 0.1 A g^{-1}), impressive rate and excellent cycling stability as a polymeric anode for sodium ion battery. We have explored possible structures and theoretical capacity at the DFT level.

According to experimental observation, the synthesized polyimide COF crystal consists of only few layers. The layer arrangement thus was considered within bulk models. The layer arrangements investigated are shown in Figure 20. Several stacking patterns including AA eclipsed, serrated, inclined and AB staggered (defined in Figure 4) were considered. The corresponding lattice parameters and interaction energy per unit cell (defined in Eq. (3.1)) are shown in Table 10. According to E_{int}, AB staggered is more stable than any of AA stacking structures. In addition, we simulated the XRD for most stable AA structure (AA eclipsed) and AB staggered structure. Compared to experimental results, it turns out that AB staggered structure shows better agreement with experimental data (see Figure 21). Thus, the AB staggered structure is more likely to be the actual structure of the polyimide COF investigated.

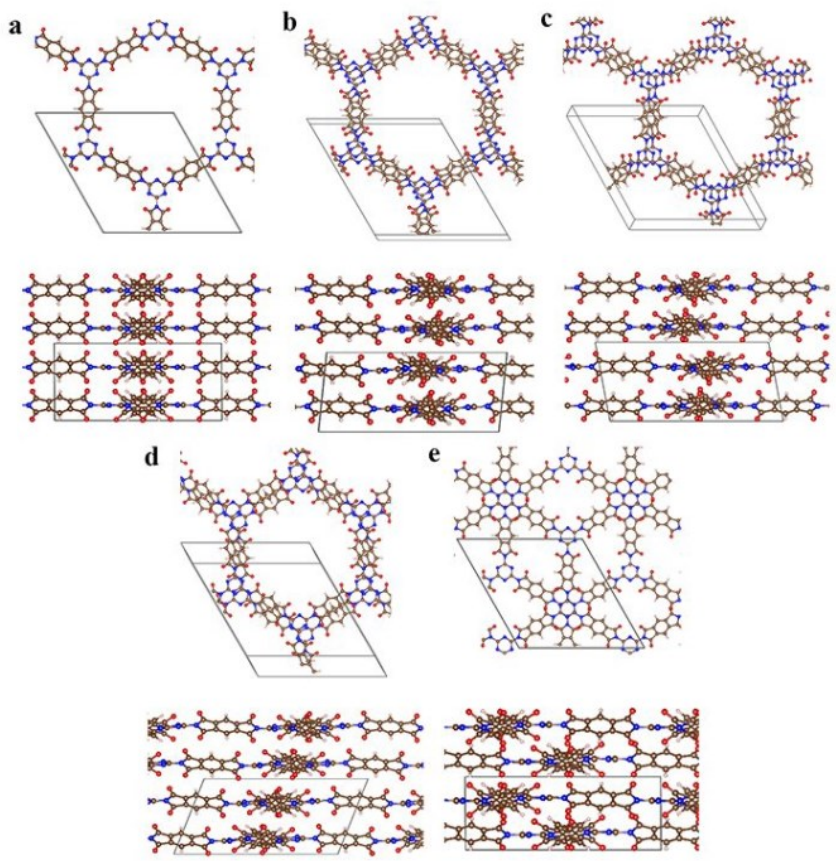

Figure 20: Top and side views of polyimide COF with stacking of (a)AA-eclipsed, (b) AA-serrated-1, (c) AA-serrated-2, (d) AA-inclined, (e) AB-staggered. C, N, O and H are shown as brown, blue, red and white balls.

Table 10: The lattice parameters and interaction energy per unit cell for the structures in Figure 20

stacking mode	E_{int}	lattice parameters				
		$a=b$	c	α	β	γ
AA-eclipsed	−242	21.00	8.42	90	91	120
AA-serrated-1	−208	20.89	8.13	83	93	120
AA-serrated-2	−219	20.79	8.60	96	97	119
AA inclined	−197	20.86	9.27	66	101	120
AB staggered	−262	20.99	6.86	90	90	120

[a]Energies, distances and angles in kJ mol^{-1}, Å and deg, respectively.

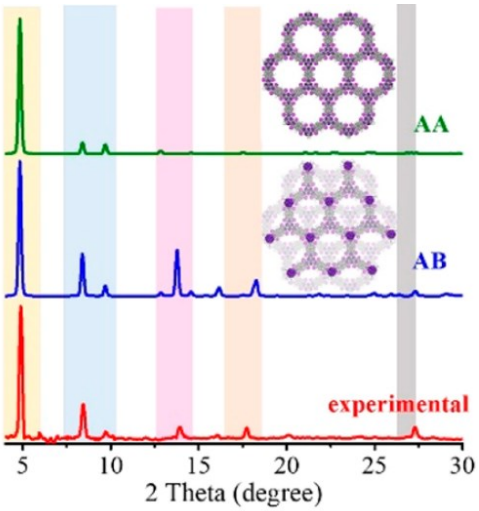

Figure 21: Experimental and simulated (eclipsed AA and staggered AB) XRD pattern of polyimide COF

To calculate the specific capacity and open circuit voltage, the monolayer and bilayer with AB staggered structure were used. The lattice constants ***a*** were optimized to 21.10 Å for monolayer and 20.85 Å for AB staggered bilayer.

As shown in Figure 22 and 23, sodium ions always favour specific sites on individual layer, *i.e.* the sites where a sodium ion could simultaneously interacts with 2 oxygen atoms and 1 nitrogen atom. For each individual layer, there are only 12 such sites. Calculated OCV profile (Figure 24) shows that OCV is above 0 for first 12 ions but it becomes negative for additional ions. Thus, the theoretical capacities for both monolayer and bilayer polyimide COF were 403 mAh g^{-1}.

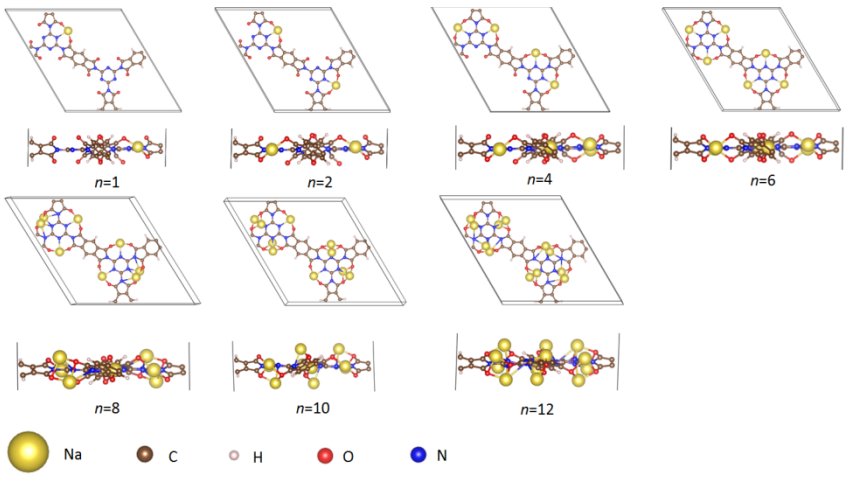

Figure 22: The top and side view of monolayer polyimide COF with *n* Na sodiated

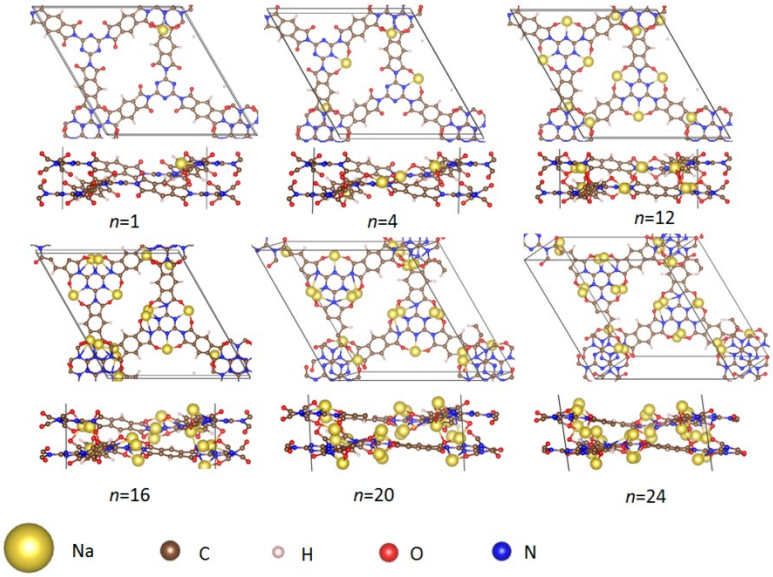

Figure 23: The top and side view of bilayer polyimide COF with *n* Na sodiated

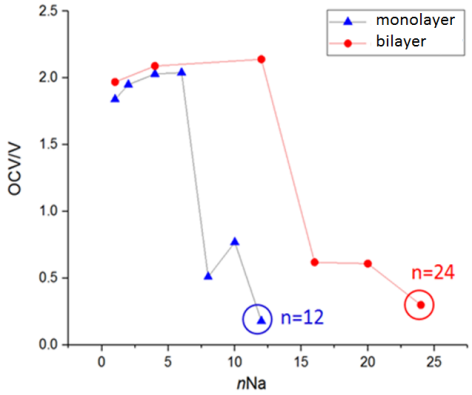

Figure 24: OCV profile for *n*Na on polyimide COF (*n* up to 12 for monolayer and 24 for bilayer)

3.1.4 Summary

COFs were investigated using DFT calculations for their structures, electronic structures and applications such as photocatalysis and sodium ion batteries.

First, our systematic computational investigation of CTF-1, HPP and TzF COFs revealed important relationships between COF chemical composition (C:N ratio) – intralayer buckling – interlayer arrangement – band edges position:

(i) Decreasing nitrogen content increases the deviation from planarity of individual layers due to the repulsion of H atoms on adjacent linkers and connectors.

(ii) Decreasing nitrogen content favours the buckling of individual layers in bulk structures. Consequently, AB structures are favoured over AA structures, and T arrangements are favoured over PD arrangements.

(iii) Dispersion interactions stabilise AB helical structures.

(iv) Increasing nitrogen content decreases both the valence band maximum and the conduction band minimum, which can be observed already in isolated COF monolayers (primary effect).

(v) Layer arrangements in bulk material affect the conduction band minimum, while the valence band maximum remains unaffected (secondary effect).

Decreasing conjugation (due to the torsion and bending of linkers) increases the band gap, while shortening the inter-layer distance reduces the band gap. Thus, band gaps and band edge positions can be modulated by specific layer arrangements. Calculations for the general performance of water splitting catalysis indicate that CTF-1 and HPP are suitable photocatalysts only at pH=0 and 7, respectively, while TzF could be used at both pHs.

The interlayer arrangements can be tuned with different synthetic methods, e.g. AA stacked CTF-1 can be obtained via ionothermal synthesis, and AB stacked CTF-1 can be prepared via solution synthesis. Thus next we have computationally investigated the influence of solvent molecules (dichloromethane and triflic acid) on the layer arrangements. According to our results, in the absence of solvent, AA structure of CTF-1 is more stable. The interaction of dichloromethane with CTF-1 layers is not strong enough to reverse the stability. The interaction of triflic acid molecules with CTF-1 layers is stronger and the adsorption stabilizes AB structures; upon the adsorption of 2 triflic acid molecules in the unit cell, AB is more stable than AA. Thus the residual triflic acid molecules in the crystal stabilize AB structures. Our results are also in agreement with the experimental observation (EDS) that triflic acid molecules are found across the as-synthesized CTF-1 crystal.

Finally, we have performed investigations on a few different COFs for their structures, electronic structures as well as their performance as sodium ion battery electrodes. Our results are in reasonable agreements with experiments and provide atomistic understanding of COF materials. Such knowledge is of practical importance with respect to design of COFs with optimal performance.

3.2 Silicene: lithium ion battery electrode

Silicene, the silicon analog of graphene, has a structure showing buckling that is due to the partial sp^3 type hybridization on Si.[25] Silicene was proposed as promising material for various applications, however, it remains a big challenge to obtain silicene with high quality because the sp^3 nature of Si complicates the spontaneous formation of silicene. Thus, silicene can only be synthesized with very limited methods such as epitaxial growth, other than conventional chemical or physical methods, which restricts relevant research and applications. Our experimental collaborators found the way of scalable preparation of high-quality silicene nanosheets via the oxidation and exfoliation of $CaSi_2$ in the liquid phase. The prepared silicene then has been applied as lithium ion battery anode and the specific capacity is 721 mAh g^{-1} at 0.1 A g^{-1} associated with excellent cycling stability, instead of rapid capacity decay as reported for most silicon anode materials. The experimental observation confirms that the silicene sheets are prepared as the single layer or sheets consisting of just few layers. Thus, we performed DFT calculations for monolayer and bilayer silicene in order to investigate their lithiation processes. Results present in this section have been published in *Adv. Mater.* 2018, 1800838, where more details about the topic can be found. This paper can be found in Attachment No. 5.

3.2.1 The structure of silicene monolayer and bilayer

According to the experimental observation, the silicene is either monolayer or a few-layer crystal with AA stacking order. For calculations we have used monolayer and bilayer models ($\sqrt{3} \times \sqrt{3}$ unit cells) and 4×4×1 Monkhorst-Pack grid.[128] The optimized lattice parameter ***a*** is 3.87 Å for both single and double layer models.

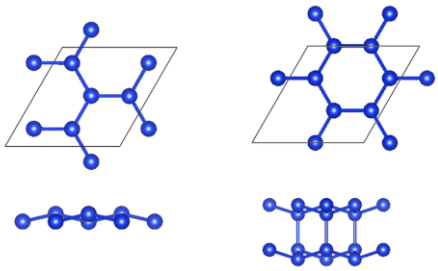

Figure 25: A top and a side view of monolayer (left) and bilayer (right) silicene with $\sqrt{3} \times \sqrt{3}$ unit cells.

3.2.2 The lithiation of silicene

A UC of monolayer model consists of 6 Si atoms, thus the lithiation with 1, 2, 3, 4, 5, 6 and 12 Li ions lead to the formula Li_xSi_{1-x} with x=0.14, 0.25, 0.33, 0.40, 0.45, 0.50 and 0.67, respectively. According to previous report,[129] the hollow site (Li stay above the centre of the hexagonal ring) and the site where Li stay above a Si atom are most stable. We found that the hollow sites are more stable (E_b=0.86 eV) with single Li, while the other site becomes more stable with 2 or more Li, as shown in Figure 26.

For bilayer, the formula of the model is $(Si)_{12}$, thus the lithiation with 1, 2, 4, 6, 9 and 12 Li ions leads to the formula Li_xSi_{1-x} with x=0.07, 0.25, 0.33, 0.43 and 0.50, respectively. As shown in Figure 27, the hollow sites are more stable up to 4 Li (corresponding to$Li_{0.25}Si_{0.75}$).

The formation energies over monolayer and bilayer are summarized in Figure 28. The surface of monolayer is fully covered with lithiation with 6 Li which corresponds to x=0.50 (see Figure 26). In such structure, both sides of monolayer are covered with 3 Li. If the number of Li on monolayer increased to 12 (corresponds to $Li_{0.67}Si_{0.33}$), although the E_f is still negative (−0.52 eV), the additional Li are clustering.

The surface of double layer is fully lithiated with 6 Li, corresponds to x=0.33. According to the results on single layer, additional Li on the surface would cluster instead of interacting with Si. Thus the additional Li are added to the interior space of bilayer. With 3 Li added, x increased to 0.43. But once x is increased to 0.50 (corresponds to 12 Li in total), Li in the interior space are also clustered.

Thus the fully lithiated monolayer and bilayer of silicene are represented by $Li_{0.50}Si_{0.50}$ and $Li_{0.43}Si_{0.57,}$ respectively.

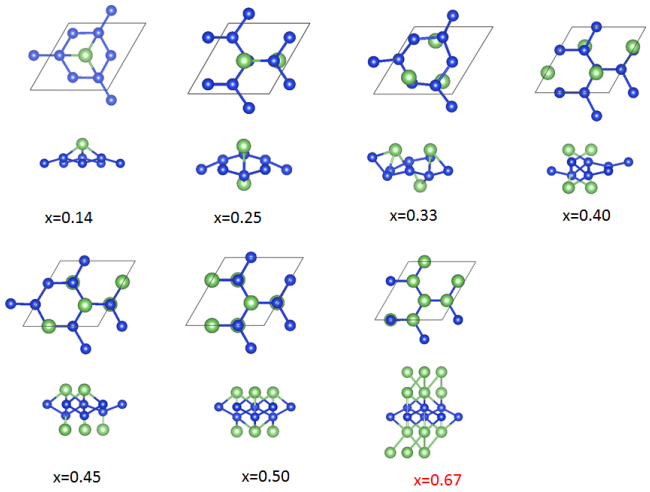

Figure 26: Top and side views of lithiated monolayer silicene, with the formula Li_xSi_{1-x} (x=0.14, 0.25, 0.33, 0.40, 0.45, 0.50 and 0.67)

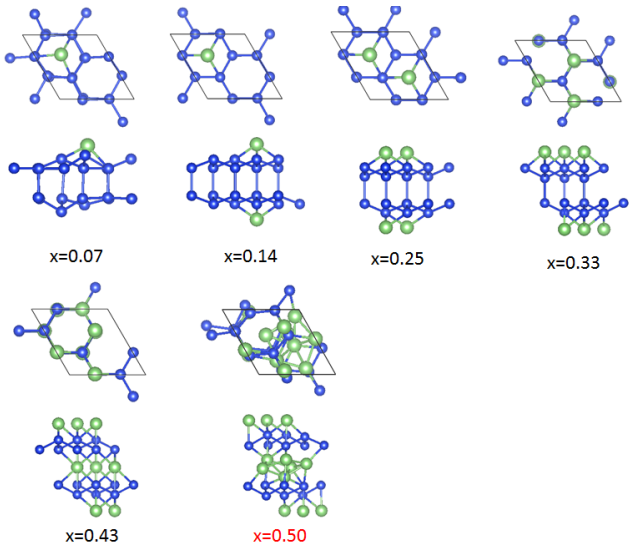

Figure 27: Top and side views of lithiated bilayer silicene with the formula Li_xSi_{1-x} (x=0.07, 0.25, 0.33, 0.43 and 0.50)

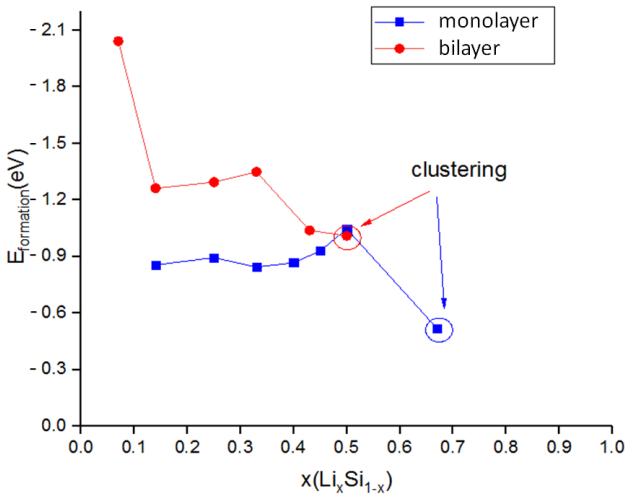

Figure 28: Formation energy profiles (E_b) of lithiation process as a function of Li content *x,* for monolayer and bilayer silicene

3.2.3 Summary

In this section, we show the fully lithiated monolayer and bilayer silicene have the formula of $Li_{0.50}Si_{0.50}$ and $Li_{0.43}Si_{0.57,}$ respectively. Thus theoretical specific capacity can be calculated according to Section 2.7. The calculated specific capacities of monolayer ($Li_{0.50}Si_{0.50}$) and bilayer ($Li_{0.43}Si_{0.57}$) are 957 and 722 mAh g^{-1}, respectively. The experimental capacity of silicene (721 mAh g^{-1}) is in good agreement with the theoretical capacity for bilayer silicene.

3.3 Transition metal dichalcogenides

Among a variety of semiconducting 2D layered materials, TMDs are one of the most intensively studied for their distinctly different properties compared to graphene. Although TMDs have been studied for decades,[36] the investigation of their 2D forms started only recently, owing to the development in material engineering that enables the preparations, measurements and operations on atomically thin films. Thus, the properties and applications of 2D TMDs are remaining to be explored using first-principle calculations.

3.3.1 Interlayer expanded MoS_2

Materials which may intercalate lithium ions have attracted increasing attention for their great potential as electrodes for lithium ion batteries.[130] However these materials have intrinsic upper limit of theoretical specific capacity, *e.g.* 167 mAh g^{-1} for MoS_2.[131] Such limitation

restricts the practical application of such materials despite their advantages in safety, rate capability and cycle life.[132] One solution is the interlayer engineering to expand the interlayer space, which has been performed on MoS_2.[133] However, the origin of the increased capacity is remaining unclear. Therefore, we collaborated with experimental groups to gain in-depth knowledge about the role of interlayer engineering in enhancing the lithium ion specific capacity. The hierarchical MoS_2 material investigated herein was synthesized with oxygen incorporation which has been recognized as effective approach to expand its interlayer space.[134] Such oxygen incorporated MoS_2 material shows a capacity of 220 mAh g^{-1} at 1 C rate, which is 32% higher than the theoretical upper limit of pristine MoS_2 (167 mAh g^{-1}). Electrochemical characterizations unambiguously confirm the increased capacity is due to the increase of amount of intercalated lithium ions, which is due to the expanded interlayer space. Thus we performed first-principle calculations to gain atomistic insight for the lithium ion intercalation in both pristine and interlayer expanded MoS_2.

The electrochemical impedance spectroscopy (EIS) results show that the lithium ion diffusion coefficients in O-MoS_2-1T are higher than those in pristine MoS_2-2H. In addition, the structure evolutions of both pristine MoS_2-2H and interlayer expanded O-MoS_2-1T during the battery cycling were monitored with ex situ XRD and the results indicate the latter is more stable than the former. The deconvolution of O-1s XPS spectra as well as Raman spectroscopy confirm the existence of Mo(IV)-O and Mo(V)-O bonds in O-MoS_2-1T. These bonds are inherited from the molybdate precursors during the hydrothermal synthesis. The incorporated oxygen atoms could either exist on the surface of MoS_2 as dopants (however it should has no influence on interlayer spacing) or exist in molybdenum oxide species in the interlayer space. Thus we also performed DFT calculations to evaluate the pillaring effect of molybdenum oxide species ($MoO_x(OH)_y$).

Results present in this section have been published in *Small* 2018, 14, 1803344 and *J. Mater. Chem. A*, 2019, 7, 1187, where more details about the topic can be found. These papers can be found in Attachment No. 6-7.

3.3.1.1 Pristine and interlayer expanded MoS_2

Slab models containing double layers were used with 3×3 supercells and 3×3×1 Monkhorst-Pack grid,[128] as shown in Figure 29. The *c* vector was set to be 20 Å for both structures to ensure a large enough vacuum. According to the experimental results, the pristine MoS_2 adopts 2H arrangement (denoted as MoS_2-2H, Figure 29) while the oxygen incorporated

interlayer expanded MoS_2 adopt 1T arrangement (denoted as O-MoS_2-1T) and the XRD patterns shows that there are two distinguish interlayer spacings for them. The MoS_2-2H model was fully relaxed and the interlayer distance was optimized to be 6.07 Å. The expansion of O-MoS_2 is due to molybdenum oxide species which will be discussed later. Thus, the interlayer distance of 1T model was fixed to 9.50 Å to simulate the experimental conditions. In addition, one of S atoms in MoS_2-1T is substituted by oxygen atom to build the O-MoS_2-1T model. The lattice constants *a* were optimized to 3.15 and 3.18 Å for pristine and O substituted MoS_2, respectively. During all calculations, atomistic positions and lattice parameters were fully relaxed while the volumes of super cells were fixed.

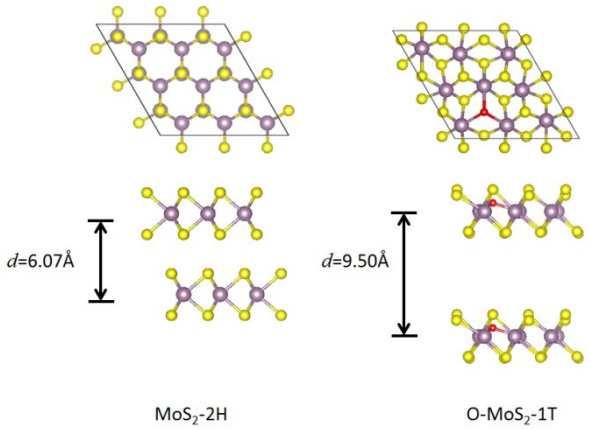

Figure 29: A top and a side view of MoS_2-2H and O-MoS_2-1T 3×3 supercells.

Two bulk structures of 1T MoS_2 were modelled for molybdenum oxide species to intercalate: 1T MoS_2 structures with (O-MoS_2-1T) or without (MoS_2-1T) oxygen atoms substituting the sulfur atoms on MoS_2 surface. 3×3×1 supercells of 1T MoS_2 were used associated with 3×3×3 Monkhorst-Pack grid. All the lattice parameters are relaxed during structure optimization. The interlayer distance of O-MoS_2-1T and MoS_2-1T are 5.88 and 5.81 Å, respectively, which are smaller than their 2H counterpart (6.07 Å), indicating that the interlayer expansion of MoS_2 is not possibly caused by the sulfur atoms substituted by oxygen.

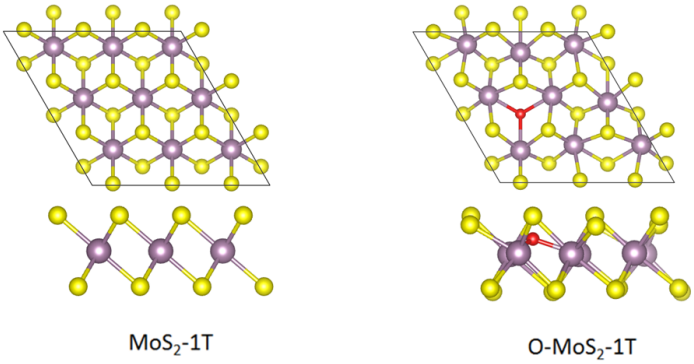

Figure 30: The top and side view of 1T MoS_2 supercells

3.3.1.2 Intercalation of lithium ions

The lithium intercalation process is considered within the interlayer spaces, which corresponds to $(MoS_2)_9$. Thus MoS_2-2H structures intercalated with n (n=1, 2, 3, 6, 9 and 10) lithium ions result in the formula Li_xMoS_2 where x=0.11, 0.22, 0.33, 0.67, 1 and 1.11, respectively. Similarly, O-MoS_2-1T intercalated with n (n=1, 2, 6, 12, 18 and 19) Li ions result in Li_xMoS_2 with x=0.11, 0.22, 0.67, 1.33, 2 and 2.11, respectively.

The intercalation structures, the formation energy profiles and OCV profiles of lithium ion intercalation in MoS_2-2H and O-MoS_2-1T are shown in Figure 31. For calculations of the formation energy and OCV see Section 2.7. The formation energies in O-MoS2-1T are always more negative than in MoS_2-2H at similar value of x indicating the intercalation process is more exothermic in O-MoS_2-1T. According to the calculated OCV profiles, OCV of O-MoS_2-1T is also higher than MoS_2-2H. The OCV of pristine MoS_2-2H change from positive to negative between x=1 and x=1.11, while in O-MoS_2-1T it remains positive up to x=2.11. Thus the calculated specific capacity (also see Section 2.7) is 167 mAh g^{-1} (x=1) for MoS_2-2H, which agrees with previous reported theoretical capacity of pristine MoS_2.[131] In the case of O-MoS_2-1T, the specific capacity calculated for x=2 is 334 mAh g^{-1}, and it is not the upper limit yet. The experimental value of 220 mAh g^{-1} is smaller than 334 mAh g^{-1}, possibly due to the interlayer molybdenum oxide species found in the interlayer space.

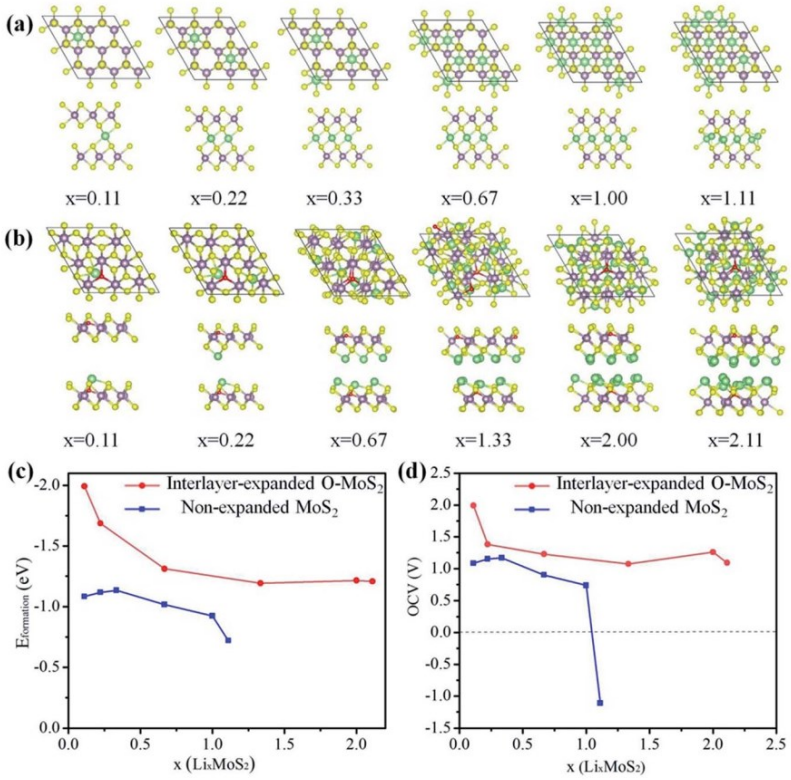

Figure 31: Top and side views of lithium ion intercalation structures in (a) MoS_2-2H and (b) O-MoS_2-1T. (c) The formation energy profiles for lithium ion intercalation in non-expanded MoS_2-2H and interlayer expanded O-MoS_2-1T. (d) The OCV profiles for lithium ion intercalation in non-expanded MoS_2-2H and interlayer expanded O-MoS_2-1T.

3.3.1.3 The change of interlayer distance with $MoO_x(OH)_y$ pillaring

The two model structures of 1T MoS_2 incorporated with molybdenum oxide species ($MoO_x(OH)_y$) are shown in Figure 32. For MoS_2-1T (without oxygen substitution on surface), the interlayer distances with incorporation of $Mo(OH)_4$, $MoO(OH)_3$, and $MoO(OH)_2$ are 10.01, 9.96, and 8.25 Å, respectively. Correspondingly for O-MoS_2-1T (one sulfur atom substituted by oxygen), the interlayer distances are 9.99, 10.42, and 8.06 Å, respectively. The interlayer distances are significantly enlarged compared to pristine MoS_2 and O-MoS_2-1T (5.82 and 5.88 Å, respectively) upon incorporation of molybdenum species investigated. In addition, the interlayer distances associated with incorporation of $Mo(OH)_4$ and $MoO(OH)_3$ agree well with the XRD and TEM measured values (~10.2 Å) with error smaller than 3%, whereas the $MoO(OH)_2$ incorporated structures result in a larger errors (>10%).

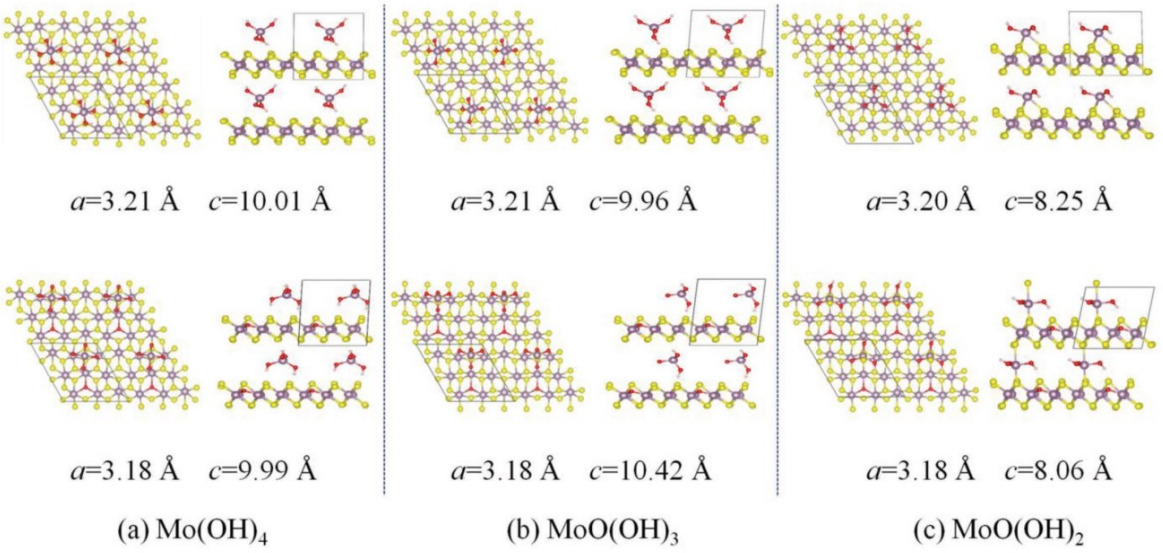

Figure 32: The top and side views of MoS_2 and O-MoS_2 structures incorporated with molybdenum species of (a) $Mo(OH)_4$, (b) $MoO(OH)_3$, and (c) $MoO(OH)_2$), with corresponding lattice parameters (*c* indicates the interlayer distance).

3.3.2 Fe-embedded $PtSe_2$

CO oxidation catalysts have been extensively studied because they are of practical importance, *e.g.* to remove the catalytically poisoning CO in fuel cells.[135, 136] In particular, the single-atom catalysts (SAC),[137] where individual metal atom anchored on the substrate as the catalytically active site, can efficiently catalyze CO oxidation under mild conditions. Thus $PtSe_2$ monolayer with a single transition metals (Sc-Zn) embedded at the Se vacancy were computationally investigated as CO oxidation catalyst candidates. The best candidate chosen was further investigated in details for the reaction mechanisms. Results present in this section have been published in *RSC Adv.*, 2017, 7, 19630-19638, where more details about the topic can be found. This paper can be found in Attachment No. 8.

3.3.2.1 Screening the candidates for CO oxidation

The model of pristine $PtSe_2$ monolayer is shown in Figure 33 together with the localized densities of states (LDOS) projected on Pt-6s, Pt-5d and Se-4p orbitals.

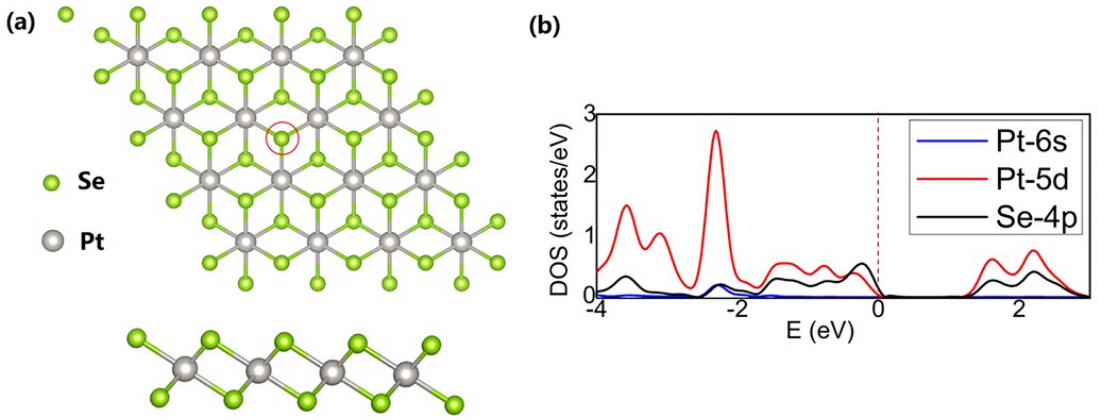

Figure 33: (a) A top and a side view of $PtSe_2$ monolayer. The position of Se vacancy (to be replaced) is denoted by the red circle. (b) DOS projected on the Pt(5d), Pt(6s) and Se(4p) orbitals. The Fermi level (E_f) is indicated by a brown dash line.

The structure parameters of TM (Sc-Zn) embedded $PtSe_2$ monolayer (denoted as TM-PtSe2) are shown in Table 11. They were screened to choose suitable candidates for CO oxidation according to the criteria stated for the same purpose previously:[138] (i) the overall barrier of CO oxidation should be lower than 96 kJ mol^{-1} to make it possible to proceed under mild conditions; (ii) the adsorption of O_2 molecule on the catalyst should be stronger than adsorption of CO molecule to avoid catalytic poisoning; (iii) the adsorption energy of produced CO_2 should be weaker than –50 kJ mol^{-1}. Considering all the aforementioned criteria, the adsorption energies of CO, CO_2 and O_2 are summarized in Figure 34. It appears that Fe-$PtSe_2$ is the best candidate to catalyze CO oxidation and hence investigated afterward.

Table 11: Calculated binding energies and geometrical parameters for TM-$PtSe_2$.[a]

TM	Sc	Ti	V	Cr	Mn	Fe	Co	Ni	Cu	Zn
E_b	−390	−337	−310	−461	−523	−258	−107	−46	9	−25
r(TM-Pt)	2.49	2.40	2.37	2.51	2.46	2.43	2.43	2.43	2.50	2.50
d	−0.19	−0.34	−0.41	−0.11	−0.17	−0.24	−0.21	−0.16	−0.08	−0.16

[a] Energies in kJ mol^{-1}. Distances between Pt and TM atoms r(TM-Pt) and distances between TM atom and the Se layer (d, negative sign indicates the embedded TM atom is below the Se plane) are reported in Å.

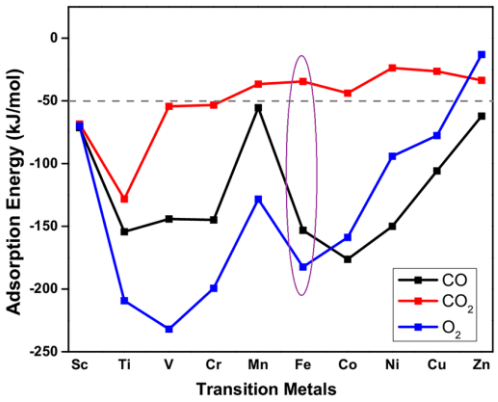

Figure 34: Adsorption energies of CO, O_2 and CO_2 molecules on TM-$PtSe_2$ (TM=Sc-Zn).

3.3.2.2 Geometry, electronic structure and stability of Fe-$PtSe_2$

The Fe-Pt bond length of 2.43 Å (Table 11) is shorter than the Pt-Se bond 2.53 Å, thus the embedded Fe atom is slightly below the Se plane. The optimized structure of Fe-$PtSe_2$ with charge density difference (between $PtSe_2$ with Se vacancy and Fe-$PtSe_2$) and spin densities are shown in Figure 35a and 35b, respectively. The majority of spin densities is located on the Fe atom, which is also in good agreement with the spin-polarized DOS of Fe-$PtSe_2$ as shown in Fig. 3.34c. In addition, the band around the Fermi level is mainly contributed from Fe-3d and Pt-5d orbitals.

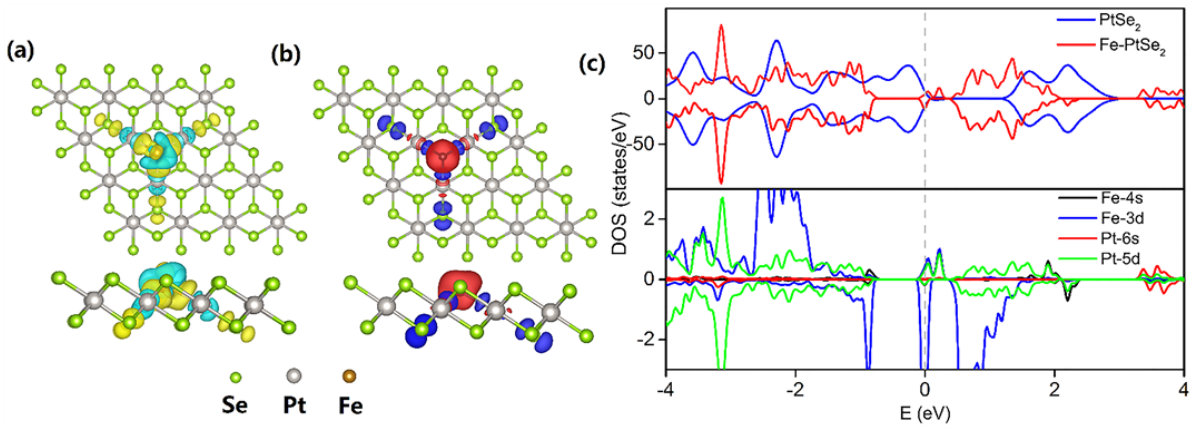

Figure 35: A top and a side view for Fe-$PtSe_2$ monolayer with density difference (a) and spin densities (b). The TDOS and LDOS projected on Fe-4s, Fe-3d, Pt-6s and Pt-5d are shown in (c).

The stability of the embedded Fe atom at the Se vacancy has been compared with respect to its relocation on the Se surface nearby. Fe atom is assumed to migrate to either the center of the Se-Pt-Se hexagonal ring (Figure 36, FS1) or to the top of Pt (Fig. 36, FS2). However the

Fe adsorptions on such positions (with adsorption energies −140 and −91 kJ mol^{-1}, respectively) are both significantly weaker than the original position (with adsorption energy −258 kJ mol^{-1}). In addition, the barriers for the Fe atom migrations are 230 and 224 kJ mol^{-1}, respectively. Thus Fe atom both thermodynamically and kinetically favors the Se vacancy rather than the Se surface and avoids to form iron cluster on the surface.

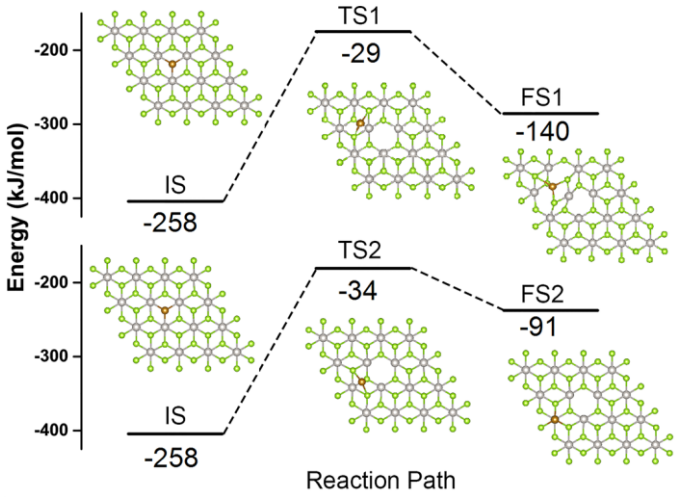

Figure 36: Reaction paths of Fe migration from the Se vacancy to the center of neighboring hexagonal ring (upper part) and to the top of the Pt atom (lower part).

3.3.2.3 Adsorption of O_2 and CO

The energetically most favored side-on configuration of O_2 adsorption on Fe-$PtSe_2$ is associated with the adsorption energy of −156 kJ mol^{-1}(PBE level) and −182 kJ mol^{-1}(PBE+D3 level). As shown in Figure 37a, the bond lengths of Fe-O1 and Fe-O2 are 1.80 Å and 1.86 Å, respectively. Meanwhile, the O-O bond length changes from 1.21 Å (gas phase molecule) to 1.39 Å (adsorbed). The electron transfer from HOMO (localized Fe-3d) to LUMO O-2π^* orbitals (0.77 |e| by Bader charge analysis, also shown in Figure 37b.) explains the significant weakening of the O-O bond. The magnetic moment of embedded Fe also reduced significantly upon O_2 adsorption. All these results indicate that O_2 molecule is effectively activated by embedded Fe atom.

In the case of CO adsorption, a C end-on configuration is most stable as shown in Figure 37c with adsorption energy of −125 kJ mol^{-1}(PBE level) and −153 kJ mol^{-1}(PBE+D3 level). The Fe-C bond length is 1.71 Å, while the C-O bond length only stretches from 1.14 Å to 1.17 Å upon adsorption, indicating merely a moderate activation of CO. The charge transfer from the substrate to CO (0.40 |e|) accumulated on the Fe-C bond as shown in Figure 37d.

The changes in geometry of the Fe/$PtSe_2$ (Pt-Fe and Se-Fe distances) upon the adsorption of CO and O_2 and during the process of the reaction are shown in Table 12. Note that two values are reported due to the symmetry lowering upon O_2 adsorption, as well as for some intermediate structures.

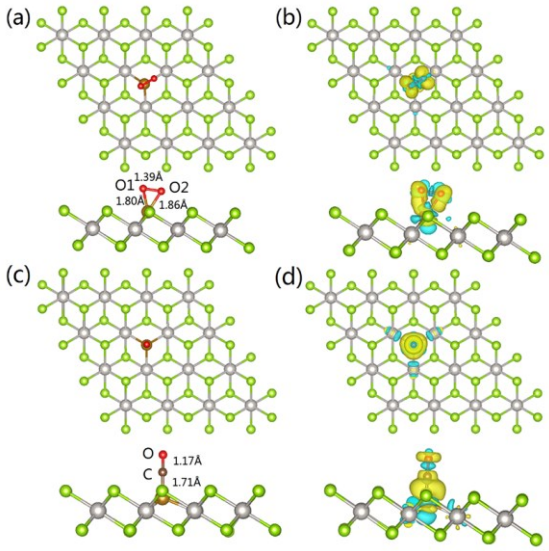

Figure 37: Adsorption configurations of O_2 (a) and CO (c) molecules, and charge density differences upon O_2 (b) and CO (d) adsorption.

Table 12: Structural parameters of Fe-$PtSe_2$ and reaction intermediates for both ER and LH reaction paths.[a]

Distance		$d_{(O1-O2)}$	$d_{(C-O1)}$	$d_{(C-O2)}$	$d_{(C-Fe)}$	$d_{(Pt-Fe)}$	$d_{(Se-Fe)}$
Fe-$PtSe_2$		–	–	–	–	2.43	3.21
O_2 ads.		1.39	–	–	–	2.47, 2.63	3.30, 3.43
CO ads.		–	–	–	1.71	2.37	3.06
ER	IS	1.39	3.50	3.54	5.14	2.46, 2.63	3.30, 3.43
	TS	1.40	1.74	2.65	4.29	2.47	3.29
	MS	3.13	1.18	2.88	4.43	2.41	3.16
	FS	5.10	1.18	4.96	6.50	2.42	3.17
LH	IS	1.39	3.50	3.54	5.14	2.46, 2.63	3.30, 3.43
	TS1	1.38	2.63	2.58	2.32	2.54, 2.75	3.40, 3.58
	MS1	1.34	2.67	2.68	1.92	2.62	3.47
	TS2	1.43	1.82	2.43	1.98	2.50, /2.57	3.26, 3.36
	MS2	1.51	1.35	2.17	2.05	2.48	3.28
	TS3	1.67	1.32	2.19	2.07	2.49, 2.57	3.25, 3.37
	MS3	3.13	1.18	2.88	4.43	2.41	3.16
	FS	5.10	1.18	4.96	6.50	2.42	3.17
ER O/Fe-$PtSe_2$	IS	–	–	3.08	4.66	2.42	3.17
	TS	–	–	1.71	3.39	2.44	3.23
	FS	–	–	1.18	3.41	2.47	3.27

[a] All distances reported in Å.

3.3.2.4 Reaction paths of CO oxidation

Eley-Rideal (ER) and Langmuir-Hinshelwood (LH) paths [139, 140] which are well known for CO oxidation process were both investigated. PBE is expected to underestimate the barriers, thus, all barriers reported were based on single point energy calculations with hybrid PBE0 functional for the structures optimized at PBE level.

As shown above, O_2 strongly adsorbs on the Fe site. Thus, the complex of CO molecule weakly adsorbs on O_2/Fe-$PtSe_2$ system is taken as the initial structure (IS in Figure 38) and its energy is taken as the reference for both reaction paths.

The ER path (Figure 38, red) consists of only one elementary step. The transition state (TS) structure (barrier of 53 kJ mol^{-1}) leads to the complex of a CO_2 molecule weakly interacting with O/Fe-$PtSe_2$ (MS). The desorption process of CO_2 molecule to the gas phase is endothermic by 6 kJ mol^{-1} (without dispersion).

The LH path (Figure 38, blue) consists of three elementary steps. The first step, the formation of co-adsorption complex of O_2 and CO molecules (MS1) is exothermic (−29 kJ mol^{-1}) with a barrier (TS1) of 10 kJ mol^{-1}. The second step is the formation of a peroxo-type intermediate (MS2) which has a barrier (TS2) of 72 kJ mol^{-1}; it is the rate-determining step of LH path. The third step is the decomposition of the peroxo-type intermediate to form CO_2 (MS3) which is strongly exothermic (−325 kJ mol^{-1}) with a barrier (TS3) of 40 kJ mol^{-1}. Note that intermediates MS3 (LH path) and MS (ER path) are identical, therefore, desorption energies of formed CO_2 are identical.

CO oxidation by O_2 leads to an O adatom on Fe-$PtSe_2$ (denoted as O/Fe-$PtSe_2$). Thus the catalytic cycle is completed by CO oxidation by O/Fe-$PtSe_2$ (Figure 39). The complex of CO interact with O/Fe-$PtSe_2$ is taken as reference (IS). This reaction contains only one step that is the formation of CO_2 molecule (−237 kJ mol^{-1}) with a barrier of 21 kJ mol^{-1}. The easy desorption process of CO_2 molecule is expected because the desorption energy is equivalent to the adsorption energy of CO_2 (less than 50 kJ mol^{-1} including dispersion). Thus the barrier of CO oxidation by O/Fe-$PtSe_2$ is significantly lower than that by O_2.

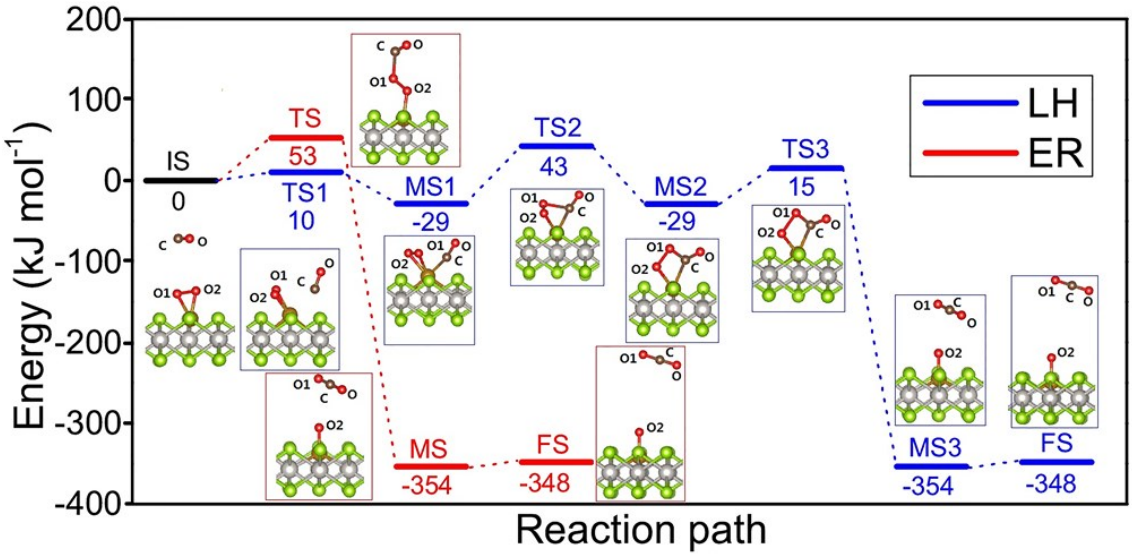

Figure 38: The reaction paths of CO catalytic oxidation by O_2 over Fe-$PtSe_2$ via the LH (blue) and ER (red) paths. Note the FS of LH and ER paths are actually the same structure.

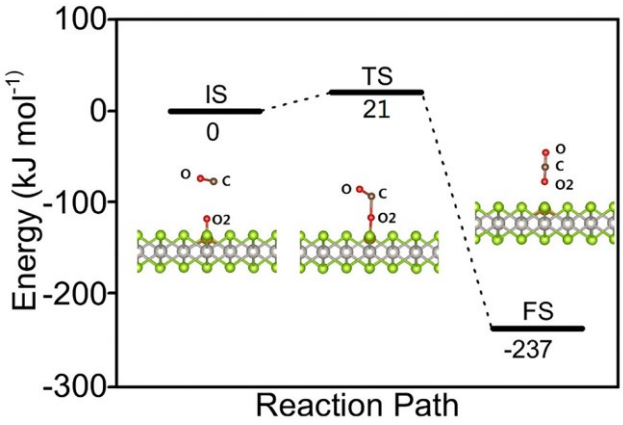

Figure 39: Reaction path of CO oxidation by O/Fe-$PtSe_2$.

Since the barriers of both paths for CO oxidation by the adsorbed O_2 molecule is higher than the barrier of CO oxidation by O/Fe-$PtSe_2$, the former process determines the overall reaction rate. The ER path contains only one step ($\Delta E^{\neq}$ = 53 kJ mol^{-1}), while the LH path proceeds via three steps with barriers $\Delta E^{\neq}$ = 10 (TS1), 72 (TS2), and 44 (TS3) kJ mol^{-1}, respectively. To further explore which path dominates, we calculated the reaction rate constants for both paths as shown below:

LH: $$(CO)_g + (O_2)_{ads} \underset{k_{-1}}{\overset{k_1}{\rightleftharpoons}} MS1 \underset{k_{-2}}{\overset{k_2}{\rightleftharpoons}} MS2 \xrightarrow{k_3} (CO_2)_g + (O)_{ads} \quad (3.4)$$

ER: $$(CO)_g + (O_2)_{ads} \xrightarrow{k_{ER}} (CO_2)_g + (O)_{ads} \quad (3.5)$$

where the reactants, CO in the gas phase and O_2 adsorbed on Fe atom are denoted as $(CO)_g$ and $(O_2)_{ads}$ respectively; $(O)_{ads}$ indicates the O adatom on Fe; other notations (MS1 and MS2) are corresponding intermediates defined in Figure 38. The rate constants are calculated for each step with corresponding barrier.

According to Eq. (3.4) and quasi stationary approximation, the CO_2 concentration resulted from LH path can be calculated as:

$$[CO_2]_{LH} = \frac{k_1}{k_{-1}} \frac{k_2 k_3}{k_{-2} + k_3} p_{CO} [(O_2)_{ads}] = k_{LH} p_{CO} [(O_2)_{ads}] \quad (3.6)$$

where k_{LH} stands for the overall rate constant for LH path; p_{CO} and $[(O_2)_{ads}]$ are the partial pressure of CO gas and concentration of adsorbed O_2 molecules, respectively. Similarly, according to Eq. (3.5), the CO_2 concentration resulted from ER path can also be calculated as:

$$[CO_2]_{ER} = k_{ER} p_{CO} [(O_2)_{ads}] \quad (3.7)$$

where k_{ER} remains to be the rate constant of the elementary step. All the rate constants are summarized in Table 13. At T=300 K, the ratio k_{ER}/k_{LH} is 1.1, indicating both paths are

possible to proceed. In addition, k_{ER}/k_{LH} ratios calculated at 250K and 350K are 0.5 and 1.9, respectively. Thus at lower temperature LH path is favored, while ER path prevails at higher temperature.

Table 13: Rate constants for ER and LH mechanisms calculated at various temperatures.

Rate constants(s^{-1})	T=250K	T=300K	T=350K
k_{ER}	1.9×10^{01}	4.3×10^{02}	4.1×10^{03}
k_{-ER}	3.1×10^{-71}	1.8×10^{-57}	1.2×10^{-47}
k_1	1.6×10^{09}	1.4×10^{09}	1.3×10^{09}
k_{-1}	5.8×10^{05}	1.5×10^{07}	1.4×10^{08}
k_2	1.4×10^{-02}	4.2×10^{00}	2.5×10^{02}
k_{-2}	3.9×10^{-02}	9.4×10^{00}	4.9×10^{02}
k_3	4.6×10^{03}	2.3×10^{05}	3.8×10^{06}
k_{-3}	7.4×10^{-66}	4.1×10^{-53}	5.2×10^{-44}
k_{LH}	4.0×10^{01}	3.9×10^{02}	2.3×10^{03}

Our results show that the Fe-$PtSe_2$ is able to catalyze CO oxidation under mild conditions.[141] The calculated energy barriers are comparable to other 2D SAC systems (as summarized in Table 14). In addition, results summarized in Table 14 are DFT calculations using either local or semi-local functionals. However, according to our results, the results calculated by semi-local and hybrid functionals could be qualitatively different: the change of functional from PBE to PBE0 increase the barrier of rate-determining step via LH path from 45 to 72 kJ mol^{-1} while decrease the barrier via ER path from 63 to 53 kJ mol^{-1}. In addition, the identification of the dominating reaction path based only on barriers is not sufficient: although the ER barrier is 20 kJ mol^{-1} lower that of LH path, calculated overall rate constants for both paths are comparable. However, no rate constants for SAC-type catalysts summarized in Table 14 were reported, thus it is difficult to compare their catalytic activities without knowledge of rate constants. The lowest energy barriers of CO oxidation for similar systems reported so far are 30 (Au-graphene)[142] and 45 (Au-BN)[143] kJ mol^{-1} at PBE level, respectively, which are close to our results (at PBE level) for Fe-$PtSe_2$. Note the barriers we report are lower than those reported for Pt(111).[144]

We also investigated the influence of dispersion on the stability of reaction intermediates with D3 correction. We found that the dispersion corrections remain constant almost for all intermediates via both paths, thus the influence of dispersion on stability of individual intermediates is small.

Table 14: The summary of energy barriers ($\Delta E^{\neq}$)[a] of CO oxidation catalyzed by different metal-embedded 2D materials.

System	Mechanism	$\Delta E^{\neq}$	Methods	Reference
Au-graphene	LH	30	PBE+DND	[142]
Fe-graphene	ER	56	PW91+DND	[140]
Cu-graphene	LH	52	PWC+DNP	[145]
Fe-MoS_2	LH	49	PBE+PAW, 450eV	[42]
CoPc	LH	63	PWC+DNP	[138]
Au-BN	ER	45	PBE+PAW,400eV	[143]
Co- BN	ER	50	PBE+PAW,400eV	[146]
Fe- $PtSe_2$	LH	45	PBE+PAW,500eV	Present work
	LH	72	PBE0+PAW,500eV	Present work
	ER	63	PBE+PAW,500eV	Present work
	ER	53	PBE0+PAW,500eV	Present work

[a] Energies in kJ mol^{-1}.

3.3.3 Summary

The oxygen incorporated, interlayer expanded MoS_2 was investigated computationally in collaboration with experimental groups. First we constructed two models for pristine MoS_2 with 2H phase and interlayer expanded, oxygen incorporated MoS_2 with 1T phase, based on experimental XRD measurements. Then we performed first-principle calculations for the lithium ion intercalation in MoS_2-2H and O-MoS_2-1T and found that the intercalation process is more exothermic in interlayer expanded O-MoS_2-1T. In addition, OCV in O-MoS_2-1T is also higher. According to OCV calculations, the specific capacity of O-MoS_2-1T could be larger than 334 mAh g^{-1} regardless the existence of interlayer molybdenum oxide species. Our calculations confirm that interlayer expanded MoS_2 has great potential for LIB applications, qualitatively explains the larger experimental specific capacity (220 mAh g^{-1}) of interlayer expanded MoS_2 than pristine MoS_2 (158 mAh g^{-1}). Next considering the pillaring

effects of molybdenum oxide species, we found that the oxygen substitution on the surface of MoS_2 has only very small effect on interlayer distance. For 1T MoS_2 structures incorporated by molybdenum oxide species, the interlayer distances of all investigated structures are enlarged significantly, while the incorporations of $Mo(OH)_4$ and $MoO(OH)_3$ lead to reasonable agreements with experimental results.

Computational screening of 3d transition metal (Sc-Zn) embedded in $PtSe_2$ monolayers was carried out to seek the potential CO oxidation catalysts. According to the criteria stated for similar purpose previously,[138]**Error! Bookmark not defined.** we chose Fe-$PtSe_2$ as the best andidate and further investigated its electronic structure, structural stability and reaction paths. We found Fe-$PtSe_2$ to be stable enough to avoid an iron-cluster formation. We considered both LH and ER path for CO oxidation by O_2 adsorbed on Fe-$PtSe_2$. Although, for the rate-determining steps, the barrier of LH path (71 kJ mol^{-1}) is higher than that for ER path (53 kJ mol^{-1}), our kinetics analysis shows the overall rate constant for both paths are comparable at 300 K. In addition, LH path prevails at a lower temperature. To complete the catalytic cycle, we also investigated CO oxidation by the O adatom on Fe-$PtSe_2$ where a single step reaction proceeds via ER path with a barrier of only 21 kJ mol^{-1}. Our results thus suggest that Fe-$PtSe_2$ could be an efficient CO oxidation catalyst.

3.4 Transition metal carbides and transition metal trihalides

Although the exciting physical and chemical properties of 2D layered materials render their potential in new generation of electronic and spintronic devices,[53] the practical applications of a majority of 2D materials in spintronics are limited due to the absence of intrinsic magnetism. The magnetic properties can be introduced into 2D layered materials by approaches such as doping, defects and functionalization, the experimental preparation of such materials with an highly ordered spin structure, as well as spin-polarization at room temperature is still a challenge,[54] due to the extra complexities such as the difficulty to obtain uniform distributions as well as to avoid clustering of dopants.[55] Thus, 2D materials with intrinsic magnetism associated with high Curie/ Néel temperature are desirable. In this section, transition metal carbides (MXenes) and transition metal trihalides (TMTs) have been investigated for their magnetic properties. Results present in this section have been published in *J. Mater. Chem. C,* 2016, 4, 6500, *J. Mater. Chem. C,* 2016, 4, 11143, *J. Mater. Chem. C,*

2016, 4, 2518 and *Nanoscale*, 2017, 9, 2246, where more details about the topic can be found. These papers can be found in Attachment No. 9-12.

3.4.1 Cr-based MXenes: spin-polarized antiferromagnetic semiconductors

Novel materials with high-spin polarization and magnetic order at room temperature are highly desirable to develop new generation of spintronic devices. Spin-polarized, ferromagnetic materials are suitable for spintronics. However, the generation of spin-polarized current is usually prevented by the magnetic domains, stray fields and low Curie temperature. On the other hand, spin-polarized, antiferromagnetic materials which have zero magnetism, are usually associated with high Néel temperature. In this section, the asymmetrically functionalized MXenes (two-dimensional transition metal carbides) are proposed, using first-principle calculations, to be a new class of spin-polarized semiconductors with fully compensated antiferromagnetism associated with high Néel temperature.

The investigated MXenes have the formula Cr_2CXX', where X and X'=H, OH, F, Cl and Br. The structure and FM states, Néel states and zigzag states are shown Figure 40. Considering the nearest (J_1)- and next-nearest (J_2)-exchange coupling parameters calculated by mapping the DFT energies to the spin Hamiltonian, the Néel temperatures T_N were calculated by Monte Carlo simulations. Rather high Néel temperatures were found for Cr_2CFCl, Cr_2CHBr, Cr_2CClBr, Cr_2CFBr, Cr_2CBrOH, Cr_2CHCl, Cr_2CHF, Cr_2CClOH, Cr_2CFOH and Cr_2CHOH (395, 320, 385, 310, 300, 430, 380, 375, 390 and 270 K, respectively). Their high T_N indicate their potential for spintronic applications at room temperature.

In addition to high Néel temperature, these materials also show bipolar antiferromagnetic semiconductor (BAFMS) characters. More details of BAFMS as well as the band gap tailoring can be found in the attached papers.

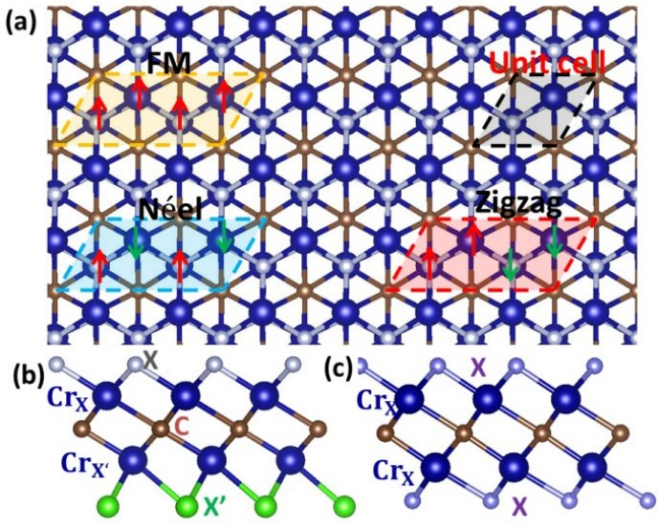

Figure 40: Atomistic structure of Cr_2CXX' and the magnetic states

3.4.2 Mn-based MXenes: ferromagnetic materials at room temperature

As we shown in previous section, MXenes are promising materials for spintronic applications. However, the chemical functionalization of the surfaces of MXenes usually leads to the completely compensated antiferromagnetic (AFM) states. To broaden the application of MXenes on spintronics, in this section, we investigated the electronic and magnetic properties of MXenes with the formula Mn_2CT_2 (T=F, Cl, OH, O and H) using DFT calculations. This investigation is based on both theoretically and experimentally confirmation of existence of Mn_2GaC MAX phase with a ferromagnetic order, because Mn_2GaC is possible to be converted to 2D Mn_2CT_2. Our results show that the ferromagnetism of Mn_2CT_2 is conserved for surface functional groups with −1 charge (F, Cl and OH).

The atomistic structure and magnetic states of investigated Mn_2CT_2 MXenes are shown in Figure 41. For Mn_2CT_2 (T=F, Cl and OH), where the surface functional group has a formal charge of −1, the magnetic ground states are ferromagnetic associated with half-metallicity. The Curie temperatures calculated with Monte-Carlo simulations are 520, 460 and 380 K for Mn_2CF_2, $Mn_2C(OH)_2$ and Mn_2CCl_2, respectively, which are higher than room temperature. For Mn_2CT_2 (T=O and H) where the formal charge of surface functional group are −2 and +1, respectively, the net magnetization drops and the half-metallicity disappears. Mn_2CO_2 is an AFM semiconductor with Néel temperature of 110K while Mn_2CH_2 is an AFM metal with Néel temperature of 120K.

Our results show that Mn_2CT_2 materials have tunable magnetic order (ranging from FM half metal, AFM metal and AFM semiconductor), as well as high Curie temperature. More details can be found in the attached paper.

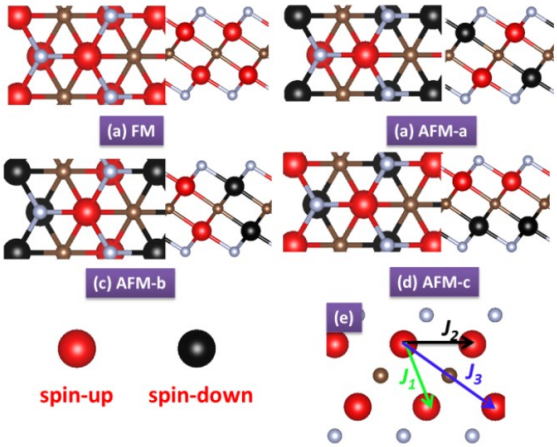

Figure 41: Atomistic structure of Mn_2CT_2 and the magnetic states

3.4.3 Vanadium trihalide: Dirac half metal

The Dirac half-metals, characterized by a semiconducting/insulating spin channel and a Dirac cone in the other spin channel, have attracted increasing interest, due to their potential in spintronic applications. In this section, we report the DFT+*U* investigations on 2D vanadium trihalides (VCl_3 and VI_3). They are predicted to have intrinsic ferromagnetism and half-metallicity. In addition, the Dirac points around Fermi levels are found only in one spin channel in VCl_3 and VI_3. Thus our results predict new members of 2D Dirac materials which have great potential towards spintronic applications.

VCl_3 and VI_3 monolayers can be exfoliated from their bulk forms which belong to R3 space group. The atomistic structures as well as the possible magnetic states (including the collinear FM, Néel, zigzag and stripy states) are shown Figure 42. The magnetic ground states are predicted to be ferromagnetic for both of them. Thus the Curie temperature is evaluated with Monte-Carlo simulations, and it is 80K and 98 K for VCl_3 and VI_3, respectively. Although the Curie temperature is lower than room temperature, it can be increased upon carrier doping. In addition, the carrier doping can also shift the Dirac states to exactly the Fermi level.

Our results show that 2D VCl_3 and VI_3 are new materials showing the Dirac half-metallicity, with promising spintronic applications. Their magnetic properties can be further tuned via carrier doping. More details can be found in the attached paper.

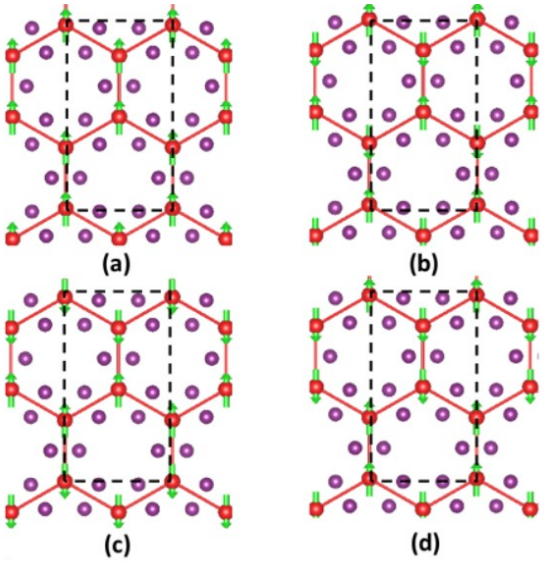

Figure 42: Atomistic structure of VCl_3/VI_3 and the possible magnetic states; red balls indicate V atoms and purple balls indicate Cl/I atoms

3.4.4 Nickel trichloride: Chern-insulator at near room temperature

Chern insulators are essential for applications of the quantum anomalous Hall (QAH) effect. QAH has been experimentally observed only at very low temperature (<30mK), which prevent its practical applications. In this section, we investigated nickel trichloride ($NiCl_3$) monolayers with DFT calculations. We found that $NiCl_3$ monolayer has ferromagnetism at high temperature, a large non-trivial band gap about 24 meV as well as high Curie temperature. In addition, the electron mobility within $NiCl_3$ is also predicted to be very high. Our results show that $NiCl_3$ monolayer is promising for the applications of QAH effect at near room-temperature as well as for the spintronic applications.

The structure of $NiCl_3$ is shown in Figure 43, as well as the dependence of total energy on lattice parameter. *Ab initio* molecular dynamics show that the ferromagnetic state is robust at room temperature. The Curie temperature evaluated by Monte-Carlo simulation is 400K, much higher than the reported experimental temperature of QAH (30mK). Moreover, $NiCl_3$ is predicted to show QAH effect at 280 K with HSE06+SOC calculated large non-trivial band gap of about 24 meV. The existence of edge states of $NiCl_3$ monolayer is also confirmed. In addition, the Fermi velocity calculated for $NiCl_3$ monolayer is the same order of graphene.

All these results show $NiCl_3$ monolayer is promising for QAH effect application at near room temperature. More details about the computations can be found in the attached paper.

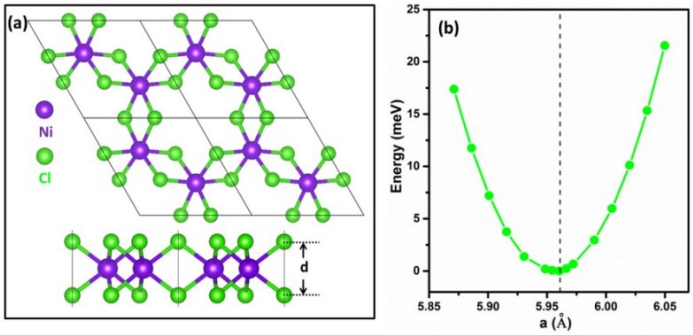

Figure 43: (a) Atomistic structure of $NiCl_3$ and (b) the dependence of total energy on lattice parameter

3.4.5 Summary

We have computationally predicted exciting electronic and magnetic properties for a number of new 2D magnetic materials including Cr- and Mn-based MXenes and TMTs (VCl_3, VI_3 and $NiCl_3$). These materials are promising for practical spintronic applications because their Curie/Néel temperature obtained from Monte Carlo simulations are around room temperature. The results reported here not only extend the family 2D magnetic materials for spintronics, but also enrich the spectrum of magnetic materials in general.

3.5 Layered double hydroxide: the structure of fougèrite and mössbauerite

Layered double hydroxides (LDH) are widely studied for their potential in numerous applications, including adsorption, photocatalysis and electrocatalysis. A remarkable feature of the LDHs is the absence of crosslinking between the adjacent cationic layers which allows the expansion and compression of the interlayer space to accommodate various exchangeable A^{n-}. The understanding of LDH structures is essential to advance their researches. The fougèrite group minerals are unique subgroup of the hydrotalcites in which the divalent and trivalent cations are of the same element (Fe)[67] and they are known in the form of naturally occurring green rust phases. Despite considerable efforts,[67] the structure of mössbauerite is not fully understood. Thus the structure and surface carbonate grafting of fougèrite and mössbauerite were investigated by a combination of experimental and computational methods.

3.2.1 Specific details for LDH

Test calculations carried out for mössbauerite with the 2T unit cells (2 layers per cell) revealed that ferromagnetic (FM) and antiferromagnetic (AFM) states have very similar energies (the differences are always smaller than 10 kJ mol^{-1}, and mostly smaller than 5kJ mol^{-1}). Thus, FM coupling was adopted for all calculations. Consequently, calculations were performed with the unit cell containing a single layer. The $3R_1$ model was used for fougèrite and it was reduced to 1/3 by an offset vector, considering the symmetry. There are a large number of possible structures of mössbauerite, $3T_7$ ($O_1O_2P_2$) [67]. Therefore, the 1T model was used; the corresponding O_1 geometry represents reasonably well the structure of mössbauerite and it is suitable for atomistic understanding of the interlayer space. The $\sqrt{3}\times 2\sqrt{3}$ supercell is adopted to accommodate the carbonate anion (CO_3^{2-}). Three water molecules were included in the interlayer space within both models giving following stoichiometries: fougèrite $Fe_4^{2+}Fe_2^{3+}(OH)_{12}[CO_3]\cdot 3H_2O$) and mössbauerite $Fe_6^{3+}O_4(OH)_8[CO_3]\cdot 3H_2O$).[67] Thus, the total magnetic moments of fougèrite and mössbauerite were fixed at 26 and 30 μ_B per cell (6 Fe atoms in total, 4 Fe^{2+} and $2Fe^{3+}$ in fougèrite and 6 Fe^{3+} in mössbauerite). 4×3×2 k-point sampling[128] was used for all calculations.

TOPAS Academic V5 was used for structure solution. Applying the unit cell data from DFT+U calculations, 20 stacks of grafted and non-grafted mössbauerite layers each were created with randomized ***a***/***b*** ($\Delta \neq 1/3$) orientation to compensate for turbostratic disorder. The random stacking was simulated by varying the ratio of grafted to non-grafted layers. Since the amount of grafted and non-grafted layers is unclear at this point, the ratio was left open for refinement with a starting value of 1/1. To compensate the thermal expansion of the lattice parameters of the DFT+*U* calculated values, the unit cell parameter ***a*** and ***c*** were refined within an allowed range of 0.5 Å. Cell angles were allowed to vary within ± 3°. Also, the atomistic displacement parameters (beq) were set to 7 for hydrogen, 6 for carbon, 4 for iron and 6 for oxygen. The step size was set to 0.05. The input file was created based on the kaolinite.inp file by Ian Madsen.

3.5.2 The structure of fougèrite

The unit cell of $Fe_4^{II}Fe_2^{III}(OH)_{12}[CO_3]\cdot 3H_2O$ has been adopted for fougèrite. All surface oxygen atoms are saturated with hydrogens as shown in Figure 44. Due to a larger number of

geometrical and conformational degrees of freedom of molecules in the interlayer space, several low-lying energy minima were obtained and the relative energies (with respect to the most stable configuration obtained) and UC parameters of the five lowest energy structures of non-grafted (NG) and grafted (G) structures are summarize in Table 15. The top and side views of the most stable fougèrite structures (non-grafted and grafted denoted as NG_1 and G_1, respectively) and simulated and experimental PXRDs are shown in Figure 44.

Table 15: The relative energies (E_{rel}, in kJ mol^{-1}) and ***a*** and ***c*** vectors (in Å) of optimized fougèrite structures

Non-grafted			Grafted		
Structure	E_{rel}	***a/c***	Structure	E_{rel}	***a/c***
NG_1	0	3.20/7.43	G_1	19	3.21/7.19
NG_2	1	3.20/7.43	G_2	20	3.21/7.11
NG_3	1	3.20/7.44	G_3	28	3.20/7.12
NG_4	2	3.20/7.42	G_4	48	3.20/7.14
NG_5	3	3.20/7.43	G_5	54	3.23/7.19

Grafting leads to a sizable decrease of the lattice *c* vector while the *a* vector is not changed significantly (Table 15). Consequently, the calculated (*hkl*) peaks with $l \neq 0$ are different for grafted and non-grafted structures. The PXRD calculated for NG_1 non-grafted and G_1 grafted structures are shown in Fig. 43c together with experimental results. The pattern calculated for the non-grafted structure is in significantly better agreement with experimental data than the pattern obtained for grafted fougèrite. In addition, we found that the grafted structures are higher in energy that the non-grafted structures and that grafting of fougèrite cannot take place spontaneously. Based on the results presented in Figure 44 we conclude that no, or only limited, grafting takes place in fougèrite.

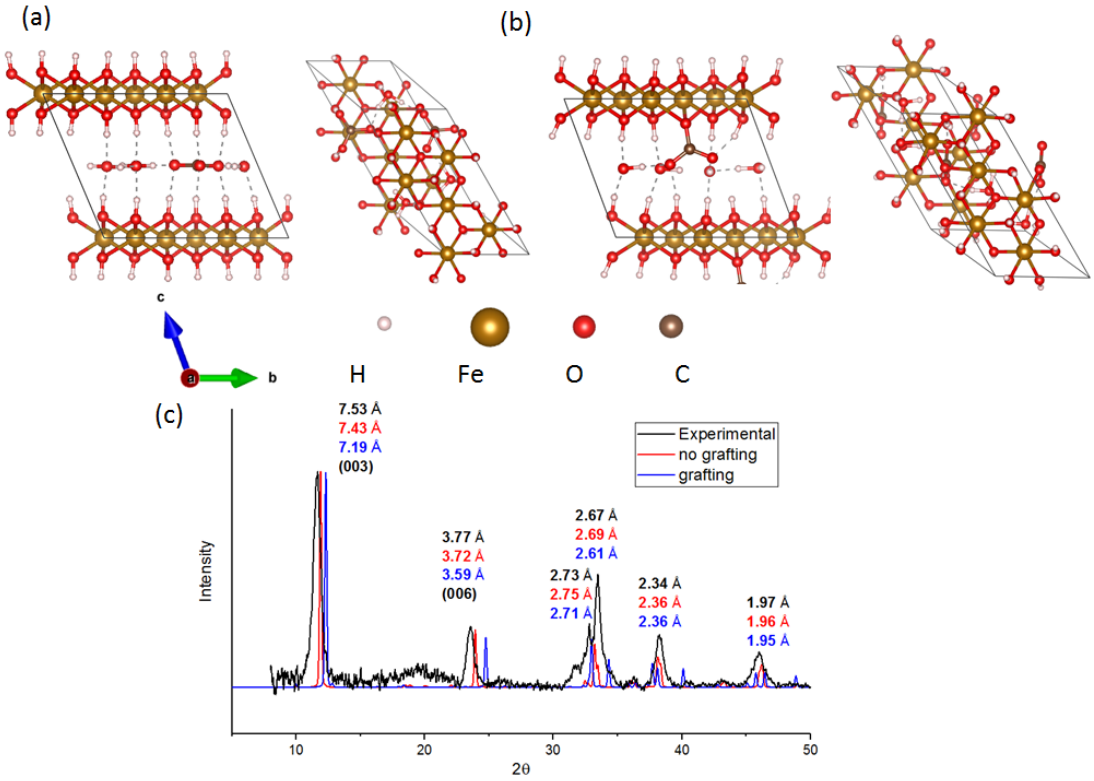

Figure 44: Side and top views of energy most stable structures of fougèrite without (a) and with (b) carbonate grafting (NG_1 and G_1, respectively); (c) simulated PXRD of fougèrite with and without carbonate grafting together with experimental PXRD of fougèrite.

3.5.3 The structure of mössbauerite

The unit cell of $Fe_6^{III}O_4(OH)_8[CO_3] \cdot 3H_2O$ has been adopted for mössbauerite. Each layer of mössbauerite has 8 hydrogen atoms distributed between the upper and lower surfaces. This brings additional complexity (compared with fougèrite) for the description of the mössbauerite interlayer space. Possible 8H configurations include: the (6H/2H) configuration with fully hydrogenated upper surface and only two H atoms on the lower surface; (5H/3H); and (4H/4H). In addition, protons can be also exchanged with carbonate and water in the interlayer space. Geometries of all possible configurations were optimized starting from various initial structures obtained from AIMD simulations. The structures obtained from subsequent geometry optimization were sorted according to their relative energies and the five most stable structures obtained for each hydrogen distribution are reported in Table 16 (with respect to the most stable structure obtained). Significantly larger differences in energies of individual structures were found for mössbauerite than reported above for

fougèrite. The (5H/3H) configuration NG_1 is found to be at least 32 kJ mol^{-1} more stable than any of the (6H/2H) and (4H/4H) configurations.

Table 16: The relative energies (E_{rel}, in kJ mol^{-1}) and ***a*** and ***c*** vectors (in Å) of mössbauerite layers with different numbers of hydrogen atoms on upper and lower surfaces

Structure	Non-grafted minima		Grafted minima	
	E_{rel}	***a/c***	E_{rel}	***a/c***
(5H/3H)	0	3.14/7.17	16	3.15/ 6.90
	17	3.15/7.11	17	3.15/6.85
	29	3.12/7.03	27	3.13/6.84
	45	3.09/7.08	27	3.15/6.83
(6H/2H)	37	3.08/7.16	—	—
	40	3.09/7.11	—	—
	48	3.07/7.17	—	—
	89	3.06/7.21	—	—
(4H/4H)	32	3.09/6.98	—	—
	33	3.08/7.03	—	—
	57	3.06/7.03	—	—
	63	3.12/7.28	—	—

Following the results for non-grafted mössbauerite, grafted structures were only searched for the (5H/3H) configurations, using the same strategy based on AIMD as for non-grafted structures, and results are also reported in Table 16.

The most stable non-grafted and grafted structures of mössbauerite are shown in Figure 45. Note that the carbonate anion (CO_3^{2-}) grafted on the lower surface is protonated by the hydrogen atom from the upper surface of adjacent layer, thus forming the HCO_3^- anion, and such structure is denoted (5H/2H). In analogy with fougèrite, a significantly smaller ***c*** vector is found for grafted than non-grafted structures, while the ***a*** vector remains unchanged. Contrary to the case of fougèrite, simulated PXRD patterns for both non-grafted and grafted structures poorly reproduce the experimental result (Figure 45c). While the ***c*** vector obtained for the non-grafted structure of mössbauerite (7.17 Å) is longer than the experimental value of 7.0 Å, the *c* vector obtained for the grafted structure (6.90 Å) is shorter. These results indicate that the experimental sample could be a mixture of grafted and non-grafted surfaces.

The relative stabilities presented in Table 16 indicate that grafting is not likely based on simple energetic considerations. However, the mössbauerite synthesis requires an excess of hydrogen peroxide to oxidize Fe^{II} to Fe^{III}, which may be the source of energy that is required for grafting. A detailed computational investigation presented below in Section 3.5.6 suggests that this is indeed the case. Therefore, we assume that the experimental sample of mössbauerite contains both non-grafted and grafted layers.

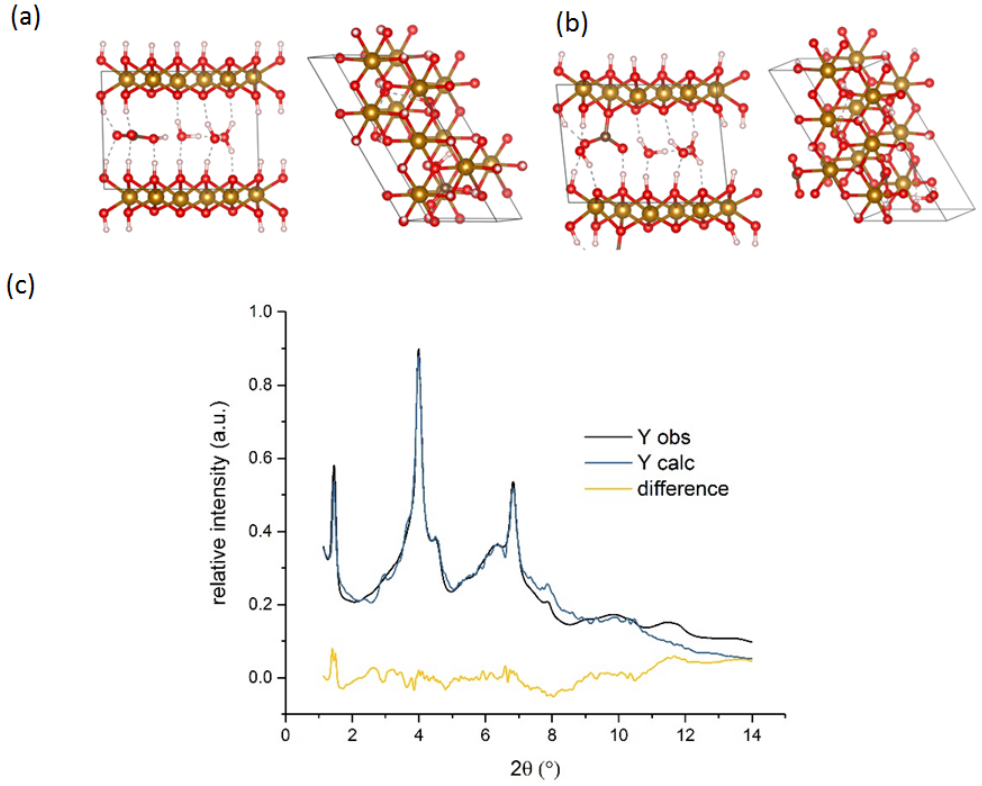

Figure 45: Side and top views of optimized mössbauerite structure without grafting (a) and with grafting (b). (c) Fit to Rietveld-generated pattern comprising stacks of grafted (63 %) and non-grafted (37%) mössbauerite. The stack size was set to 20 layers each.

The crystal structure solution for grafted and non-grafted mössbauerite was refined applying the cell parameters. Stacks of grafted and non-grafted layers were created with random ***a*** and ***b*** orientations. The refinement of the experimental diffractogram yielded an R_{wp} of 10.671 which can be considered satisfactory taking the highly disordered nature of the material into account. The refined cell parameters are shown in Table 17. The deviation from the DFT+*U* calculated distances and angles results mainly from the fact that DFT+U calculations do not consider thermal expansion or thermally induced flexibility of the lattice.

Table 17: refined lattice parameters of grafted and non-grafted mossbauerite structures, ***a***, ***b*** and ***c*** are in Å, α, β and γ are in degree

cell parameter	grafted$_{20}$	non-grafted$_{20}$
a	5.187972	5.609265
b	10.52681	11.17129
c	7.25695	7.21172
α	84.84656	82.43613
β	105.8354	99.95544
γ	121.1973	117.2881

The refined XRD is shown in Figure 45c. The calculated pattern takes the turbostratic disorder into account by shifting the stacks in ***a*** and ***b*** direction by $\Delta \neq 1/3$ and results in a broadening of the Bragg peaks in accordance with the experimental pattern. The first prominent reflex at $2\theta = 1.45°$ corresponds to the layer spacing of 7.0 Å. The difference plot shows, that the interstratification cannot be mimicked perfectly by using random sequences of two types of 20 layers each.

Additionally, the second Bragg centered peak at $2\theta = 3.99°$ cannot be indexed without doubt due to the amount of reflexes from both grafted and non-grafted stacks that account for the diffraction intensity. The most intense reflections in this region can be assigned to *hkl* = 120 and *hkl* = 200 according to the refinement. The reflex centered at $2\theta = 6.83°$ can be assigned mainly to *h*=3, *k*=0 and *h*=0, *k*=6 bands. If a random stacking is considered with an averaged d-spacing of 7.0 Å as experimentally observed, then the reflexes can be labeled *hkl* = 301 and 061.

3.5.4 Monodentate *vs.* bidentate carbonates

According to previous theoretical studies of the thermal decomposition of the MgAl-LDH, [147] the barrier for interconversion between monodentate and bidentate carbonate grafted structures is as high as 175 kJ mol^{-1}. Furthermore, the reaction energy is also higher than 150 kJ mol^{-1}. Both high barrier and reaction energy render this process unlikely to proceed under mild conditions; the phase-change in MgAl-LDH appears between 180 and 200 °C. [147]

In the case of mössbauerite, the reaction energy for transformation of monodentate to bidentate structure is 149 kJ mol^{-1} as shown in Figure 46. Such a high reaction energy

inhibits this reaction under the experimental conditions (up to ~50 °C), and agrees closely with previous theoretical work. Hence, bidentate carbonate grafting is much less likely than monodentate grafting. Only monodentate grafting is discussed in the following sections.

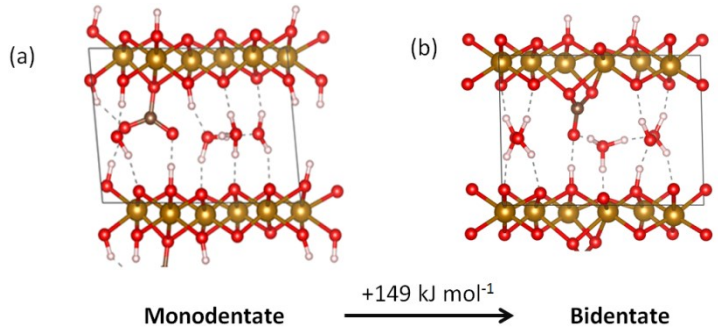

Figure 46: The monodentate (a) and bidentate (b) carbonate grafted mössbauerite.

3.5.5 Mechanism of carbonate grafting

In order to determine the relative stabilities of the grafted and non-grafted structures of fougèrite and mössbauerite, we calculated the relative energies of grafted structures with respect to non-grafted ones and found that the grafted structures are always less stable:

$$CO_3^{2-} + 2\,MOH \rightarrow MCO_3^{-} + MO^{-} + H_2O \qquad (3.8)$$

The reaction proceeds via abstraction of one of the surface H atoms and dissociation of the C-OH bond in carbonate; the energetic profiles for such a mechanism are shown in Figure 47a and 3.46b for fougèrite and mössbauerite, respectively. The structures of corresponding reactants, intermediates, transition states and products are shown in Figure 47c and 47d.

We first describe the mechanism of grafting for fougèrite. The transition state structure (**3** in Figure 47a) is reached when the carbonate anion abstracts a hydrogen from the layer and forms an HCO_3^- anion. The grafted carbonate is formed along with the hydroxyl group (OH^-) in the interlayer space (**5**). The barrier is as high as 190 kJ mol^{-1} and endothermic by 19 kJ mol^{-1}, which suggests that this process is both thermodynamically and kinetically unfavourable, and thus unlikely to occur under the experimental conditions (up to ~50 °C).

The reaction path is quite different in the case of mössbauerite. As mentioned above, the carbonate anion (CO_3^{2-}) exists in a protonated form, as HCO_3^-. From the most stable mössbauerite structure (**1'**), the hydrogen of HCO_3^- moves to another oxygen (**2'**), then the OH^- group from HCO_3^- attacks a hydrogen atom from the layer at the TS (**4'**) and forms grafted carbonate and one H_2O molecule (**6'**). The final product (**10'**) is formed with just a small barrier simply by the concerted series of rotations of the formed water molecule. The

overall barrier is 94 kJ mol^{-1}, which while is significantly lower than in fougèrite, is still too high for the reaction to take place under the experimental conditions. Although this reaction is also slightly less endothermic (17 kJ mol^{-1}) than on fougèrite (19 kJ mol^{-1}), there is still no clear driving force for the formation of carbonate-grafted mössbauerite.

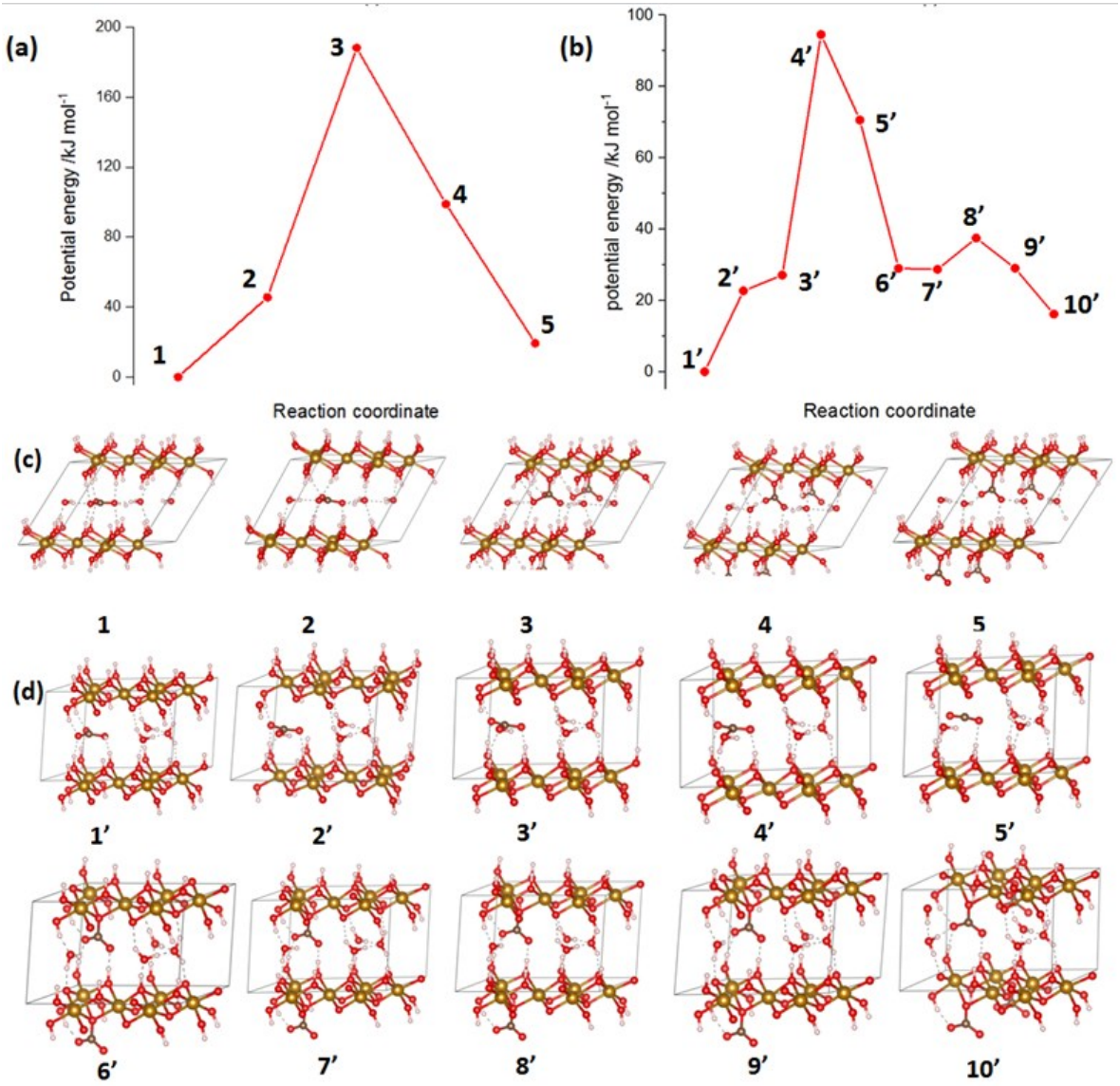

Figure 47: The potential energy profile of the carbonate grafting process for (a) fougèrite and (b) mössbauerite. The structures of corresponding reactants, intermediates, transition states and products are shown in (c) fougèrite (1–5) and (d) mössbauerite (1'–10').

3.5.6 The effect of H_2O_2

H_2O_2 is used for the oxidation of all Fe^{2+} in fougèrite to Fe^{3+} and to transform fougèrite to mössbauerite. In doing so, four H_2O molecules are formed from two H_2O_2:

$$Fe_4^{II}Fe_2^{III}(OH)_{12}[CO_3]\cdot nH_2(\text{fougèrite}) + 2H_2O_2 \rightarrow Fe_6^{III}O_4(OH)_8[CO_3]\cdot(n+4)H_2O\ (\text{mössbauerite})$$

It is difficult to consider the detailed reaction paths (H_2O_2 can act either as an oxidant or as a radical generator). However, the calculations of the reaction energy is straightforward (Figure 48). Assuming the stoichiometry of the above process, the reaction proceeds exothermically with a reaction energy of −154 kJ mol^{-1}, which is likely to be the driving force for carbonate grafting. Note that if the grafting (driven by H_2O_2) takes place, the resulting structure is protected by relatively high barriers against returning to non-grafted structures (Figure 48) and it is reasonable to assume that once the grafted surface is obtained it is kinetically stable.

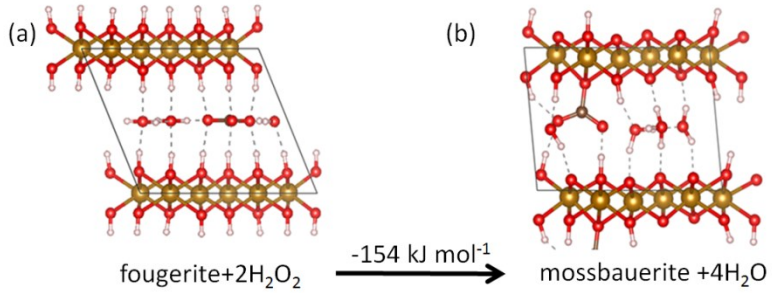

Figure 48: Transformation of fougèrite (a) to carbonate-grafted mössbauerite (b).

3.5.7 Summary

The results of the first systematic combined computational and experimental investigation of fougèrite and mössbauerite LDHs are presented. Density functional theory applied to periodic structures of the iron-containing LDHs allowed us to distinguish various structural details at the atomistic level. A critical comparison of these theoretical results with experimental data leads us to the following conclusions:

(i) The simulated PXRD spectra of non-grafted fougèrite agrees well with experimental data, while fougèrite grafted with carbonates shows poorer agreement, suggesting carbonate grafting is unlikely in fougèrite. This is in agreement with the calculated relative energies of grafted and non-grafted structures.

(ii) The simulated PXRD of neither grafted nor non-grafted mössbauerite agrees well with experimental data; to obtain agreement with experimental data one has to consider a

highly randomized structure of mössbauerite considering various arrangements of both grafted and non-grafted layers.

(iii) Grafting leads to the formation of monodentate carbonates while the formation of bidentate carbonates is unlikely.

(iv) The carbonate grafting process in fougèrite is endothermic (19 kJ mol^{-1}) and it exhibits a high barrier (190 kJ mol^{-1}).

(v) The carbonate grafting process in mössbauerite is also endothermic (17 kJ mol^{-1}) and the corresponding barrier is 94 kJ mol^{-1}. Considering the involvement of H_2O_2, which is utilized experimentally, the fougèrite to mössbauerite conversion becomes strongly exothermic (−154 kJ mol^{-1}). This is proposed to be the driving force for carbonate grafting in mössbauerite.

CHAPTER 4. Conclusions

The goal of the thesis was to increase our understanding of the properties and potential applications of 2D materials using first-principle calculations at the DFT level. Most systems investigated were researched in close collaboration with experimental groups. Six different types of 2D layered materials were investigated, in particular, covalent organic frameworks (COFs), silicene, transition metal dichalcogenides (TMDs), transition metal carbides (MXenes), transition metal trihalides (TMTs) and layered double hydroxides (LDHs), analyzing their structures, properties and applications in photocatalysis, catalysis and alkali-ion batteries. We believe that the results reported in this thesis are not only theoretically relevant but also have key practical implications. The major achievements of this research are briefly summarized below:

(1) ***Tuning the interlayer structures of 2D layered materials***

Unlike conventional 3D bulk materials, 2D layered materials are hold together mostly via the van der Waals interactions. Thus, although the intra-layer interactions are strong, typically covalent, inter-layer interactions are only weak and can be often overcome, leading to exfoliated 2D materials. Therefore, the inter-layer structures of 2D layered materials are often less ordered, regarding their interlayer arrangement, interlayer distance and interlayer atomistic structure. On one hand, structural details of these materials are difficult to obtain solely from experimental data; on the other hand, knowledge of these structures makes it possible to fine-tune layer arrangements for particular applications. In this context, atomistic insights based on DFT calculations are of great importance because the knowledge acquired from theoretical investigations can greatly help to advance the research of 2D materials.

In COFs, particularly in CTF-1, assessing the solvent effect is essential to analyze the relative stability of different interlayer arrangements. AA stacking is more stable in the absence of any solvent, as experimentally determined by ionothermal synthesis. AB stacking is stabilized by solvent (triflic acid) molecules, as experimentally determined by solution synthesis. The existence of triflic acid molecules in as-synthesized, AB-stacking CTF-1 crystals was confirmed by experimental observations (EDS). Thus, interlayer arrangements can be tuned using different synthetic methods.

In TMDs, particularly in MoS_2, interlayer distances can be tuned by incorporating foreign species such as alkali metals, oxygen, ammonia, carbon materials and organic molecules. The incorporation of various molybdenum oxide species in MoS_2 significantly enlarged the interlayer space. Calculations on inter-layer-expanded MoS_2 revealed that $Mo(OH)_4$ and $MoO(OH)_4$ are likely inter-layer species based on good agreements with experimental inter-layer distances.

In LDHs, particularly in fougèrite and mössbauerite, interlayer structures were investigated in detail considering the grafting of carbonate. Combined with experimental measurements, the carbonate-grafted structure was found in mössbauerite but not in fougèrite crystals. the result from our studies of reaction mechanisms and thermodynamic analyses showed that the carbonate grafting process is driven by the reaction of fougèrite with hydrogen peroxide producing mössbauerite. Moreover, th resulting grafted structure in mössbauerite is protected by a high kinetic barrier.

(2) ***Tuning the electronic properties of 2D layered materials***

2D layered materials have many advantages for practical applications such as photocatalysis, electronics and spintronics. However, their electronic properties often require tuning for specific applications. Doping and defect introduction are conventional approaches to tuning the electronic properties of materials. However, the concentrations and distributions of dopants and defects are difficult to experimentally control in 2D materials. Based on first-principle calculations, several strategies, other than doping and defect introduction, are proposed herein to effectively tune the electronic structures of 2D materials.

As exemplified for CTF-type COFs, their band gaps can be tuned with different nitrogen-to-carbon ratios and stacking patterns (AA eclipsed, serrated, inclined and AB staggered, helical). The adjustment of the nitrogen-to-carbon ratio affects both the structure of COF and the band gap; decreasing the nitrogen content directly increases the band gap, however, it also leads to structural changes (a lack of planarity due to the repulsion between hydrogen atoms on linkers and connectors) that secondarily increase the band gap. Similarly, different stacking patterns show different deviations from planarity, in addition to different interlayer distances; the shortening of interlayer distances also reduces the band gap for the bulk structures. Accordingly, band gaps and

band edge positions can also be modulated by specific nitrogen-to-carbon ratios and layer arrangements.

As exemplified in the studies of MXenes, another approach for tuning the electronic properties of 2D materials is the surface functionalization. Cr_2C can be converted from a ferromagnetic half-metal into a bipolar antiferromagnetic semiconductor simply by asymmetrical functionalization. Its band gap can be further tuned with suitable functional group pairs. Similarly, Mn_2C MXenes can be converted into materials with different characteristics such as ferromagnetic half-metals, antiferromagnetic metals or antiferromagnetic semiconductors, upon functionalization by surface groups with different electronegativities.

(3) ***Screening for potential applications of 2D layered materials for catalysis***

The high specific surface area of 2D materials accounts for their high potential as heterogeneous catalysts. Catalysts suitable for specific reactions are often found through trial-and-error. Yet, potential catalysts can be more easily identified and evaluated computationally from a pool of candidates with particular restrictions.

In photocatalytic water splitting, the band gap energy should range from 1.2 to 3.0 eV for enhanced sunlight absorbance in this region; using vacuum and pH=0 as reference conditions, VBM should be lower than the oxidation potential of O_2/H_2O (−5.67 eV), whereas CBM should be higher than the reduction potential of H^+/H_2 (−4.44 eV). Thus the band gaps and band edge positions of monolayers and bulk structures of CTF-type COFs with different interlayer arrangements were systematically investigated. Calculations for the general performance of water splitting catalysis indicate that CTF-1 and HPP are suitable photocatalysts only at pH=0 and 7, respectively, whereas TzF can be used at both pHs.

In CO oxidation reactions, (i) the overall barrier of CO oxidation under mild conditions should be lower than 96 kJ mol^{-1}; (ii) the adsorption of O_2 molecules on the catalyst should be stronger than that of CO molecules to avoid the catalyst poisoning and (iii) the adsorption energy of CO_2 should be weaker than –50 kJ mol^{-1}. After meeting these criteria, $PtSe_2$ monolayers embedded with 3*d* transition metal atoms were computationally screened, and Fe-$PtSe_2$ was identified as the best candidate for the catalysis of CO oxidation under mild conditions. Moreover, the subsequent study of

reaction mechanisms showed that Fe-$PtSe_2$ is able to catalyse CO oxidation via both Eley-Rideal and Langmuir-Hinshelwood reaction paths.

(4) ***Evaluating the application performance of 2D layered materials for alkali-ion batteries***

Alkali-ion batteries with high specific capacity, high rate capability and large cycle life are highly desired as new-generation energy storage devices. Advanced electrode materials are urgently needed to meet these needs. 2D materials with large surface areas associated with an abundance of active sites are promising candidates as electrode materials for alkali-ion batteries and thus have been extensively studied experimentally. Theoretical specific capacities are necessary to evaluate their performance. In close collaboration with experimental groups, we provide such evaluations of several 2D layered materials as alkali-ion batteries to gain in-depth insights for the development of advanced electrode materials.

In polyimide COF, 12 active sites for sodium ion adsorption were found in each individual layer, within monolayer and bilayer models. The theoretical specific capacity calculated for fully sodium-loaded polyimide COF was 403 mAh g^{-1}, which was in reasonable agreement with the corresponding experimental value (312 mAh g^{-1} at 0.1 A g^{-1}), considering the crystallinity of COFs (generally below 100%). For silicene, the calculated specific capacities of fully lithiated monolayers ($Li_{0.50}Si_{0.50}$) and bilayers ($Li_{0.43}Si_{0.57}$) were 957 and 722 mAh g^{-1}, respectively. The experimental capacity of few-layer silicene (721 mAh g^{-1}) was in good agreement with the theoretical capacity of bilayer silicene. For interlayer-expanded MoS_2, the calculated specific capacity was larger than 334 mAh g^{-1}. The experimental value of 220 mAh g^{-1} was smaller than 334 mAh g^{-1} due to the incorporation of interlayer molybdenum oxide species in the interlayer space. In addition, our theoretical capacity of pristine MoS_2 (167 mAh g^{-1}) was significantly smaller than the experimental value (220 mAh g^{-1}). Thus, our results justify the advantage of using interlayer-expanded MoS_2 as an electrode material.

Results reported herein were published in 12 research papers, which are included as attachments. The results reported in section 3.1.1, systematic investigation of CTF type COFs, and in section 3.5., layered-double hydroxides, have not been published yet, but the respective manuscripts are under preparation and will be submitted within next two months.

List of References

1. Z. Sun, A. Martinez and F. Wang, *Nat. Photonics*, 2016, **10**, 227.
2. R. Mas-Ballesté, C. Gómez-Navarro, J. Gómez-Herrero and F. Zamora, *Nanoscale*, 2011, **3**, 20-30.
3. K. S. Novoselov, A. Mishchenko, A. Carvalho and A. H. Castro Neto, *Science*, 2016, **353**, aac9439.
4. A. K. Singh, K. Mathew, H. L. Zhuang and R. G. Hennig, *The Journal of Physical Chemistry Letters*, 2015, **6**, 1087-1098.
5. K. Xu, L. Yin, Y. Huang, T. A. Shifa, J. Chu, F. Wang, R. Cheng, Z. Wang and J. He, *Nanoscale*, 2016, **8**, 16802-16818.
6. L. D. Landau and E. M. Lifshitz, *Statistical physics, Part I & II*, Pergamon Press, Oxford, 1980.
7. K. S. Novoselov, A. K. Geim, S. V. Morozov, D. Jiang, Y. Zhang, S. V. Dubonos, I. V. Grigorieva and A. A. Firsov, *Science*, 2004, **306**, 666.
8. A. K. Geim and K. S. Novoselov, in *Nanoscience and Technology*, Co-Published with Macmillan Publishers Ltd, UK, 2009, DOI: doi:10.1142/9789814287005_0002, 11-19.
9. M. J. Allen, V. C. Tung and R. B. Kaner, *Chem. Rev.*, 2010, **110**, 132-145.
10. K. S. Novoselov, V. I. Fal′ko, L. Colombo, P. R. Gellert, M. G. Schwab and K. Kim, *Nature*, 2012, **490**, 192.
11. X. Li, J. Yu, S. Wageh, A. A. Al-Ghamdi and J. Xie, *Small*, 2016, **12**, 6640-6696.
12. X. Jiang, P. Wang and J. Zhao, *J. Mater. Chem. A*, 2015, **3**, 7750-7758.
13. D. S. Su, J. Zhang, B. Frank, A. Thomas, X. Wang, J. Paraknowitsch and R. Schlögl, *ChemSusChem*, 2010, **3**, 169-180.
14. X. Zhang, X. Xie, H. Wang, J. Zhang, B. Pan and Y. Xie, *J. Am. Chem. Soc.*, 2013, **135**, 18-21.
15. A. P. Côté, A. I. Benin, N. W. Ockwig, M. O'Keeffe, A. J. Matzger and O. M. Yaghi, *Science*, 2005, **310**, 1166-1170.
16. X. Chen, M. Addicoat, E. Jin, L. Zhai, H. Xu, N. Huang, Z. Guo, L. Liu, S. Irle and D. Jiang, *J. Am. Chem. Soc.*, 2015, **137**, 3241-3247.
17. P. Miro, M. Audiffred and T. Heine, *Chem. Soc. Rev.*, 2014, **43**, 6537-6554.
18. N. Huang, L. Zhai, D. E. Coupry, M. A. Addicoat, K. Okushita, K. Nishimura, T. Heine and D. Jiang, *Nat. Commun.*, 2016, **7**, 12325.
19. M. A. Kumar, M. Javeed and B. Jong-Beom, *ChemNanoMat*, 2017, **3**, 373-391.
20. S. Das, P. Heasman, T. Ben and S. Qiu, *Chem. Rev.*, 2017, **117**, 1515-1563.
21. K. Gontarczyk, W. Bury, J. Serwatowski, P. Wieciński, K. Woźniak, K. Durka and S. Luliński, *ACS Appl. Mater. Inter.*, 2017, **9**, 31129-31141.
22. Y. L. Wong, J. M. Tobin, Z. Xu and F. Vilela, *J. Mater. Chem. A*, 2016, **4**, 18677-18686.
23. F. Haase, K. Gottschling, L. Stegbauer, L. S. Germann, R. Gutzler, V. Duppel, V. S. Vyas, K. Kern, R. E. Dinnebier and B. V. Lotsch, *Mater. Chem. Front.*, 2017, **1**, 1354-1361.
24. J.-J. Adjizian, P. Briddon, B. Humbert, J.-L. Duvail, P. Wagner, C. Adda and C. Ewels, *Nat. Commun.*, 2014, **5**, 5842.
25. C.-C. Liu, W. Feng and Y. Yao, *Phys. Rev. Lett.*, 2011, **107**, 076802.
26. A. O'Hare, F. V. Kusmartsev and K. I. Kugel, *Nano Lett.*, 2012, **12**, 1045-1052.
27. J. Zhuang, X. Xu, Y. Du, K. Wu, L. Chen, W. Hao, J. Wang, W. K. Yeoh, X. Wang and S. X. Dou, *Phys. Rev. B*, 2015, **91**, 161409.
28. J. Zhuang, X. Xu, H. Feng, Z. Li, X. Wang and Y. Du, *Science Bulletin*, 2015, **60**, 1551-1562.
29. P. Vogt, P. De Padova, C. Quaresima, J. Avila, E. Frantzeskakis, M. C. Asensio, A. Resta, B. Ealet and G. Le Lay, *Phys. Rev. Lett.*, 2012, **108**, 155501.
30. A. Fleurence, R. Friedlein, T. Ozaki, H. Kawai, Y. Wang and Y. Yamada-Takamura, *Phys. Rev. Lett.*, 2012, **108**, 245501.
31. L. Meng, Y. Wang, L. Zhang, S. Du, R. Wu, L. Li, Y. Zhang, G. Li, H. Zhou, W. A. Hofer and H.-J. Gao, *Nano Lett.*, 2013, **13**, 685-690.
32. H. Nakano, T. Mitsuoka, M. Harada, K. Horibuchi, H. Nozaki, N. Takahashi, T. Nonaka, Y. Seno and H. Nakamura, *Angew. Chem. Int. Ed.*, 2006, **45**, 6303-6306.
33. A. Kara, H. Enriquez, A. P. Seitsonen, L. C. Lew Yan Voon, S. Vizzini, B. Aufray and H. Oughaddou, *Surf. Sci. Rep.*, 2012, **67**, 1-18.
34. J. Zhao, H. Liu, Z. Yu, R. Quhe, S. Zhou, Y. Wang, C. C. Liu, H. Zhong, N. Han, J. Lu, Y. Yao and K. Wu, *Prog. Mater Sci.*, 2016, **83**, 24-151.
35. Q. H. Wang, K. Kalantar-Zadeh, A. Kis, J. N. Coleman and M. S. Strano, *Nat. Nanotechnol.*, 2012, **7**, 699.
36. J. A. Wilson and A. D. Yoffe, *Advances in Physics*, 1969, **18**, 193-335.
37. D. Voiry, J. Yang and M. Chhowalla, *Adv. Mater.*, 2016, **28**, 6197-6206.
38. K. F. Mak, C. Lee, J. Hone, J. Shan and T. F. Heinz, *Phys. Rev. Lett.*, 2010, **105**, 136805.

39. W. Zhao, Z. Ghorannevis, L. Chu, M. Toh, C. Kloc, P.-H. Tan and G. Eda, *ACS Nano*, 2013, **7**, 791-797.
40. X. Huang, Z. Zeng and H. Zhang, *Chem. Soc. Rev.*, 2013, **42**, 1934-1946.
41. D. Xiao, G.-B. Liu, W. Feng, X. Xu and W. Yao, *Phys. Rev. Lett.*, 2012, **108**, 196802.
42. D. Ma, Y. Tang, G. Yang, J. Zeng, C. He and Z. Lu, *Appl. Surf. Sci.*, 2015, **328**, 71-77.
43. S. Liu and S. Huang, *Appl. Surf. Sci.*, 2017, **425**, 478-483.
44. C. Du, H. Lin, B. Lin, Z. Ma, T. Hou, J. Tang and Y. Li, *J. Mater. Chem. A*, 2015, **3**, 23113-23119.
45. M. Naguib, M. Kurtoglu, V. Presser, J. Lu, J. Niu, M. Heon, L. Hultman, Y. Gogotsi and M. W. Barsoum, *Adv. Mater.*, 2011, **23**, 4248-4253.
46. C. Si, J. Zhou and Z. Sun, *ACS Appl. Mater. Inter.*, 2015, **7**, 17510-17515.
47. M. Khazaei, M. Arai, T. Sasaki, C.-Y. Chung, N. S. Venkataramanan, M. Estili, Y. Sakka and Y. Kawazoe, *Adv. Funct. Mater.*, 2013, **23**, 2185-2192.
48. B. Huang, G. Clark, E. Navarro-Moratalla, D. R. Klein, R. Cheng, K. L. Seyler, D. Zhong, E. Schmidgall, M. A. McGuire, D. H. Cobden, W. Yao, D. Xiao, P. Jarillo-Herrero and X. Xu, *Nature*, 2017, **546**, 270.
49. S. Dutta, A. K. Manna and S. K. Pati, *Phys. Rev. Lett.*, 2009, **102**, 096601.
50. C. D. Porter and D. Stroud, *Phys. Rev. B*, 2012, **85**, 235452.
51. Q. Wang and D. O'Hare, *Chem. Rev.*, 2012, **112**, 4124-4155.
52. F. Bergaya and G. Lagaly, in *Developments in Clay Science*, eds. F. Bergaya, B. K. G. Theng and G. Lagaly, Elsevier, 2006, vol. 1, pp. 1-18.
53. G. Mascolo and M. C. Mascolo, *Microporous Mesoporous Mater.*, 2015, **214**, 246-248.
54. M. V. Bukhtiyarova, *J. Solid State Chem.*, 2019, **269**, 494-506.
55. Q. Wang, J. Luo, Z. Zhong and A. Borgna, *Energy & Environmental Science*, 2011, **4**, 42-55.
56. M. Meyn, K. Beneke and G. Lagaly, *Inorg. Chem.*, 1990, **29**, 5201-5207.
57. C. Nyambo, P. Songtipya, E. Manias, M. M. Jimenez-Gasco and C. A. Wilkie, *J. Mater. Chem.*, 2008, **18**, 4827-4838.
58. C. M. Becker, A. D. Gabbardo, F. Wypych and S. C. Amico, *Composites Part A: Applied Science and Manufacturing*, 2011, **42**, 196-202.
59. D. Basu, A. Das, K. W. Stöckelhuber, U. Wagenknecht and G. Heinrich, *Prog. Polym. Sci.*, 2014, **39**, 594-626.
60. S. f. K. Dash, S. Nayak, S. Das and K. Parida, *Current Environmental Engineering*, 2018, **5**, 20-34.
61. A. Malak-Polaczyk, C. Vix-Guterl and E. Frackowiak, *Energy Fuels*, 2010, **24**, 3346-3351.
62. V. Rives, M. del Arco and C. Martín, *Appl. Clay Sci.*, 2014, **88-89**, 239-269.
63. Z. Yang, F. Wang, C. Zhang, G. Zeng, X. Tan, Z. Yu, Y. Zhong, H. Wang and F. Cui, *RSC Advances*, 2016, **6**, 79415-79436.
64. L. Mohapatra and K. Parida, *J. Mater. Chem. A*, 2016, **4**, 10744-10766.
65. X. Long, Z. Wang, S. Xiao, Y. An and S. Yang, *Mater. Today*, 2016, **19**, 213-226.
66. M. Gong and H. Dai, *Nano Research*, 2015, **8**, 23-39.
67. J. M. R. Génin, S. J. Mills, A. G. Christy, O. Guérin, A. J. Herbillon, E. Kuzmann, G. Ona-Nguema, C. Ruby and C. Upadhyay, *Mineral. Mag.*, 2014, **78**, 447-465.
68. Wolfram Koch and M. C. Holthausen, *A Chemist's Guide to Density Functional Theory*, Wiley VCH, 2001.
69. P. Hohenberg and W. Kohn, *Physical Review*, 1964, **136**, B864-B871.
70. R. O. Jones, *Reviews of Modern Physics*, 2015, **87**, 897-923.
71. M. Levy, *Proceedings of the National Academy of Sciences*, 1979, **76**, 6062.
72. W. Kohn and L. J. Sham, *Physical Review*, 1965, **140**, A1133-A1138.
73. U. v. Barth and L. Hedin, *Journal of Physics C: Solid State Physics*, 1972, **5**, 1629-1642.
74. A. K. Rajagopal and J. Callaway, *Phys. Rev. B*, 1973, **7**, 1912-1919.
75. J. P. Perdew, *Phys. Rev. B*, 1986, **33**, 8822-8824.
76. A. D. Becke, *Phys. Rev. A*, 1988, **38**, 3098-3100.
77. C. Lee, W. Yang and R. G. Parr, *Phys. Rev. B*, 1988, **37**, 785-789.
78. J. P. Perdew, K. Burke and M. Ernzerhof, *Phys. Rev. Lett.*, 1996, **77**, 3865-3868.
79. J. P. Perdew, M. Ernzerhof and K. Burke, *J. Chem. Phys.*, 1996, **105**, 9982-9985.
80. J. Heyd, G. E. Scuseria and M. Ernzerhof, *J. Chem. Phys.*, 2003, **118**, 8207-8215.
81. S. Grimme, J. Antony, S. Ehrlich and H. Krieg, *J. Chem. Phys.*, 2010, **132**, 154104.
82. S. Grimme, S. Ehrlich and L. Goerigk, *J. Comput. Chem.*, 2011, **32**, 1456-1465.
83. V. I. Anisimov, F. Aryasetiawan and A. I. Lichtenstein, *J. Phys.: Condens. Matter*, 1997, **9**, 767-808.
84. S. L. Dudarev, G. A. Botton, S. Y. Savrasov, C. J. Humphreys and A. P. Sutton, *Phys. Rev. B*, 1998, **57**, 1505-1509.
85. N. J. Mosey, P. Liao and E. A. Carter, *J. Chem. Phys.*, 2008, **129**, 014103.

86. M. L. M. a. M. Page, eds. K. B. Lipkowitz and D. B. Boyd, VCH, New York, 1993.
87. G. Mills and H. Jónsson, *Phys. Rev. Lett.*, 1994, **72**, 1124-1127.
88. G. Mills, H. Jónsson and G. K. Schenter, *Surf. Sci.*, 1995, **324**, 305-337.
89. G. Henkelman, B. P. Uberuaga and H. Jónsson, *J. Chem. Phys.*, 2000, **113**, 9901-9904.
90. G. Henkelman and H. Jónsson, *J. Chem. Phys.*, 1999, **111**, 7010-7022.
91. R. L. Arevalo, M. C. S. Escaño and H. Kasai, *J. Phys. Chem. C*, 2013, **117**, 3818-3825.
92. S.-M. Xu, H. Yan and M. Wei, *J. Phys. Chem. C*, 2017, **121**, 2683-2695.
93. D. Er, J. Li, M. Naguib, Y. Gogotsi and V. B. Shenoy, *ACS Appl. Mater. Inter.*, 2014, **6**, 11173-11179.
94. Q. Bai, L. Yang, H. Chen and Y. Mo, *Advanced Energy Materials*, 2018, **8**, 1702998.
95. G. Kresse and J. Furthmüller, *Comp. Mater. Sci.*, 1996, **6**, 15-50.
96. P. Steneteg, I. A. Abrikosov, V. Weber and A. M. N. Niklasson, *Phys. Rev. B*, 2010, **82**, 075110.
97. P. Pulay and G. Fogarasi, *Chem. Phys. Lett.*, 2004, **386**, 272-278.
98. N. Metropolis and S. Ulam, *J. Am. Stat. Assoc.*, 1949, **44**, 335-341.
99. W. K. Hastings, *Biometrika*, 1970, **57**, 97-109.
100. P. E. Blöchl, *Phys. Rev. B*, 1994, **50**, 17953-17979.
101. G. Kresse and D. Joubert, *Phys. Rev. B*, 1999, **59**, 1758-1775.
102. F. Tran, R. Laskowski, P. Blaha and K. Schwarz, *Phys. Rev. B*, 2007, **75**, 115131.
103. J. Kästner and P. Sherwood, *J. Chem. Phys.*, 2008, **128**, 014106.
104. G. Henkelman, "Vasp TST tools").
105. M. J. T. Frisch, G. W.; Schlegel, H. B.; Scuseria, G. E.;, M. A. C. Robb, J. R.; Scalmani, G.; Barone, V.; Mennucci, G. A. B.; Petersson and e. al., *Journal*, 2009.
106. A. Schäfer, C. Huber and R. Ahlrichs, *J. Chem. Phys.*, 1994, **100**, 5829-5835.
107. G. Jansen, *Wiley Interdiscip. Rev. Comput. Mol. Sci.*, 2014, **4**, 127-144.
108. A. Heßelmann, G. Jansen and M. Schütz, *J. Chem. Phys.*, 2004, **122**, 014103.
109. H.-J. Werner, P. J. Knowles, M. Schu¨tz, R. Lindh and e. al., *Journal*.
110. J. He, G. Ding, C. Zhong, S. Li, D. Li and G. Zhang, *Nanoscale*, 2019, **11**, 356-364.
111. B. Lukose, A. Kuc, J. Frenzel and T. Heine, *Beilstein. J. Nanotech.*, 2010, **1**, 60-70.
112. T. Hayashi, Y. Hijikata, A. Page, D. Jiang and S. Irle, *Chem. Phys. Lett.*, 2016, **664**, 101-107.
113. E. L. Spitler, B. T. Koo, J. L. Novotney, J. W. Colson, F. J. Uribe-Romo, G. D. Gutierrez, P. Clancy and W. R. Dichtel, *J. Am. Chem. Soc.*, 2011, **133**, 19416-19421.
114. B. T. Koo, W. R. Dichtel and P. Clancy, *J. Mater. Chem.*, 2012, **22**, 17460-17469.
115. O. Bludský, M. Rubeš, P. Soldán and P. Nachtigall, *J. Chem. Phys.*, 2008, **128**, 114102.
116. S. Tsuzuki, K. Honda, T. Uchimaru, M. Mikami and K. Tanabe, *J. Am. Chem. Soc.*, 2002, **124**, 104-112.
117. P. Kuhn, M. Antonietti and A. Thomas, *Angew. Chem. Int. Ed.*, 2008, **47**, 3450-3453.
118. D. Schwarz, Y. Noda, J. Klouda, K. Schwarzová-Pecková, J. Tarábek, J. Rybáček, J. Janoušek, F. Simon, M. V. Opanasenko, J. Čejka, A. Acharjya, J. Schmidt, S. Selve, V. Reiter-Scherer, N. Severin, J. P. Rabe, P. Ecorchard, J. He, M. Polozij, P. Nachtigall and M. J. Bojdys, *Adv. Mater.*, 2017, **29**, 1703399.
119. P. Zhu and V. Meunier, *J. Chem. Phys.*, 2012, **137**, 244703.
120. J. Liu, W. Zan, K. Li, Y. Yang, F. Bu and Y. Xu, *J. Am. Chem. Soc.*, 2017, **139**, 11666-11669.
121. Y. Ding, Y. Wang, J. Ni, L. Shi, S. Shi and W. Tang, *Physica B: Condensed Matter*, 2011, **406**, 2254-2260.
122. Z. Mutlu, D. Wickramaratne, S. Turkyilmaz, H. H. Bay, Z. J. Favors, M. Ozkan, R. K. Lake and C. S. Ozkan, *J. Nanosci. Nanotechnol.*, 2016, **16**, 8419-8423.
123. Y. Gong, Z. Liu, A. R. Lupini, G. Shi, J. Lin, S. Najmaei, Z. Lin, A. L. Elías, A. Berkdemir, G. You, H. Terrones, M. Terrones, R. Vajtai, S. T. Pantelides, S. J. Pennycook, J. Lou, W. Zhou and P. M. Ajayan, *Nano Lett.*, 2014, **14**, 442-449.
124. R. Gutzler, *Phys. Chem. Chem. Phys.*, 2016, **18**, 29092-29100.
125. Note that the following discussion is based on as-calculated band gaps and edge positions without any shift; since the DFT-based band gaps depend up to some extent on the choice of a particular exchange-correlation functional, following discussion should be taken rather qualitatively.
126. D. Malko, C. Neiss, F. Viñes and A. Görling, *Phys. Rev. Lett.*, 2012, **108**, 086804.
127. J. Liu, P. Lyu, Y. Zhang, P. Nachtigall and Y. Xu, *Adv. Mater.*, 2018, **30**, 1705401.
128. H. J. Monkhorst and J. D. Pack, *Phys. Rev. B*, 1976, **13**, 5188-5192.
129. G. A. Tritsaris, E. Kaxiras, S. Meng and E. Wang, *Nano Lett.*, 2013, **13**, 2258-2263.
130. Z. Xing, S. Wang, A. Yu and Z. Chen, *Nano Energy*, 2018, **50**, 229-244.
131. T. Stephenson, Z. Li, B. Olsen and D. Mitlin, *Energy & Environmental Science*, 2014, **7**, 209-231.
132. J. Cabana, L. Monconduit, D. Larcher and M. R. Palacín, *Adv. Mater.*, 2010, **22**, E170-E192.

133. Z. Hu, L. Wang, K. Zhang, J. Wang, F. Cheng, Z. Tao and J. Chen, *Angew. Chem. Int. Ed.*, 2014, **53**, 12794-12798.
134. J. Xie, J. Zhang, S. Li, F. Grote, X. Zhang, H. Zhang, R. Wang, Y. Lei, B. Pan and Y. Xie, *J. Am. Chem. Soc.*, 2013, **135**, 17881-17888.
135. A. Hornés, A. B. Hungría, P. Bera, A. L. Cámara, M. Fernández-García, A. Martínez-Arias, L. Barrio, M. Estrella, G. Zhou, J. J. Fonseca, J. C. Hanson and J. A. Rodriguez, *J. Am. Chem. Soc.*, 2010, **132**, 34-35.
136. S. Royer and D. Duprez, *ChemCatChem*, 2011, **3**, 24-65.
137. B. Qiao, A. Wang, X. Yang, L. F. Allard, Z. Jiang, Y. Cui, J. Liu, J. Li and T. Zhang, *Nature Chem.*, 2011, **3**, 634.
138. Q. Deng, L. Zhao, X. Gao, M. Zhang, Y. Luo and Y. Zhao, *Small*, 2013, **9**, 3506-3513.
139. Y. Tang, Z. Yang and X. Dai, *Phys. Chem. Chem. Phys.*, 2012, **14**, 16566-16572.
140. Y. Li, Z. Zhou, G. Yu, W. Chen and Z. Chen, *J. Phys. Chem. C*, 2010, **114**, 6250-6254.
141. K. H. Warnick, B. Wang, D. E. Cliffel, D. W. Wright, R. F. Haglund and S. T. Pantelides, *Nano Lett.*, 2013, **13**, 798-802.
142. Y.-H. Lu, M. Zhou, C. Zhang and Y.-P. Feng, *J. Phys. Chem. C*, 2009, **113**, 20156-20160.
143. P. Zhao, Y. Su, Y. Zhang, S.-J. Li and G. Chen, *Chem. Phys. Lett.*, 2011, **515**, 159-162.
144. C. Dupont, Y. Jugnet and D. Loffreda, *J. Am. Chem. Soc.*, 2006, **128**, 9129-9136.
145. E. H. Song, Z. Wen and Q. Jiang, *J. Phys. Chem. C*, 2011, **115**, 3678-3683.
146. S. Lin, X. Ye, R. S. Johnson and H. Guo, *J. Phys. Chem. C*, 2013, **117**, 17319-17326.
147. D. G. Costa, A. B. Rocha, W. F. Souza, S. S. X. Chiaro and A. A. Leitão, *J. Phys. Chem. C*, 2012, **116**, 13679-13687.

List of Attached Publications

The thesis is based on following articles:

Attachment No.1:

Reprinted with permission from Jing Jing Liu, **Pengbo Lyu**, Yu Zhang, Petr Nachtigall, Yuxi Xu, *New Layered Triazine Framework/Exfoliated 2D Polymer with Superior Sodium-Storage Properties*. *Adv. Mater.*, **2018**, 30, 1705401. Copyright 2018 Wiley.

To download this article, please use:
https://onlinelibrary.wiley.com/doi/full/10.1002/adma.201705401

Attachment No.2:

Reprinted with permission from Dana Schwarz, Amitava Acharja, Arun Ichangi, **Pengbo Lyu**, Maksym V. Opanasenko, Fabian R. Goßler, Tobias A. F. König, Jiří Čejka, Petr Nachtigall, Arne Thomas, Michael J. Bojdys, *Fluorescent sulphur and nitrogen containing porous polymers with tuneable donor-acceptor domains for light-driven hydrogen evolution*. *Chem. Eur. J.*, **2018**, 24, 11916. Copyright 2018 Wiley.

To download this article, please use:
https://onlinelibrary.wiley.com/doi/full/10.1002/chem.201802902

Attachment No.3:

Reprinted with permission from Dana Schwarz, Amitava Acharjya, Arun Ichangi, Yaroslav S. Kochergin, **Pengbo Lyu**, Maksym V. Opanasenko, Ján Tarábek, Jana Vacek Chocholoušová, Jaroslav Vacek, Johannes Schmidt, Jiří Čejka, Petr Nachtigall, Arne Thomas, Michael J. Bojdys, *Tuning the Porosity and Photocatalytic Performance of Triazine-Based Graphdiyne Polymers through Polymorphism*. *ChemSusChem*, **2019**, 12, 194. Copyright 2019 Wiley.

To download this article, please use:
https://onlinelibrary.wiley.com/doi/full/10.1002/cssc.201802034

Attachment No.4:

Reprinted with permission from Haiyan Duan, **Pengbo Lyu**, Jingjing Liu, Yanli Zhao, and Yuxi Xu, *Semiconducting Crystalline Two-Dimensional Polyimide Nanosheets with Superior Sodium Storage Properties*, *ACS Nano*. **2019**, 13, 2, 2473-2480. Copyright 2019 American Chemical Society.

To download this article, please use:
https://pubs.acs.org/doi/10.1021/acsnano.8b09416

Attachment No.5:

Reprinted with permission from Jingjing Liu, Yang Yang, **Pengbo Lyu**, Petr Nachtigall, Yuxi Xu, *Few-Layer Silicene Nanosheets with Superior Lithium-Storage Properties. Adv. Mater.*, **2018**, 30, 1800838. Copyright 2018 Wiley.

To download this article, please use:
https://onlinelibrary.wiley.com/doi/abs/10.1002/adma.201800838

Attachment No.6:

Reprinted with permission from Shan Gong, Guangyu Zhao, **Pengbo Lyu**, Kening Sun, *A Pseudolayered MoS_2 as Li-Ion Intercalation Host with Enhanced Rate Capability and Durability*. *Small*, **2018**, 14, 1803344. Copyright 2018 Wiley.

To download this article, please use:
https://onlinelibrary.wiley.com/doi/full/10.1002/smll.201803344

Attachment No.7:

Reprinted with permission from Shan Gong, Guangyu Zhao, **Pengbo Lyu**, Kening Sun, *Insights into the intrinsic capacity of interlayer-expanded MoS_2 as a Li-ion intercalation host*. *J. Mater. Chem. A,* **2019**,7, 1187. Copyright 2019 Royal Society of Chemistry.

To download this article, please use:
https://pubs.rsc.org/en/Content/ArticleLanding/2019/TA/C8TA08120D#!divAbstract

Attachment No.8:

Reprinted with permission from **Pengbo Lyu**, Junjie He and Petr Nachtigall, *Theoretical investigation of CO catalytic oxidation by a Fe–PtSe2 monolayer*. *RSC Adv.*, **2017**, 7, 19630. Copyright 2017 Royal Society of Chemistry.

To download this article, please use:
https://pubs.rsc.org/en/content/articlelanding/2017/ra/c6ra27528a#!divAbstract

Attachment No.9:

Reprinted with permission from Junjie He, **Pengbo Lyu**, Lizhong Sun, Angel MoralesGarcia, Petr Nachtigall, *Two-dimensional Janus MXenes: High-temperature Spin-polarized Semiconductor with Zero Magnetization*. *J. Mater. Chem. C*, **2016**, 4, 6500. Copyright 2016 Royal Society of Chemistry.

To download this article, please use:
http://pubs.rsc.org/-/content/articlelanding/2016/tc/c6tc01287f#!divAbstract

Attachment No.10:

Reprinted with permission from Junjie He, **Pengbo Lyu**, Petr Nachtigall, *New TwoDimensional Mn-based MXenes with Room-Temperature Ferromagnetism and Half-Metallicity*. *J. Mater. Chem. C*, **2016**, 4, 11143. Copyright 2016 Royal Society of Chemistry.

To download this article, please use:
http://pubs.rsc.org/-/content/articlelanding/2016/tc/c6tc03917k#!divAbstract

Attachment No.11:

Reprinted with permission from Junjie He, ShuangYing Ma, **Pengbo Lyu**, Petr Nachtigall, *Unusual Dirac Half-Metallicity with Intrinsic Ferromagnetism in Vanadium Trihalides Monolayers*. *J. Mater. Chem. C*, **2016**, 4, 2518. Copyright 2016 Royal Society of Chemistry.

To download this article, please use:
http://pubs.rsc.org/-/content/articlelanding/2016/tc/c6tc00409a#!divAbstract

Attachment No.12:

Reprinted with permission from Junjie He, Xiao Li, **Pengbo Lyu**, Petr Nachtigall, *NearRoom-Temperature Chern Insulator and Dirac Spin-Gapless Semiconductor: Nickle Chloride Monolayer*. *Nanoscale*, **2016**, 4, 2518. Copyright 2017 Royal Society of Chemistry.

To download this article, please use:
http://pubs.rsc.org/-/content/articlelanding/2017/nr/c6nr08522a#!divAbstract

Attached Publications